

UTRECHT UNIVERSITY

TOPOLOGY OF WEYL SEMIMETALS
with non-orientable Brillouin zones

by

Thijs DOUWES

A THESIS

Submitted to the Department of Physics
in partial fulfilment of the requirements
for the degree of

Master of Science

under the joint supervision of

Project supervisor

Prof. Cristiane DE MORAIS SMITH
Department of Physics

Daily supervisor

Dr. Marcus STÅLHAMMAR
Department of Physics

June 2025

Abstract

Contents

1	Introduction	1
1.1	Motivation	1
1.2	State-of-the-art	1
1.3	Main question	1
1.4	Main results	1
1.5	Notational conventions	1
2	Prerequisites	2
2.1	Topological band theory	2
2.2	Homology and cohomology	2
2.2.1	Homology	3
2.2.2	Cohomology	6
3	Topological states of matter & symmetries	10
3.1	Basic definitions	10
3.1.1	Bloch theory	10
3.2	The Su–Schrieffer–Heeger model	11
3.3	Classification of symmetries	16
3.4	Higher-dimensional models	16
3.4.1	The Chern insulator	16
3.4.2	Quantum spin Hall effect	16
3.4.3	3D strong and weak insulators	16
4	Weyl semimetals	17
4.1	Physical aspects	17
4.1.1	Weyl points	18
4.1.2	Global features	19
4.1.3	Semimetals with symmetries	20
4.2	Topological description	23
4.2.1	3D Chern insulators	23
4.2.2	Topology with Weyl points	26
4.2.3	The semimetal Mayer–Vietoris sequence	30
4.2.4	Time-reversal symmetric Weyl semimetals	34

5 Non-orientable systems	38
5.1 Review of recent literature	38
5.1.1 Non-orientable Weyl semimetals	41
5.2 Topological exploration	44
5.2.1 Preliminary clarifications	45
5.2.2 Classification scheme	49
5.2.3 Computation of invariants on $K^2 \times S^1$	53
5.2.4 Classification of K^2 surface states	60
5.3 Other non-orientable Brillouin zones	63
5.4 Inversion symmetry ansatz	66
6 Conclusions and outlook	67
6.1 Summary of main results	67
6.2 Research recommendations	69
APPENDICES	
A Cellular (co)homology	72

Chapter 1

Introduction

1.1 Motivation

1.2 State-of-the-art

1.3 Main question

1.4 Main results

1.5 Notational conventions

- Berry curvature factor 2π

Chapter 2

Prerequisites

2.1 Topological band theory

2.2 Homology and cohomology

The concepts of homology and its dual counterpart cohomology are indispensable tools in the mathematical field of algebraic topology. While seemingly abstract from a physics point of view, many fundamental elements of the physicist’s toolbox—such as Stokes’ theorem—are formulated most naturally in the context of this theory. Additionally, there are deep results relating the cohomology of a space to the classification of different types of vector bundles over this space. Physically, this relates to the classification of topological phases of matter to which this work is dedicated.

Here, we offer a brief introduction to these concepts, aimed at the uninitiated physicist. The goal is not to be completely rigorous, but to give a sufficiently comprehensive understanding that the applications discussed in later chapters may be understood in their proper context. For a more complete picture, the interested reader is referred to standard texts in algebraic topology such as Refs. [1] and [2]. A more geometric treatment relying on differential forms is also found in Ref. [3].

The basic idea underlying homology is that information about the topology of a space M can be gained from studying non-trivial subspaces of M of various dimensions. Perhaps the simplest conceptual realisation of this idea exists in the closely related *homotopy* theory. In this theory, one defines the n th homotopy group $\pi_n(M)$ in terms of maps from the n -dimensional sphere S^n into M . For example, the first homotopy group $\pi_1(M)$ (also known as the *fundamental group*) records the topologically different ways in which loops $\gamma : S^1 \rightarrow M$ can sit inside M . If two such loops cannot be transformed continuously into each other, then they represent different elements of $\pi_1(M)$. This fundamental group forms the conceptual basis behind some topological invariants in physics as well, such as that of the Su–Schrieffer–Heeger model discussed in Section 3.2.

Despite their conceptual simplicity, homotopy groups can be rather unwieldy in practice: they are generally difficult to compute and may have unpredictable structures. For example, even maps from S^n to a lower-dimensional S^m with $m < n$ may be non-trivial, and calculating the associated higher homotopy groups $\pi_n(S^m)$

of the spheres is an important open problem in algebraic topology.

This is where the closely related homology enters the stage. It is conceptually somewhat more involved than homotopy, and strictly speaking it contains less information. However, there is a great payoff: homology groups are generally much easier to compute and structurally simpler than their homotopy counterparts. Moreover, homology can be dualized into cohomology, which is a construction which is both mathematically and physically very natural.

2.2.1 Homology

The basic building blocks of homology theory are oriented subspaces of a space M .¹ Some such subspaces are illustrated for the two-dimensional torus in Figure 2.1. Topological information can be gained from these subspaces by studying their

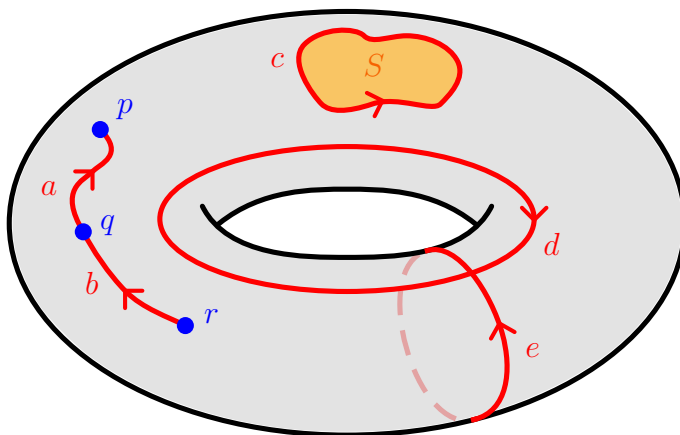


Figure 2.1: The two-torus \mathbb{T}^2 . Some of the oriented subspaces that make up chains in the homology theory are highlighted: components of 0, 1, and 2-chains are coloured blue, red and orange, respectively. The orientation of the 0D and 2D subspaces can be canonically induced from an orientation on the torus in this case.

(oriented) boundaries. The goal of homology is to find subspaces such as d and e in Figure 2.1, which do not have a boundary, but cannot themselves be written as the boundary of another subset either—unlike c , for instance, which is the boundary of S . Spaces like d and e detect topological features of the space, such as the hole in the centre of the torus.

To properly define oriented boundaries, we must work in the context of so-called *n-chains*, which are linear combinations of n -dimensional subspaces of M . For example, $a + b$ is a 1-chain on the torus in Figure 2.1, as is $3a - 2c$. Using n -chains makes boundaries well-behaved under addition. For example, we may define the boundary of a as the 0-chain $\partial a = p - q$, and similarly $\partial b = q - r$; adding these up,

¹There are different ways of formally defining these oriented subspaces, such as mapping simplices (the n -dimensional analogue of triangles) into M or defining a so-called *cell structure* on M . Importantly, these different constructions usually give rise to the same homology groups. Therefore, we will be agnostic to the details and focus on the conceptual basis instead.

we obtain

$$\partial a + \partial b = (p - q) + (q - r) = p - r,$$

which is precisely the boundary of the 1-chain $a + b$.

Formally, an n -chain takes the form

$$\sum_i c_i X_i,$$

where $X_i \subset M$ are oriented n -dimensional subsets of M . The coefficients c_i are usually taken to be integers in \mathbb{Z} , but they may also be e.g. real numbers, rationals or elements of \mathbb{Z}_2 ; to be precise, they must be elements of any fixed Abelian group G , which is called the *coefficient group*. A powerful result called the universal coefficient theorem implies that taking coefficients in the integers $G = \mathbb{Z}$ always results in the richest possible homology theory [1, §3.A]; this is why the coefficients are usually assumed to be elements of \mathbb{Z} unless explicitly stated otherwise.

The n -chains on M naturally form a group under addition in the coefficient group G , which we denote $C_n(M; G)$ —or simply $C_n(M)$ when $G = \mathbb{Z}$. The inverses in this group act to invert the orientation of a chain: for example, the chain $-c$ on the pictured torus looks like c with the arrow pointing in the opposite direction.

The boundary of an n -chain is always an $(n - 1)$ -chain. This is even true for $n = 0$; points have no boundary, so their boundary is the empty “(-1)-chain” in $C_{-1}(M; G) = 0$. This means taking the boundary defines² a map ∂_n from $C_n(M; G)$ to $C_{n-1}(M; G)$ for every integer n . These maps are group homomorphisms—that is, for integer or real coefficients, they are linear: for instance, we have already seen that $\partial(a + b) = \partial a + \partial b$ on the torus.

The boundary maps ∂_n can be used to arrange the chain groups in a so-called *chain complex*:

$$0 \xleftarrow{\partial_0} C_0(M; G) \xleftarrow{\partial_1} C_1(M; G) \xleftarrow{\partial_2} C_2(M; G) \xleftarrow{\partial_3} \dots.$$

These chain complexes are usually finite: for example, the 2-torus in Figure 2.1 has no 3-dimensional subspaces, so its chain complex (with integer coefficients) reads

$$0 \xleftarrow{\partial_0} C_0(\mathbb{T}^2) \xleftarrow{\partial_1} C_1(\mathbb{T}^2) \xleftarrow{\partial_2} C_2(\mathbb{T}^2) \xleftarrow{\partial_3} 0.$$

In practice, the subscript on the maps ∂_n is often dropped when talking about specific subspaces.

A very important property of the chain complex is that composing two boundary maps always yields zero; this is often abbreviated as $\partial^2 = 0$. In other words, boundaries have no boundaries. An example of this can be seen in Figure 2.1: the 1-chain c is the boundary of the 2-chain S , but it does not have a boundary itself. In homology terms, chains like c which have no boundaries are called *cycles*. The set of n -cycles is denoted Z_n and it forms a subgroup of the n -chain group. It is defined in terms of the kernel of ∂_n , i.e. the n -chains that map to the empty chain 0:

$$Z_n(M; G) := \ker(\partial_n) \subset C_n(M; G).$$

²The precise definition of the boundary map depends on the way subspaces are defined, but the properties we discuss here are universal.

The property $\partial^2 = 0$ implies that all boundaries are cycles, but crucially, it does not imply the opposite: there may be cycles which are not boundaries. In Figure 2.1, d and e are such 1-cycles: we cannot find a 2-chain of which d is the boundary, for instance. This implies that the set of n -chains which are boundaries is a subgroup of the group of n -cycles Z_n . The former group is called the group of n -boundaries and denoted B_n . It is defined as the image of ∂_{n+1} :

$$B_n(M; G) := \text{im}(\partial_{n+1}) \subset Z_n(M; G) \subset C_n(M; G).$$

We can now finally define the homology on M . The n th homology group H_n consists of all n -cycles modulo n -boundaries:

$$H_n(M; G) := \frac{Z_n(M; G)}{B_n(M; G)} = \ker(\partial_n)/\text{im}(\partial_{n+1}).$$

Again, the coefficient group G is often dropped from the notation under integer coefficients $G = \mathbb{Z}$. The elements of H_n are called *homology classes*, and they are equivalence classes of n -cycles. Two n -cycles γ_1 and γ_2 are called *homologous* if they differ only by a boundary, i.e. if $\gamma_1 = \gamma_2 + \partial\Gamma$ for some $n+1$ chain Γ . In this case they represent the same homology class, and we write $[\gamma_1] = [\gamma_2] \in H_n(M; G)$. For example, the 1-cycle c in Figure 2.1 is the boundary of the 2-chain S , and so it is homologous to the empty cycle: $c = 0 + \partial S$, meaning $[c] = 0 \in H_1(\mathbb{T}^2)$. Similarly, any n -boundary represents the trivial class in H_n in general. Intuitively, this is because a boundary can always be continuously retracted to a point (for example, c can be retracted by shrinking S), where it vanishes and becomes the empty cycle.

Another important example of homologous cycles is illustrated in Figure 2.2. In

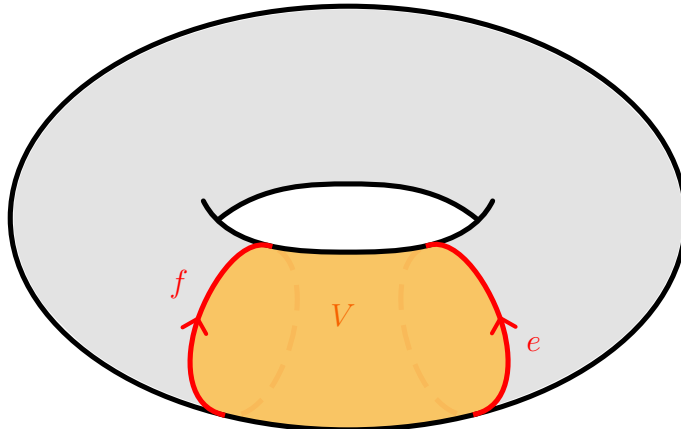


Figure 2.2: The 2-torus \mathbb{T}^2 , featuring the same 1-cycle e as before, and also a 1-cycle f which is obtained by moving e along the torus. The boundary of the 2-chain V indicated in orange is precisely the difference of these cycles: $\partial V = e - f$. Since e and f differ by a boundary, they are homologous, i.e. $[e] = [f] \in H_1(\mathbb{T}^2)$.

this case, we see that non-trivial cycles may also represent the same homology class if they can be deformed into each other continuously.

These examples demonstrate an important general property: the homology group classifies cycles that differ from each other topologically, i.e. cannot be deformed into

one another. As a result, the homology groups H_n have a much simpler structure than the underlying chain groups. For example, the first homology group of the 2-torus $H_1(\mathbb{T}^2)$ consists precisely of elements of the form

$$m_d[d] + m_e[e], \quad m_d, m_e \in G = \mathbb{Z},$$

where d and e are as in Figure 2.1. It follows that this group looks like two copies of \mathbb{Z} :

$$H_1(\mathbb{T}^2) \cong \mathbb{Z}^2.$$

The 0th homology group can be obtained by similar logic: all single points on \mathbb{T}^2 can be continuously moved to a single point p , so that elements of $H_0(\mathbb{T}^2)$ are of the form

$$m_p[p], \quad m_p \in \mathbb{Z},$$

and consequently

$$H_0(\mathbb{T}^2) \cong \mathbb{Z}.$$

For similar reasons, if M consists of k connected components, then $H_0(M) = \mathbb{Z}^k$ in general.

Finally, the only two-dimensional subspace of \mathbb{T}^2 that represents a non-trivial homology class turns out to be the whole torus itself; as a result, H_2 also has a single generator:

$$H_2(\mathbb{T}^2) \cong \mathbb{Z}.$$

These three groups completely classify the homology of the 2-torus, since it only admits n -chains for $0 \leq n \leq 2$. This is a general property of homology: unlike homotopy, where higher homotopy groups may have a highly non-trivial structure, the homology groups H_n of a d -dimensional manifold are always 0 for $n > d$ and $n < 0$.

2.2.2 Cohomology

The chain complex structure underlying homology allows for a natural counterpart called cohomology, which is obtained by *dualising* the chain complex. Dualisation is a concept that shows up all over mathematics; the basic idea is that a mathematical object can be paired with a different object—its *dual*—in order to obtain something like a simple number. A familiar example from physics is that of a covector: in physics notation, any vector V^μ can be paired with any covector ω_μ to obtain a scalar $\omega_\mu V^\mu \in \mathbb{R}$. Formally, a covector is defined as a linear function from the underlying vector space to \mathbb{R} .

A similar construction is used to define *cochains* on a manifold M . An n -cochain is a homomorphism from the n -chain group $C_n(M; G)$ into the coefficient group G ; under the usual integer coefficients, this is a function $C_n(M) \rightarrow \mathbb{Z}$ that assigns an integer to each n -chain linearly. The cochains form a group which has a very similar structure to the chain group itself. We denote the n -cochain group with a raised index:

$$C^n(M; G) := \text{Hom}(C_n(M; G), G).$$

There is an interpretation of cochains with coefficients in \mathbb{R} which is of special relevance to physicists. This comes in the form of integration on differential forms: for example, a 1-form \mathcal{A} can be paired with an oriented 1-dimensional subspace $\ell \subset M$ in a line integral, to obtain a real number $\int_{\ell} \mathcal{A} \in \mathbb{R}$. The definition of integration can be readily generalised from subspaces of M to chains, so that a differential n -form becomes a linear map on the chain group:

$$\omega : C_n(M; \mathbb{R}) \rightarrow \mathbb{R}, \quad c := \sum_i c_i X_i \mapsto \int_c \omega := \sum_i c_i \int_{X_i} \omega,$$

where as before, X_i are oriented n -dimensional subspaces of M and c_i are coefficients in \mathbb{R} . This definition of integration gives rise to a complete cohomology theory in terms of differential forms, called *de Rham cohomology*. This theory is fully equivalent to more abstractly defined cohomology with \mathbb{R} coefficient, and offers a useful link to physical observables: the existence of de Rham cohomology means that many topological invariants can be expressed in terms of integrals over differential forms such as the Berry flux 1-form \mathcal{A} and the Berry curvature 2-form \mathcal{F} .

The main shortcoming of de Rham cohomology lies in its real coefficients. As mentioned before, the universal coefficient theorem implies that \mathbb{Z} coefficients may provide richer homology groups, and the same also holds for cohomology. This is especially true when the homology and cohomology groups contain $\mathbb{Z}_2 := \mathbb{Z}/2\mathbb{Z}$ factors (referred to as *torsion*³), corresponding to \mathbb{Z}_2 physical invariants; these appear especially often on the non-orientable manifolds studied in this work. These factors disappear under \mathbb{R} coefficients, relating to the fact that $\mathbb{R}/2\mathbb{R} = 0$. Still, many of the associated invariants may be expressed using modified integral formulas, and in any case, the de Rham theory offers a physically intuitive perspective on cohomology. For these reasons, we will continue to use it as an analogy for the more abstract concepts of integer-valued cohomology.

Just as in homology, the cochain groups of cohomology are gathered into a *cochain complex*: for example, the cochain complex of the 2-torus is

$$0 \xrightarrow{\delta_{-1}} C_0(\mathbb{T}^2) \xrightarrow{\delta_0} C_1(\mathbb{T}^2) \xrightarrow{\delta_1} C_2(\mathbb{T}^2) \xrightarrow{\delta_2} 0.$$

The maps $\delta_n : C^n \rightarrow C^{n+1}$ are called *coboundary* maps, and they are a natural result of dualising the boundary maps $\partial_{n+1} : C_{n+1} \rightarrow C_n$, meaning they are uniquely defined by the property

$$\delta\omega(c) = \omega(\partial c). \tag{2.1}$$

This duality takes on a familiar form in de Rham cohomology: there, the coboundary map is the exterior derivative d on differential forms, and the duality above becomes

$$\int_c d\omega = \int_{\partial c} \omega,$$

which is precisely Stokes' theorem. For example, suppose a Berry connection 1-form \mathcal{A} is defined on the 2-torus in Figure 2.1. Then the Berry curvature 2-form \mathcal{F} can

³Formally, torsion also includes more general factors \mathbb{Z}_k , but these do not tend to appear in the physics literature as often.

locally be written as $\mathcal{F} = d\mathcal{A}$, and Stokes' theorem tells us that

$$\int_S \mathcal{F} = \int_S d\mathcal{A} = \int_{\partial S} \mathcal{A} = \int_c \mathcal{A}.$$

This dual property of the coboundary maps also ensures that the cochain complex inherits the $\delta^2 = 0$ property of the chain complex: for any n -cochain ω and $n+2$ -chain c , we find

$$\delta^2 \omega(c) = \omega(\delta^2 c) = \omega(0) = 0,$$

so that there is a similar $\delta^2 = 0$ property here.

The construction of the cohomology groups from the cochain complex proceeds completely analogously to that of the homology groups. Just as an n -cycle is an n -chain with no boundary, an n -cocycle is a cochain ω which has no coboundary, i.e. for which $\delta\omega = 0$. In de Rham cohomology, cocycles are called *closed* differential forms (i.e. those with $d\omega = 0$). The n -cocycles form a group which is denoted (again using a raised index) as

$$Z^n(M; G) := \ker(\delta_n).$$

Similarly, an n -coboundary is defined as an n -cochain ω which can be written as $\omega = \delta\eta$ for some $(n-1)$ -cochain η . In the context of de Rham cohomology, the coboundaries are referred to as *exact* differential forms (i.e. forms which can be written as $\omega = d\eta$). Again, the n -coboundaries form a group which is denoted

$$B^n(M; G) := \text{im}(\delta_{n-1}).$$

The $\delta^2 = 0$ property of the cochain complex implies that all coboundaries are cocycles. In de Rham cohomology, this corresponds precisely to the Bianchi identity $d^2 = 0$, which says that all exact forms are closed. As before, this implies that B^n is a subgroup of Z^n , and we can define the n th *cohomology group* as their quotient:

$$H^n(M; G) := \frac{Z^n(M; G)}{B^n(M; G)} = \ker(\delta_n) / \text{im}(\delta_{n-1}).$$

The elements of this group are called *cohomology classes*. In the de Rham picture, non-trivial cohomology classes are represented by forms which are closed, but not exact. For example, this can be the case for the Berry curvature 2-form \mathcal{F} : while it can always be written as $d\mathcal{A}$ *locally*, this depends on a local choice of gauge. Globally, there may be gauge singularities preventing \mathcal{A} from being well defined everywhere. As a result, an expression like $\int_{\mathbb{T}^2} \mathcal{F}$ may have a non-zero value, precisely because \mathbb{T}^2 itself is a 2-cycle with non-trivial global topology. In this case, \mathcal{F} represents a non-zero cohomology class $[\mathcal{F}] \in H^2(\mathbb{T}^2; \mathbb{R})$.

This close link between cohomology classes and non-trivial cycles ensures that the cohomology groups H^n are intimately related to the homology groups H_n in their structure; in fact, in the absence of the aforementioned \mathbb{Z}_2 torsion factors, there is a direct isomorphism $H^n(M) \cong H_n(M)$ for every $n \in \mathbb{Z}$.⁴ This means that for instance, the cohomology groups of the 2-torus are the same as the homology groups:

$$H^0(\mathbb{T}^2) \cong \mathbb{Z}; \quad H^1(\mathbb{T}^2) \cong \mathbb{Z}^2; \quad H^2(\mathbb{T}^2) \cong \mathbb{Z}.$$

⁴To be precise, when there are torsion factors in some homology group H_n , they will appear “one dimension up” in the cohomology group H^{n+1} instead of H^n . Incidentally, since there is no torsion in de Rham cohomology, this means that $H^n(M; \mathbb{R}) \cong H_n(M; \mathbb{R})$ in full generality.

There is a straightforward interpretation of these groups in terms of their homology counterparts: for example, $H^1(\mathbb{T}^2)$ is generated by the cocycles (1-forms) that evaluate to 1 on either of the two non-trivial loops that generate $H_1(\mathbb{T}^2)$, and to 0 on the other.

Finally, we should reiterate what the value in this whole process of dualisation is, given that the cohomology groups are so easily computed from their homology counterparts. The answer is that cohomology, despite being seemingly more involved than homology, is in some ways a more natural theory from both a physical and a mathematical point of view. Physically, the interpretation in terms of differential forms allows topological invariants to be written as integrals of physical quantities. Mathematically, it turns out that there are deep links between cohomology theory and the topological classification of vector bundles; for example, the complex line bundles over a manifold M are always fully classified by $H^2(M)$. This classification of vector bundles is the subject of an advanced area of mathematics known as K-theory, which is really a generalised cohomology theory. K-theory in turn plays an important role in the classification of topological phases of matter [4, 5].

Chapter 3

Topological states of matter & symmetries

Sources: [6, 7, 8, 9]

Topo phases occur in nature: [10]

Finish intro when chapter is more complete

3.1 Basic definitions

- Conducting properties of materials are understood in terms of band structure → Fermi energy. Conductance means Fermi level lies inside one of the bands. [picture]
- N -band system has hilbert space $\mathcal{H} \cong \mathbb{C}^N$, Hamiltonian represented by $N \times N$ matrix. Static system: $H\psi = E\psi$, eigenvalues are energy bands.
- Mostly interested in 2-band systems since only valence/conduction bands are relevant. Then H is a 2×2 Hermitian (for now) matrix. These are given by $H = h_0\mathbb{I} + \mathbf{h} \cdot \boldsymbol{\sigma}$ in general (h_0 changes the energy of all bands but does not affect topology of band crossings) → Bloch Hamiltonian [higher dimensional systems: Clifford algebra]
- For a Bloch Hamiltonian, eigenvalues are $\pm|\mathbf{h}|$, so conductance occurs when $\mathbf{h} = 0$.
- Insulating Hamiltonians are adiabatically connected if they can be continuously deformed into each other without band crossings. Insulators are considered topological if they are not adiabatically connected to a reference trivial phase; then these inhabit different regions of the phase diagram → existence of edge states (not always [8], footnote)

3.1.1 Bloch theory

- We work with crystalline materials which are composed of periodically repeating unit cells.

- In the bulk, we assume the Hamiltonian is periodic in the unit cell. This enables use of Bloch's theorem [11] $\psi(\mathbf{r}) = e^{i\mathbf{k}\cdot\mathbf{r}} u_{\mathbf{k}}(\mathbf{r})$.
- Different values of crystal momentum may yield identical eigenstates, the set of equivalence classes is the Brillouin zone
- Brillouin zone usually has \mathbb{T}^n topology, but internal symmetries etc. may alter this [12] [other sources]
- Discuss dispersion relations

3.2 The Su–Schrieffer–Heeger model

- SSH is usually introduced "physics first", but we would like to work backwards in a sense, to see how bulk topology gives rise to physical properties of a system.

We will take the approach of deriving the Su–Schrieffer–Heeger (SSH) model by beginning with a generic one-dimensional crystal, and introducing two topologically distinct phases in the simplest way possible.

Concretely, consider an infinite one-dimensional chain of unit cells indexed by $n \in \mathbb{Z}$; at this point, we make no assumptions on the internal structure of these unit cells. A boundary will be introduced later, but its relevant properties will turn out to be determined by the crystal's bulk topology. Suppose the real-space Hamiltonian of the system is periodic in the unit cells. By Bloch's theorem, two crystal momenta k and k' are then equivalent if they differ by an integer multiple of 2π . This means that the Brillouin zone B can be taken to be the interval $[-\pi, \pi]$, with the points $-\pi$ and π identified; this space is homeomorphic to the circle S^1 .

We might begin with a simple two-band Bloch Hamiltonian $H(k) = \mathbf{h}(k) \cdot \boldsymbol{\sigma}$, with

$$\mathbf{h} : B \cong S^1 \rightarrow \mathbb{R}^3, \quad k \mapsto \begin{pmatrix} h_x(k) \\ h_y(k) \\ h_z(k) \end{pmatrix}.$$

Such a Hamiltonian describes a gapped phase precisely when the map \mathbf{h} is non-zero everywhere, so that the topological classification of these phases is given by classes of maps from S^1 to \mathbb{R}^3 minus the origin—that is, homotopy classes of loops in $\mathbb{R}^3 \setminus \{0\}$. However, this space has a trivial fundamental group $\pi_1(\mathbb{R}^3 \setminus \{0\}) \cong 0$, meaning that all such loops can be contracted to a point; in other words, all gapped Hamiltonians are adiabatically connected, and there are no topologically interesting phases.

This situation can be remedied by imposing a constraint on the Hamiltonian: we require that $h_z(k) = 0$. Doing this effectively reduces \mathbf{h} to a two-dimensional map:

$$\mathbf{h} : B \cong S^1 \rightarrow \mathbb{R}^3, \quad k \mapsto \begin{pmatrix} h_x(k) \\ h_y(k) \end{pmatrix}.$$

The gapped phases are now classified by the non-trivial fundamental group $\pi_1(\mathbb{R}^2 \setminus \{0\}) \cong \mathbb{Z}$. This group is indexed by winding number: loops that wind around the

origin $a \in \mathbb{Z}$ times cannot be deformed into those with a different winding number $b \neq a$. In particular, loops with a non-zero winding number cannot be contracted to a point, and the associated phases are considered topological. Note that imposing a constraint on the Hamiltonian has made this system rather more interesting from a topological point of view, even though it seems like it has been simplified. Once we move to the physical picture, we will see that this restriction corresponds to imposing a certain symmetry on the system.

Let us now choose a more specific Hamiltonian to arrive at a concrete physical system. We begin with the simplest possible¹ topologically distinct states, one trivial and one topological:

$$\mathbf{h}_{\text{triv}}(k) = \begin{pmatrix} 1 \\ 0 \\ 0 \end{pmatrix}, \quad \mathbf{h}_{\text{top}}(k) = \begin{pmatrix} \cos(k) \\ \sin(k) \\ 0 \end{pmatrix}.$$

To characterise a phase transition between these two states, we consider the linear combination $\mathbf{h}(k) = v\mathbf{h}_{\text{triv}}(k) + w\mathbf{h}_{\text{top}}(k)$, with $v, w \geq 0$. The phase described by the resulting Bloch Hamiltonian is trivial when $v > w$, gapless (i.e. conducting) when $v = w$, and topological when $v < w$; see Figure 3.1.

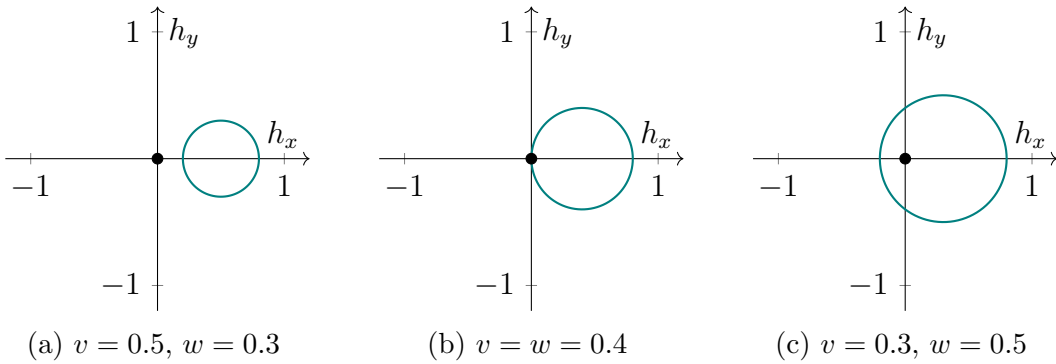


Figure 3.1: Contours in Hamiltonian space for (a) trivial, (b) conducting and (c) topological phases.

We are now in a position to start analysing the physics of the system. Concretely, the momentum space Hamiltonian is given by

$$H(k) = \mathbf{h}(k) \cdot \boldsymbol{\sigma} = (v + w \cos(k))\sigma_x + w \sin(k)\sigma_y = \begin{pmatrix} 0 & v + w e^{-ik} \\ v + w e^{ik} & 0 \end{pmatrix}.$$

We can set up a Fourier transform to real space by rewriting this suggestively in terms of the unit cell index n :

$$H(k) = e^{-ik(n-n)} \begin{pmatrix} 0 & v \\ v & 0 \end{pmatrix} + e^{-ik((n+1)-n)} \begin{pmatrix} 0 & w \\ 0 & 0 \end{pmatrix} + e^{-ik(n-(n+1))} \begin{pmatrix} 0 & 0 \\ w & 0 \end{pmatrix}$$

I need to work out the details of this Fourier transform later, my calculations aren't working out. Transforming from a periodic Brillouin zone to (discrete or infinite)

¹Our particular choice of x , y , and z coordinates very conveniently leads to the SSH model. However, mathematically speaking, all similar models are related by a simple change of basis.

real space is breaking my brain. I imagine it needs to look something like this (where $M_{0/\pm 1}$ are the three matrices above):

$$\begin{aligned}
 \hat{H} &= \int_B H(k) |k\rangle \langle k| \\
 &= \int_{-\pi}^{\pi} \frac{dk}{2\pi} \left(\sum_{a \in \{0, \pm 1\}} e^{-ika} M_a \right) \left(\sum_n e^{-ikn} |n\rangle \right) \left(\sum_{n'} \langle n'| e^{ikn'} \right) \\
 &= \sum_{a,n,n'} \left(\int_{-\pi}^{\pi} \frac{dk}{2\pi} e^{-ik(a+n-n')} \right) M_a |n\rangle \langle n'| \\
 &= \sum_{a,n,n'} \delta_{n+a,n'} M_a |n\rangle \langle n'| \\
 &= \sum_{a,n} M_a |n\rangle \langle n+a|
 \end{aligned}$$

But I don't fully understand the first step, the sign of a is wrong and normalization is broken. Maybe it's easier to discretize first and do a DFT?

- It follows [how exactly?] that we can write the Hamiltonian in a unit cell basis as

$$\hat{H} = \sum_{n=-\infty}^{\infty} \left[|n\rangle \langle n| \otimes \begin{pmatrix} 0 & v \\ v & 0 \end{pmatrix} + (|n+1\rangle \langle n| \otimes \begin{pmatrix} 0 & w \\ 0 & 0 \end{pmatrix} + \text{h.c.}) \right]$$

- Mention tight binding somewhere around this point

This Hamiltonian contains a term which acts within the unit cells, and terms which act between neighbouring unit cells, parametrized by v and w respectively. The structure of these interactions can be made somewhat more transparent by going to a finite chain of length N . The Hamiltonian then becomes

$$\hat{H} = \sum_{n=0}^N |n\rangle \langle n| \otimes \begin{pmatrix} 0 & v \\ v & 0 \end{pmatrix} + \sum_{n=0}^{N-1} \left(|n+1\rangle \langle n| \otimes \begin{pmatrix} 0 & w \\ 0 & 0 \end{pmatrix} + \text{h.c.} \right),$$

where open boundary conditions have been introduced on the ends of the chain to allow the boundary behaviour to be studied. The tensor products can be expanded in order to cast the Hamiltonian into a full $2N \times 2N$ matrix:

$$\hat{H} = \begin{pmatrix} 0 & v & 0 & 0 & & & & & \\ v & 0 & w & 0 & & & & & \\ 0 & w & 0 & v & & & & & \\ 0 & 0 & v & 0 & & & & & \\ & & & & \ddots & & & & \\ & & & & & 0 & & & \\ & & & & & & \ddots & & \\ & & & & & & & 0 & 0 \\ 0 & & & & & & & w & 0 \\ & & & & & & & 0 & w & 0 \\ & & & & & & & 0 & 0 & v \\ 0 & 0 & v & 0 & & & & 0 & 0 & 0 \end{pmatrix}.$$

A physical interpretation of this system presents itself in the form of this matrix: it describes a chain of $2N$ sites, with alternating hopping amplitudes v and w between neighbouring sites. The unit cells now consist of two of these sites, and v and w are referred to as the *intra-cell* and *inter-cell* hoppings, respectively. When these two hoppings are equal, the system is in the gapless phase $v = w$, corresponding to a chain where all bonds are equally strong. Intuitively, this homogeneity allows electrons to propagate freely along the chain. On the other hand, in the insulating cases $v \neq w$, one of the two hoppings is stronger than the other, and the electrons tend to be confined around these stronger bonds.

Dividing the unit cells into two individual sites in this way allows us to distinguish two so-called *sublattices* of the crystal, which we label A and B . The notation can then be simplified by labelling quantum states according to the sublattice on which they are localized:

$$|n, A\rangle \equiv |n\rangle \otimes \begin{pmatrix} 1 \\ 0 \end{pmatrix}, \quad |n, B\rangle \equiv |n\rangle \otimes \begin{pmatrix} 0 \\ 1 \end{pmatrix}.$$

In this notation, the Hamiltonian becomes

$$\hat{H} = \left(\sum_{n=0}^N v |n, B\rangle \langle n, A| + \sum_{n=0}^{N-1} w |n+1, A\rangle \langle n, B| \right) + \text{h.c.} \quad (3.1)$$

The tight-binding model of alternating hoppings is precisely the SSH model: it was introduced in 1979 by Wu-Pei Su, John Robert Schrieffer, and Alan J. Heeger to describe polyacetylene (Figure 3.2), a polymer chain which features alternating single and double covalent bonds [13, 14]. This material displays unexpectedly high

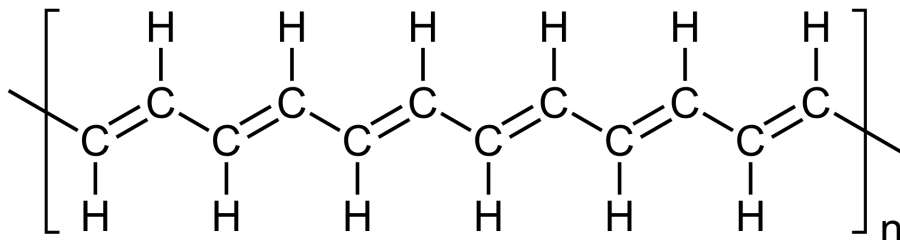


Figure 3.2: Structural diagram of polyacetylene. Electrons are transported more readily along the double bonds, which is modelled using a larger hopping parameter.

conductivity when doped with halogen impurities, and the SSH model affords an explanation for this.

To understand how this metallic behaviour comes about, the differences between the trivial and the topological phase must be examined more closely. The two phases appear to be identical at a first glance: if the unit cell in polyacetylene is chosen in such a way that the stronger double bond represents the intra-cell hopping v , then the system is in the trivial phase $v > w$, and if instead the unit cell is centred around a single bond, $v < w$ and the phase is topological. In either case, valence

electrons are expected to remain localized around the double bonds, leading to the same insulating bulk behaviour.²

The difference between the two phases only becomes apparent when the endpoints of the chain are studied. [introduce a figure here] For example, the leftmost atom is not subject to any inter-cell hopping, and it is only connected to the other atom in its unit cell. In the trivial case, this connection is strong and the two atoms share their valence electrons. In the topological phase, on the other hand, the second atom from the left prefers to share electrons with its right-hand neighbour, and the leftmost atom becomes isolated. In the limit where v goes to zero, this isolation becomes complete and the edge sites carry zero-energy eigenstates. In this case, only the second term in the Hamiltonian (3.1) survives, and the edges obey the eigenvalue equations

$$\hat{H} |1, A\rangle = \hat{H} |N, B\rangle = 0.$$

These edge modes can be shown to persist for non-zero $v < w$, in which case they become highly localized and approach zero energy in the $N \rightarrow \infty$ limit.³ The salient point is that the boundary modes of the topological phase exist inside the energy gap: their energy eigenvalues have a degeneracy at the Fermi level $\varepsilon_F = 0$. [Perhaps include dispersion figure]

Something remarkable has happened: we have started from a topological description of a gapped bulk phase, and the resulting physical effects appear as in-gap zero energy modes on the boundary of the material. As will become apparent looking at other examples, the existence of edge modes at the Fermi level is a fairly⁴ general feature of topological phases of matter, captured in the so-called *bulk-boundary correspondence*. It can be thought of as being a result of the inability to go continuously from a topological gapped phase to a trivial one in real space; in particular, the outside boundary of an idealised material connects to the vacuum, which is also considered a trivial gapped phase.

- Discuss physics of polyacetylene (solitons on trivial/topological interface) and experimental observations of solitons + berry phase [16, 17]
- We can now physically interpret the meaning of setting $h_z = 0$: it ensures that hopping only occurs between the two sublattices A and B , and not within them (i.e. there are only off-diagonal elements in the internal degrees of freedom). If we define the sublattice projection operators

$$\hat{P}_A = \mathbb{I} \otimes \begin{pmatrix} 1 & 0 \\ 0 & 0 \end{pmatrix}, \quad \hat{P}_B = \mathbb{I} \otimes \begin{pmatrix} 0 & 0 \\ 0 & 1 \end{pmatrix}$$

²The attentive reader might wonder why the conducting $v = w$ phase does not occur naturally in this system. This is a result of the so-called Peierls transition: in a nutshell, introducing a band gap locally lowers the energy of the (filled) valence band and raises that of the (empty) conduction band. This makes it energetically favourable for atoms in the chain to pair up, in a process referred to as dimerisation.

³A precise understanding of this is beyond the scope of this review; the interested reader is referred to e.g. [7].

⁴This is not a completely general statement: topological phases with edge modes at energies other than ε_F have been shown to be theoretically feasible [15]. For our purposes, it will be sufficient to restrict our attention to edge modes at the Fermi level.

then the Hamiltonian obeys

$$\hat{P}_A \hat{H} \hat{P}_A = \hat{P}_B \hat{H} \hat{P}_B = 0$$

and so since $\hat{P}_A + \hat{P}_B$ is the identity we have

$$\begin{aligned}\hat{H} &= (\hat{P}_A + \hat{P}_B) \hat{H} (\hat{P}_A + \hat{P}_B) \\ &= \hat{P}_A \hat{H} \hat{P}_B + \hat{P}_B \hat{H} \hat{P}_A \\ &= (\hat{P}_A - \hat{P}_B) \hat{H} (\hat{P}_B - \hat{P}_A) \\ &\equiv -\hat{\Gamma} \hat{H} \hat{\Gamma}\end{aligned}$$

with $\hat{\Gamma} \equiv \hat{P}_A - \hat{P}_B$ having the property that $\hat{\Gamma} = \hat{\Gamma}^{-1} = \hat{\Gamma}^\dagger$; this is called sublattice symmetry and it also applies to the momentum space Hamiltonian $H(k)$.

- An immediate consequence of our setup is that the trivial and topological phase become adiabatically connected if we allow for sublattice symmetry breaking ($h_z \neq 0$).
- Talk more about \mathbb{Z} invariant (next-nearest-neighbour hopping etc.)

3.3 Classification of symmetries

3.4 Higher-dimensional models

3.4.1 The Chern insulator

- The 2nd cohomology group introduced here classifies complex vector bundles over the Brillouin zone. The vector bundle classification point of view is not one we will pursue in detail in this work, but it is in some ways more fundamental than the description in terms of Berry curvature, especially for systems with additional symmetries. This makes it the preferred point of view for precise mathematical classification schemes.

3.4.2 Quantum spin Hall effect

- Introduce the \mathbb{Z}_2 FKMI invariant in 2D, both in terms of product-of-signs and EBZ integral. (Perhaps mention twisted equivariant cohomology? Not the classical treatment and may not be necessary at this point)

3.4.3 3D strong and weak insulators

- Refer to tenfold way, weak \mathbb{Z}_2 topology on T-invariant 2D subsystems and strong 3D \mathbb{Z}_2 invariant based both on POS and difference of weak invariants.

Chapter 4

Weyl semimetals

In recent years, interest in topological materials has expanded beyond the purely gapped phases in insulators and superconductors, into the realm of metals and other related gapless phases. Some of the topological conductors that are of the greatest interest are called Weyl semimetals, which form the focus of the remainder of the present work.

Weyl semimetals are materials that host gapless modes only at very specific momenta in the Brillouin zone. They have a myriad of properties that make them worthy subjects of study, not only from a theoretical perspective but also in potential experimental and engineering applications. Practically, Weyl semimetals have exotic transport properties such as a resistance which is highly sensitive to the application of a magnetic field, opening up countless possibilities for electronic applications.

Experimentally, Weyl semimetals may comprise the first platform in which the chiral fermions described by Hermann Weyl in 1929 (Ref. [18]) can be studied in the wild, in the form of bulk quasiparticle excitations. Despite their mathematical simplicity, such Weyl fermions do not appear to exist as fundamental particles in nature.

This aspect of Weyl semimetals is also of theoretical interest, since their fermionic modes may be altered in different ways beyond the simple description originally given by Weyl. Additionally, the topology of Weyl semimetals is intrinsically rich and generalises many aspects of insulator topology. It is this latter topological point of view which is the main focus of this chapter; the interested reader is referred to Refs. [19] and [20] for more complete physically-minded overviews.

This chapter does not contain any new results; instead, its purpose is to provide the necessary context for the results presented in Chapter 5. We begin by introducing the most important physical aspects of Weyl semimetals in Section 4.1, with a focus on the features that are of topological relevance. Section 4.2 then dives deeper into the underlying topology, introducing many of the relevant mathematical concepts at a fairly elementary level.

4.1 Physical aspects

The concept of Weyl semimetals arises naturally when studying how different energy bands relate to each other in three-dimensional solids. Whereas one and two-

dimensional materials are generally gapped unless additional symmetries force the bands to touch, the situation is different in three dimensions. In this context, so-called *accidental band crossings* are expected based on geometric arguments [21].

Accidental crossings can be understood by studying the interplay between any two of the energy bands. In most physically relevant scenarios these will be the valence and conduction band, since these determine the transport properties of a material. Recall that the generic Hermitian two-band Hamiltonian can be written as

$$\mathcal{H}(\mathbf{k}) = h_0(\mathbf{k})\mathbb{I} + \mathbf{h}(\mathbf{k}) \cdot \boldsymbol{\sigma},$$

where \mathbf{k} lives in the three-dimensional Brillouin torus \mathbb{T}^3 . The eigenvalues of this Hamiltonian are

$$E(\mathbf{k}) = h_0(\mathbf{k}) \pm |\mathbf{h}(\mathbf{k})| = h_0(\mathbf{k}) \pm \sqrt{h_1^2(\mathbf{k}) + h_2^2(\mathbf{k}) + h_3^2(\mathbf{k})},$$

so that the gap between the two bands closes exactly when $\mathbf{h}(\mathbf{k}) = 0$. That is, band crossings occur at the simultaneous zeroes of three functions h_i for $i \in \{1, 2, 3\}$, all depending on three momentum degrees of freedom. Such a system of three equations with three parameters generically has point-like solutions: the zeroes of each individual h_i normally form a surface in \mathbb{T}^3 , two such surfaces intersect in a set of curves, and the third surface intersects these curves in a set of points. This means that two bands in a three-dimensional system generically have point-like intersections where the gap closes, given that the bands are close enough together (i.e. the functions h_i each have zeroes to begin with). These band crossings are called accidental because they are not enforced by any symmetry of the system, but as we will review shortly, they are actually topologically robust and cannot be gapped out by small perturbations.

4.1.1 Weyl points

Near a band intersection at $\mathbf{k} = \mathbf{k}_w$, the Hamiltonian can be linearized: writing $\delta\mathbf{k} := \mathbf{k} - \mathbf{k}_w$, it can be expanded as

$$\mathcal{H}(\delta\mathbf{k}) = h_0(\mathbf{k}_w)\mathbb{I} + \mathbf{v}_0 \cdot \delta\mathbf{k}\mathbb{I} + \sum_{i=1}^3 \mathbf{v}_i \cdot \delta\mathbf{k} \sigma^i + \mathcal{O}(\delta\mathbf{k}^2), \quad (4.1)$$

where $(\mathbf{v}_\mu)_i := \partial_{k^i} h_\mu|_{\mathbf{k}=\mathbf{k}_w}$ records the rate of change of the different components of the Hamiltonian. The spectrum associated with this linear equation looks like two cones which touch at $\mathbf{k} = \mathbf{k}_w$, often collectively called the *Weyl cone*; see Figure [need to add a figure here still]. The different components of Equation (4.1) can all be given an interpretation in terms of this Weyl cone: for example, $h_0(\mathbf{k}_w)$ is the energy at which the bands touch, and it determines how far this crossing is from the Fermi energy $\varepsilon_F = 0$. If h_0 is sufficiently far from the Fermi level, the Fermi surface expands to connect with those around other band crossings and gains an extensive two-dimensional structure. Normal metallic dispersive behaviour dominates in this case. However, if h_0 is close enough to zero, then the Fermi surface around \mathbf{k}_w becomes approximately point-like, and there is a low-energy bulk conducting mode

at \mathbf{k}_w . In this case, the point \mathbf{k}_w is called a *Weyl point* or *Weyl node*. When all of the crossings between the valence and conduction band have this property, the material is referred to as a *Weyl semimetal*.¹

This nomenclature is derived from the traceless \mathbf{v}_i term in Equation (4.1): it bears resemblance to the simple chiral fermions described by Herman Weyl in 1929 [18],

$$H_{\pm} = \mp c \mathbf{p} \cdot \boldsymbol{\sigma},$$

where the speed of light c is replaced by the smaller effective velocities \mathbf{v}_i in different directions. In a Weyl semimetal, the aforementioned low-energy modes have similar dispersive properties to Weyl fermions. This is one of the reasons Weyl semimetals are a compelling object of study.

One particularly interesting feature of Weyl fermions is that they have a non-zero chirality associated with them, which leads to certain non-conserved charges upon quantisation—this is known as the chiral anomaly. It turns out that a similar truth holds for the band crossings described by Equation (4.1). They feature an intrinsic chirality χ , which can be calculated in generic cases by collecting the velocities \mathbf{v}_i into a 3×3 matrix $V_i^j := (\mathbf{v}_i)_j$ and computing the sign of its determinant:

$$\chi = \text{sign } |V_i^j|, \quad (4.2)$$

which yields a chirality of $\chi = \pm 1$. In special cases where the band crossing is non-linear, the chirality may take on other integer values; this is captured more generally using a Berry curvature integral on a two-dimensional sphere surrounding the Weyl point. In this light, Weyl points can be viewed as sources or sinks of the Berry field, with a quantized integer charge. This charge is topological in nature, which is exactly why Weyl points are robust to perturbations. The implications of this topological perspective will be explored in greater detail in Section 4.2.

A final feature of Equation (4.1) that bears mentioning is the inclusion of the \mathbf{v}_0 term. This term can be interpreted in terms of a tilting of the associated Weyl cone. For small \mathbf{v}_0 , the Fermi surface of a Weyl point remains point-like, and the dispersive properties of the virtual Weyl fermion are not greatly affected. However, for large enough \mathbf{v}_0 , the Weyl cone may begin to intersect the Fermi level, causing electron and hole pockets to form on either side of the Weyl point; see Figure 4.1. This tipping of the Weyl cone induces significantly altered dispersion, leading to different electronic properties. Such materials are categorised separately as so-called *type II* Weyl semimetals. This distinction is purely physical, however; the different types of Weyl semimetals cannot be distinguished topologically.

4.1.2 Global features

One important restriction on Weyl semimetals is that the total chirality of all Weyl points in the Brillouin zone must sum to zero—that is, for every source of the Berry field (Weyl point with $\chi > 0$) there must also be a sink ($\chi < 0$), and vice versa.

¹The term *Weyl metal* is also sometimes used for materials in which the Fermi surface is not point-like due to large h_0 , but still confined to closed surfaces around the band crossings [22]. The topology of such Weyl metals is equivalent to that of their semimetal counterparts, and we will pay them no further mind.

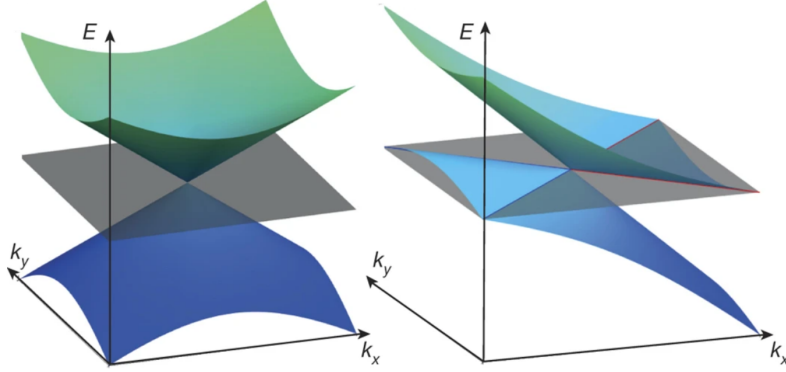


Figure 4.1: Figure from Ref. [23]. Left: Weyl cone in a normal (type I) Weyl semimetal. Right: “Overtilted” Weyl cone in a type II Weyl semimetal. Electron and hole pockets are outlined in red and blue, respectively.

This result is known as the Nielsen–Ninomiya theorem, after Holger Bech Nielsen and Masao Ninomiya who proved it in a more general context in 1981 [24, 25]. We will explore the topological nature of this theorem in more detail in Section 4.2. Physically, this charge cancellation is related to the aforementioned chiral anomaly: electric charge is locally non-conserved near a Weyl point under the application of electric and magnetic fields, and this effect must be cancelled by a Weyl point of the opposite chirality. More details on the chiral anomaly in Weyl semimetals are reviewed in Ref. [20].

The Nielsen–Ninomiya theorem is an indication that Weyl points must communicate with their opposite-chirality counterparts in some way to allow transport of charge. This connection manifests itself on the surface of a Weyl semimetal: there, gapless states called *Fermi arcs* appear in the form of curves connecting the projections of oppositely-charged Weyl points; see Figure 4.2. Fermi arcs serve as important experimental signatures of Weyl semimetals, and they have been observed in both electronic and artificial crystals since 2015 [26–31]; see Figure 4.3.

4.1.3 Semimetals with symmetries

Thus far, we have discussed Weyl semimetals without assuming any additional symmetry constraints. However, real crystalline solids often naturally possess symmetries beyond simple translational symmetry. Two such symmetries which are especially relevant to the discussion of Weyl semimetals are time-reversal symmetry and inversion symmetry.

Inversion symmetry is a natural property of many real-space lattices: it implies that there is an inversion centre \mathbf{x}_0 in the unit cell around which the lattice is symmetric as $\mathbf{x} \leftrightarrow \mathbf{x}_0 - \mathbf{x}$. In momentum space, this symmetry acts on the Hamiltonian as

$$\mathcal{H}(\mathbf{k}) = U\mathcal{H}(-\mathbf{k})U^\dagger, \quad (4.3)$$

where U is some unitary transformation. In particular, this implies that a Weyl point at $\mathbf{k} = \mathbf{k}_w$ has a partner at $\mathbf{k} = -\mathbf{k}_w$ with the opposite chirality. Take, for

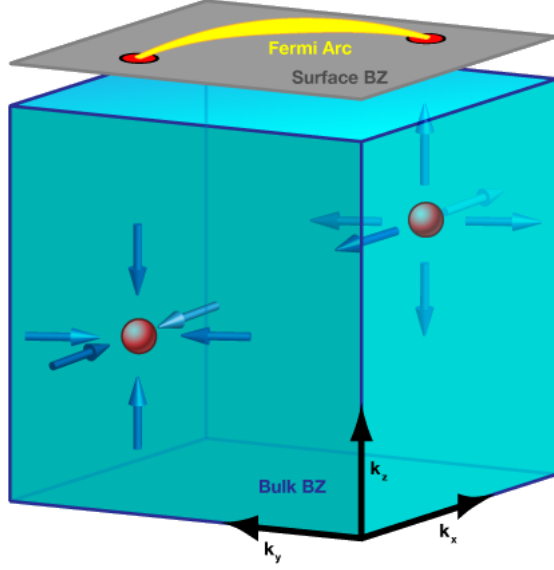


Figure 4.2: Figure by Alan Stonebraker. The 3D bulk Brillouin zone of a Weyl semimetal with two Weyl points of negative and positive chirality, depicted as a sink and a source of the Berry field respectively. A 2D surface Brillouin zone is depicted in grey at the top, featuring the projection of the two Weyl nodes connected by a Fermi arc of gapless states.

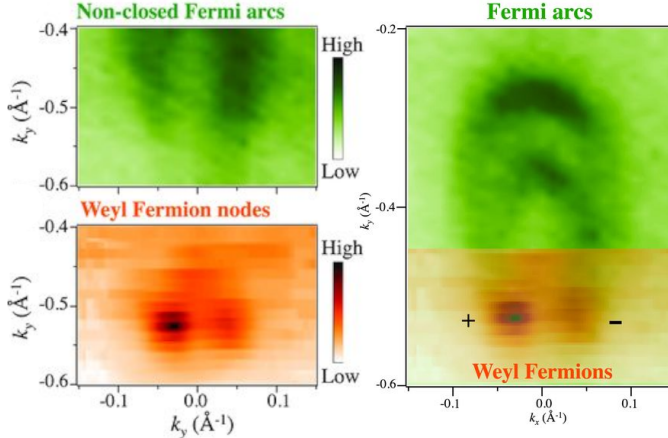


Figure 4.3: Figures from Ref. [29]. Experimental bulk (orange) and surface (green) Fermi surfaces, obtained through angle-resolved photoemission spectroscopy (ARPES). Bottom left: Two Weyl points appearing close together in the bulk. Top left: Fermi arcs are shown to terminate on the surface Brillouin zone above these Weyl points. Right: Bulk measurements are overlaid on the surface measurements at matching k_x and k_y values, showing good agreement between the position of the Weyl nodes and the tail ends of the Fermi arcs. In this case, the two distinct Fermi arcs appear because there are two separate sets of Weyl nodes with the same k_x and k_y coordinates.

example, the case of $U = \mathbb{I}$ and a Weyl point with the simple linearized Hamiltonian

$$\mathcal{H}(\delta\mathbf{k}) = \sum_{i,j} V_i^j \delta k_j \sigma^i.$$

This point has chirality $\chi = \text{sign} |V_i^j|$, and Equation (4.3) implies that

$$\mathcal{H}(-\delta\mathbf{k}) = \sum_{i,j} (V')_i^j (-\delta k_j) \sigma^i = \mathcal{H}(\delta\mathbf{k}),$$

meaning that there is a Weyl point at $\mathbf{k} = -\mathbf{k}_w$ with chirality $\chi' = \text{sign} |(V')_i^j| = \text{sign} |-V_i^j| = -\chi$. This reversal of chirality means Nielsen–Ninomiya is automatically satisfied under inversion symmetry. As a result, the minimum number of Weyl points in such a system is two; a Weyl point may be connected to its own symmetric partner via surface Fermi arcs.

Time-reversal symmetry has a similar action in momentum space, since momentum has a time component. It differs in the sense that time-reversal is an anti-unitary symmetry, meaning it also induces complex conjugation on the Hamiltonian:

$$\mathcal{H}(\mathbf{k}) = U \mathcal{H}^*(-\mathbf{k}) U^\dagger.$$

This complex conjugation changes the sign of the $\sigma^{(2)}$ term in the Hamiltonian; for Weyl points, this changes the sign of \mathbf{v}_2 , inducing a sign change in the determinant of V_i^j . This cancels the sign change discussed above, meaning a Weyl point at $\mathbf{k} = \mathbf{k}_w$ always comes with a symmetric partner of *equal* chirality at $\mathbf{k} = -\mathbf{k}_w$. Such a pair of equal-chirality points is sometimes referred to as a *Kramers pair*. The presence of Kramers pairs means that the minimum number of Weyl points in a time-reversal invariant Weyl semimetal is four: following Nielsen–Ninomiya, a pair of $\chi = +1$ points must always be accompanied by a pair of $\chi = -1$ points and vice versa.

The fact that the chirality of Weyl points is reflected in different ways under inversion and time-reversal symmetry immediately implies that a Weyl semimetal cannot satisfy both symmetries at once: if a Weyl point has a non-zero chirality χ , then inversion implies its partner has chirality $-\chi$, while time-reversal implies it should have chirality χ . Physically, this is because the combination of inversion and time-reversal induces a spin degeneracy in the band structure, making modes of opposite chiralities coincide. This is in close analogy to the way in which a Dirac fermion combines two Weyl fermions of opposite chirality into a single description; this is precisely why band touching points of this nature are called *Dirac cones*, and systems featuring them are referred to as *Dirac semimetals*. Because of the lack of non-zero chiralities, such materials are topologically less rich than their Weyl counterparts, and we will not expand on them further.

All in all, a candidate Weyl semimetallic material must break either inversion or time-reversal symmetry. Of the two, breaking time-reversal symmetry is conceptually simpler in theory: the minimum amount of Weyl points is lower, and the symmetry is straightforwardly broken in the presence of a magnetic field. However, in practice the experimental detection of Fermi arcs and other spectral features relies on angle-resolved photoemission spectroscopy (ARPES), which is sensitive to magnetic fields. This is why to date, all experimentally confirmed electronic Weyl semimetals have preserved time-reversal symmetry and broken inversion symmetry instead [26–30].

4.2 Topological description

In all the systems studied in Chapter 3, the underlying approach to topological classification has been to study which band structures cannot be deformed into each other without closing the band gap anywhere in the Brillouin zone. Weyl semimetals already feature band crossings in the bulk to begin with, meaning that this approach needs to be modified. The basic idea involves first fixing a number of gapless points in place, and then studying what gapped topologies are admitted on the rest of the Brillouin zone outside of these points. There are many intricacies to this idea, some of which we attempt to review pedagogically in this section.

Though most of the experimental candidates for Weyl semimetals feature either inversion or time-reversal symmetry, the conceptual topology framework is simplest in the absence of any symmetries beyond lattice translation. The majority of this section is written with this context in mind. Most of the concepts here are borrowed from two (fairly technical) works by Vargese Mathai and Guo Chuan Thiang [32, 33].

Only in the final part of this section will we return to time reversal symmetric systems, and review how the inclusion of this symmetry alters the topological description. This provides important context to our treatment of other symmetries in Chapter 5.

4.2.1 3D Chern insulators

To get a good intuition for the topological description of Weyl semimetals, it is useful to first consider a fully insulating material with similar properties. Suppose we have a three-dimensional material that is not subject to any additional symmetries. Such a material is called a 3D Chern insulator [31, 34, 35], in analogy to the 2D Chern insulator studied in Section 3.4.1. This system is not a semimetal, but it provides the relevant topological backdrop: Weyl semimetals can be obtained by letting the bands touch in a 3D Chern insulator. As we will discuss shortly, this allows them to act as transitional phases between different insulating topological states.

From the Atland–Zirnbauer classification in Table [reference], one might expect such a 3D type A system to be topologically trivial. However, as seen before in Equation [reference] (and perhaps also in 3D BHZ/Kane–Mele if I discuss this in ch. 2), the full topological classification of materials depends not only on the top-dimensional topology, but also on that borrowed from lower-dimensional subspaces. In the case of a 3D Chern insulator, this topology arises on two-dimensional slices of the Brillouin zone; an example of such a slice is highlighted in Figure 4.4.

There are three topologically distinct ways to slice up the three-torus, all perpendicular to one of the three coordinate directions.² These slices have the topology of a two-torus T^2 , and a Chern number can be obtained by integrating the Berry curvature \mathcal{F} of the system over them: for example, perpendicular to the x direction

²Other 2D slices exist, such as those going diagonally across, but these can all be considered linear combinations of the three “orthogonal” slices. To be precise, the different classes of 2D subspaces of T^3 form the second homology group $H_2(T^3) \cong \mathbb{Z}^3$, and this group is *generated* by the orthogonal slices.

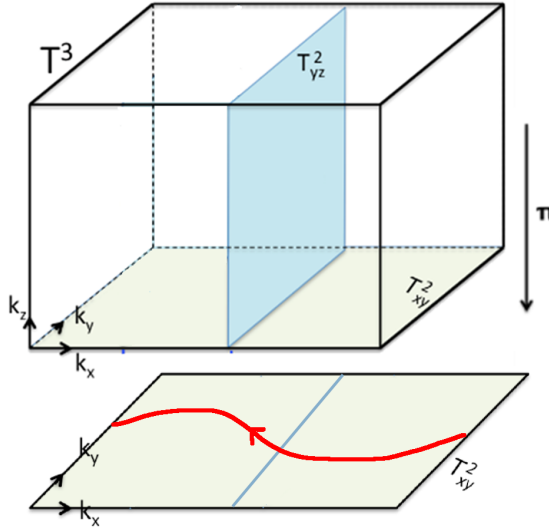


Figure 4.4: Figure adapted from Ref. [32]. The three-dimensional Brillouin torus \mathbb{T}^3 of a Chern insulator is shown, with a two-dimensional slice \mathbb{T}_{yz}^2 indicated in blue. A projection onto a surface Brillouin zone in the xy -direction is also shown, with an example Fermi loop of gapless states in red. In this example, the slice \mathbb{T}_{yz}^2 has a Chern number of $C_x = 1$. Hence, its projection onto the surface is a 1D loop (blue line) that features one chiral band crossing.

there is a Chern number³

$$C_x = \frac{1}{2\pi} \int_{\mathbb{T}_{yz}^2} \mathcal{F}.$$

This results in a classification by three distinct Chern numbers C_x , C_y and C_z , which are commonly arranged in a so-called *Chern vector*

$$\mathbf{C} = \begin{pmatrix} C_x \\ C_y \\ C_z \end{pmatrix} \in \mathbb{Z}^3.$$

Importantly, these three Chern numbers are all induced by a single two-form \mathcal{F} . In this sense, there is an exact correspondence between topologically distinct Berry curvatures \mathcal{F} and Chern vectors $\mathbf{C} \in \mathbb{Z}^3$. This is precisely what motivates the use of cohomology for classification: just like in the 2D Chern insulator, the two-form \mathcal{F} can be considered to represent a class in the second cohomology group,⁴

$$[\mathcal{F}] \in H^2(\mathbb{T}^3) \cong \mathbb{Z}^3. \quad (4.4)$$

³Note that it does not matter where along the Brillouin zone the yz -slice \mathbb{T}_{yz}^2 is taken: the Chern number is an integer, while the system is continuous. This means the x coordinate can be changed continuously without changing the resulting Chern number.

⁴As explained in Section 2.2.2, \mathcal{F} more properly represents a class in the real-valued *de Rham cohomology* group $H_{dR}^2(\mathbb{T}^3) \cong \mathbb{R}^3$. The analogy is strong enough to be considered direct here, but de Rham cohomology is too plain to encode features such as \mathbb{Z}_2 invariants. This is why we make use of the richer integer-valued cohomology theory.

As a result, this group precisely classifies the distinct topological phases of the system.⁵

Boundary states

Before moving on to a system with Weyl points, it will be instructive to study the gapless modes that arise on the surface of a 3D Chern insulator with non-zero Chern vector. Figure 4.4 illustrates the case where $\mathbf{C} = (1, 0, 0)^\top$. In this case, \mathbb{T}_{yz}^2 is the only orthogonal slice with a non-zero Chern number, and as such the material lattice can be thought of as a stack of 2D Chern insulators spanning the y and z directions, stacked together in the x direction. \mathbb{T}_{yz}^2 can effectively be considered the Brillouin zone of such a 2D Chern insulator.

Recall from our discussion in Section 3.4.1 that a 2D Chern insulator with a Chern number of 1 has a single chiral edge mode, which manifests as a gapless state on the one-dimensional surface Brillouin zone. This logic can be translated to the three-dimensional case, where such slices are stacked in the x direction. Suppose there is a projection π along the z direction, onto a two-dimensional surface Brillouin zone $\widetilde{\mathbb{T}}_{xy}^2$. Then the two-dimensional slices \mathbb{T}_{yz}^2 project down to a one-dimensional loop $\pi(\mathbb{T}_{yz}^2) \cong S^1$ containing a single point-like gapless state. As the \mathbb{T}_{yz}^2 slice is moved around in the x direction, this band crossing point moves continuously along the y direction, by continuity of the Hamiltonian. It follows that the full two-dimensional surface Brillouin zone must contain a loop of gapless states going across the x direction, as depicted in the figure. This loop is called a *Fermi loop*, in analogy with the Fermi arcs in a Weyl semimetal. Moreover, the chirality of the edge modes can be used to assign a consistent orientation to this loop.

Fermi loops admit a natural topological description in terms of homology. Being oriented loops, they precisely represent a class in the first homology group $H_1(\widetilde{\mathbb{T}}^2)$ of the surface Brillouin zone. Furthermore, it is possible to define an oriented *Dirac loop* ℓ in the bulk Brillouin zone in such a way that its projection $\pi(\ell)$ onto the surface in any direction is exactly the Fermi loop. This loop ℓ is not a gapless feature,⁶ but it is rather interesting topologically: it represents a first homology class in the bulk Brillouin zone,

$$[\ell] \in H_1(\mathbb{T}^3) \cong \mathbb{Z}^3.$$

It is not a coincidence that this first homology group is isomorphic to the second cohomology group $H^2(\mathbb{T}^3)$ from Equation (4.4). This equivalence is a result of *Poincaré duality*, which is the statement that for any closed oriented d -dimensional manifold M , the isomorphism

$$H_n(M) \cong H^{d-n}(M)$$

⁵More fundamentally, a complex vector bundle called the *valence bundle* can be associated to a gapped Hamiltonian, and the second cohomology group classifies the different complex vector bundles over a manifold.

⁶Dirac loops do still admit a physical interpretation: they represent points at which the Berry connection \mathcal{A} has a gauge singularity. Such singularities depend on the choice of gauge, meaning the loop can be moved around by gauge transformations; however, this does not change their topology. The same goes for the Dirac strings that will be discussed in a moment.

holds for any integer n . In the present case, this duality can be stated intuitively in terms of Chern numbers, which count the number of signed intersections of the Dirac loop with the different two-dimensional slices of the Brillouin zone.⁷ This duality can be summarised schematically as follows:

$$H^2(\mathbb{T}^3) \ni [\mathcal{F}] \xrightleftharpoons{\text{integration}} \mathbf{C} \xrightleftharpoons{\text{intersections}} [\ell] \in H_1(\mathbb{T}^3). \quad (4.5)$$

This Poincaré duality ensures that the classifications in terms of first homology and second cohomology are completely equivalent in this case. Importantly, however, Poincaré duality depends on orientability, and it will not hold when we consider non-orientable Brillouin zones in the next chapter. As such, the question of which group provides the right classification of such a system will be key. For the moment, we turn our attention to the topology of Weyl points in the simpler orientable setting.

4.2.2 Topology with Weyl points

Consider a Weyl semimetal with a set of k Weyl points

$$W \equiv \{w_1, w_2, \dots, w_k\} \subset \mathbb{T}^3.$$

Then the charge of a Weyl point w_i is given by the Chern number

$$C_w = \frac{1}{2\pi} \int_{S_w^2} \mathcal{F},$$

where S_w^2 is a sufficiently small 2-sphere centred at w —in particular, it must be small enough to contain no other Weyl points in its interior. Naively, this might lead us to expect that a semimetal phase is classified by the second cohomology group of the collection of all these spheres:

$$H^2\left(\bigcup_{i=1}^k S_{w_i}^2\right) \cong \bigoplus_{i=1}^k H^2(S_{w_i}^2) \cong \mathbb{Z}^k. \quad (4.6)$$

However, this classification runs into two problems: it ignores the global cancellation of charge, and it also ignores the additional topology on two-dimensional slices discussed in the previous subsection. Both of these issues are due to the fact that this group only captures the *local* topology near each Weyl point, and they can be addressed by studying how the different Chern numbers on the Brillouin zone must relate to each other *globally*.

The Nielsen–Ninomiya charge cancellation theorem is one such global relation. It is the statement that all the Chern numbers on these 2-spheres must add to zero:

$$\sum_{i=1}^k C_{w_i} = 0. \quad (4.7)$$

⁷In general, it is possible that a single Dirac loop “folds back on itself” and intersects such a slice more than once. However, any additional intersections introduced in this way always come in oppositely-oriented pairs, leaving the topology unchanged.

This cancellation can be demonstrated using Stokes' theorem. The argument goes as follows: imagine that the interior of each sphere $S_{w_i}^2$ (i.e. a small open 3-ball centred at w_i) is removed from \mathbb{T}^3 . The resulting 3-manifold X looks like a 3-torus with k small ball-shaped holes, and its boundary is given by the collection of spheres:

$$\partial X = - \bigcup_{i=1}^k S_{w_i}^2,$$

where the minus sign induces the correct orientation. Then Stokes' theorem gives

$$0 = \frac{1}{2\pi} \int_{\partial X} d\mathcal{F} = - \sum_{i=1}^k \frac{1}{2\pi} \int_{S_{w_i}^2} \mathcal{F} = - \sum_{i=1}^k C_{w_i},$$

which is precisely the Nielsen–Ninomiya theorem.

A similar argument can also be applied to study what happens to Chern numbers on two-dimensional slices of the Brillouin zone in this context. This argument is illustrated in Figure 4.5. Here, two slices \mathbb{T}_L^2 and \mathbb{T}_R^2 are placed on either side of

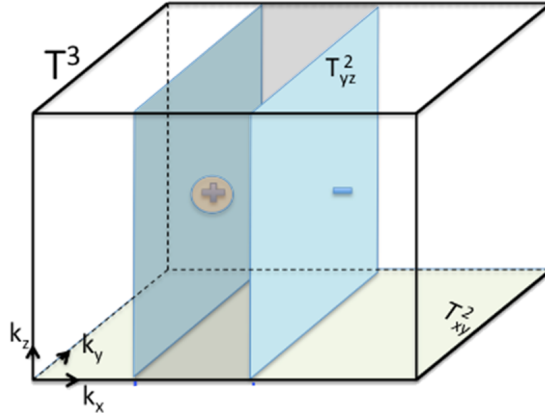


Figure 4.5: Brillouin torus \mathbb{T}^3 of a Weyl semimetal with two oppositely charged Weyl points labelled + and -. Three two-dimensional subspaces are indicated in blue: a yz -like 2-torus on either side of the + point, and a small 2-sphere surrounding it. Given the proper orientation, the blue spaces form the boundary of a three-dimensional manifold Y , shaded in grey here. Figure from Ref. [32]. [not yet licensed; may need better labelling]

a Weyl point w with charge $C_w = q$, along with a small sphere S_w^2 surrounding it. These spaces then bound a three-dimensional manifold Y as indicated in the figure, given the following orientations:

$$\partial Y = \mathbb{T}_R^2 - \mathbb{T}_L^2 - S_w^2.$$

The same Stokes' theorem argument can then be used to relate the Chern numbers C_L and C_R on the respective slices, yielding

$$C_R = C_L + C_w = C_L + q.$$

That is, the Chern number of a two-dimensional slice increases by q every time it passes over a Weyl point with charge q . As a sanity check, it should be noted that this process respects the periodicity of the Brillouin torus: when the slice is passed over the entire torus, charge cancellation ensures that the added Chern number is zero in total.

All in all, the presence of Weyl points allows for a finer collection of Chern numbers to appear in the Brillouin zone, beyond the \mathbb{Z}^3 Chern vector of the insulating case. This behaviour can be captured using cohomology. The key idea is that the Berry curvature has a singularity at points where the gap closes.⁸ As such, it can only be integrated over subspaces where the gap never closes, so that the set of Weyl points W needs to be excluded. This means \mathcal{F} now lives in the second cohomology group of the Brillouin zone minus W :

$$[\mathcal{F}] \in H^2(\mathbb{T}^3 \setminus W) \cong \mathbb{Z}^3 \oplus \mathbb{Z}^{k-1}, \quad (4.8)$$

where k again is the number of Weyl points. Put differently, classification of semimetallic phases given a set of Weyl points W essentially amounts to classifying the gapped phases on the punctured torus $\mathbb{T}^3 \setminus W$.

Notably, this classification addresses both issues present in the \mathbb{Z}^k classification on 2-spheres in Equation (4.6). Firstly, it incorporates 3D Chern insulator topology in the first term, in the form of the \mathbb{Z}^3 from Equation (4.4). Perhaps more subtly, charge cancellation is also incorporated in the form of the reduction by one \mathbb{Z} factor in the second term. This can be understood intuitively: for example, if $k = 1$ then the Nielsen–Ninomiya theorem implies that the single Weyl point must have a charge of 0, and so it is not topologically protected. A similar intuition holds for larger k , in that the k “degrees of freedom” which are afforded to the system by the Weyl point charges are reduced by one under the charge cancellation condition. This relation will become more explicit once the Mayer–Vietoris sequence is introduced in Section 4.2.3.

Fermi arcs

The varying Chern numbers over Weyl points help explain how Fermi arcs arise on the surface. As discussed in the case of a 3D Chern insulator, Fermi loops on the surface arise whenever there is a non-zero Chern number in some direction. Similarly, Fermi arcs begin and terminate whenever the presence of a Weyl point causes a change in the Chern number; this is illustrated in Figure 4.6.

This feature of Weyl semimetals implies they can mediate phase transitions between 3D Chern insulators with different Chern vectors. For example, suppose a pair of Weyl points is created at some point in the Brillouin zone of a trivial insulator ($\mathbf{C} = 0$). These points can then be moved apart in the z direction until they meet again and annihilate at the other end of the torus. In the process, a Fermi arc extends between the projections of the Weyl points on the xz and yz -planes, which eventually closes into a Fermi loop. In its final state, the system features a non-zero Chern vector of $\mathbf{C} = (0, 0, 1)^T$.

⁸Note that this singularity is required in order for the Chern number to change suddenly when a slice (i.e. the integration domain of \mathcal{F}) is moved over a Weyl point continuously.

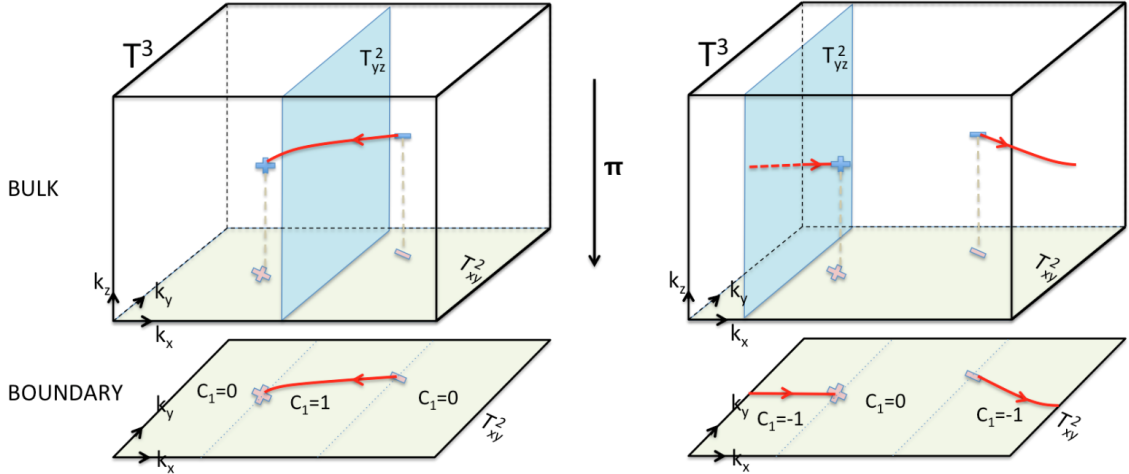


Figure 4.6: Two semimetal Brillouin zones are shown with the same configuration of Weyl points, but featuring topologically distinct Fermi arcs (shown in red on the boundary). The distinction is due to different bulk Chern numbers: Fermi arcs appear in regions where the bulk Chern number is non-zero. These Fermi arcs can be considered to be the projection of a Dirac string (shown in red in the bulk). Figure from Ref. [32].

This process was first observed experimentally in a seminal work by Gui-Geng Liu et al. in 2022 [31]. The authors construct a photonic crystal, which is a type of artificial crystal where the different energy levels are represented by frequencies of light. Under application of a magnetic field, this crystal undergoes a transition between trivial and topological insulating phases, mediated by the creation and annihilation of two Weyl points; see Figure 4.7. This was also the first experimental realisation of a 3D Chern insulator, and of a system featuring a single Fermi arc.

Just as Fermi loops can be considered projections of a bulk Dirac loop, so too can Fermi arcs be considered a projection of a bulk *Dirac string*.⁹ Like Dirac loops, these strings can be given an interpretation in terms of homology. The setup is somewhat more subtle in this case: since the Dirac strings have a boundary, they are not loops and as such do not represent homology classes in $H_1(\mathbb{T}^3)$. Instead, they represent classes in the *relative homology group*

$$H_1(\mathbb{T}^3, W) \cong \mathbb{Z}^3 \oplus \mathbb{Z}^{k-1} \quad (4.9)$$

with respect to the set of Weyl points $W \subset \mathbb{T}^3$. Intuitively, taking the relative homology means that any boundaries lying in the subset W are ignored; for a more precise definition the reader is referred to Ref. [1, §2.1].

This homology picture provides a classification scheme that is exactly dual to the cohomology classification in Equation (4.8); that is, there is an isomorphism

$$H^2(\mathbb{T}^3 \setminus W) \cong H_1(\mathbb{T}^3, W). \quad (4.10)$$

⁹A more or less equivalent concept is referred to as *Euler chain* in Ref. [32], placing the emphasis on topology over physics: “chain” here refers the oriented subspaces that homology is founded on.

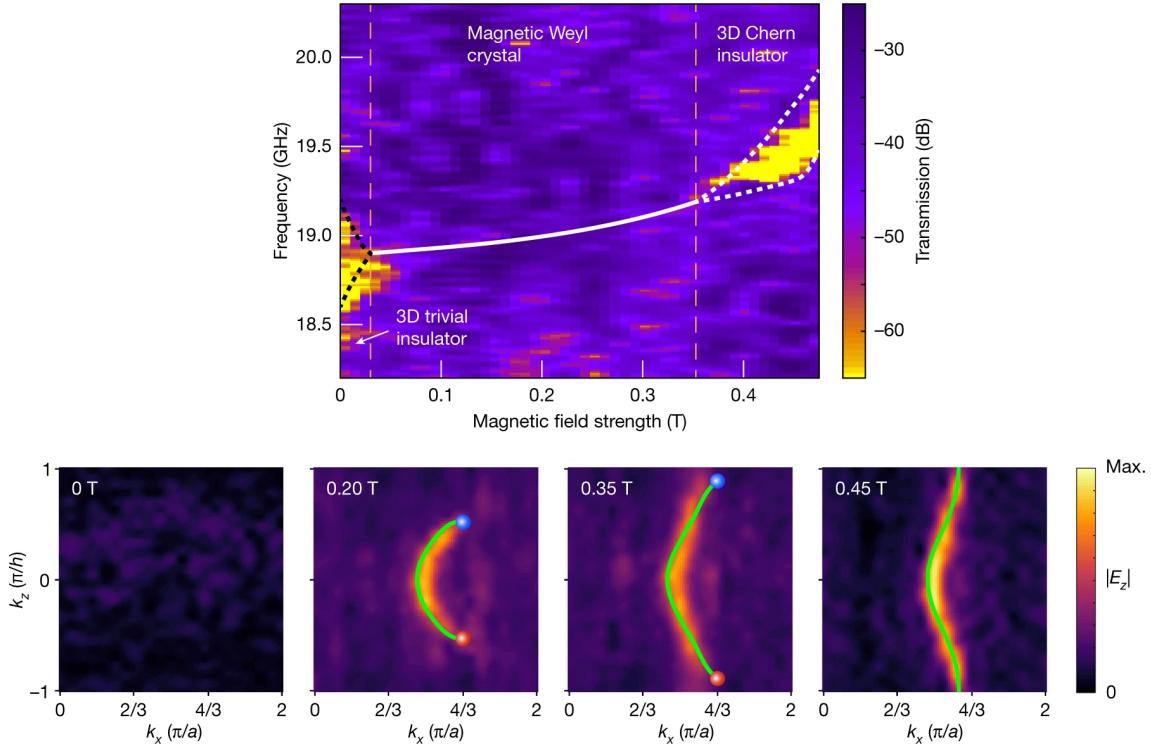


Figure 4.7: Figure from Ref. [31], reproduced with permission from Springer Nature. Top: measured frequency response (i.e. “band structure”) at increasing magnetic field strength. Yellow regions represent a band gap in the spectrum, indicating insulating phases. The white line represents the calculated frequency of the two Weyl nodes in the system. Bottom: measured response on a surface Brillouin zone, at the frequencies indicated on the white line above. Simulated Fermi arcs and loops are shown in green. A Fermi loop can clearly be seen to form, confirming a phase change to a topological insulator.

This is not a direct Poincaré duality, but it is nevertheless mathematically rigorous and protected by orientability in the same way.¹⁰ The interpretation in terms of Chern numbers given in Equation (4.5) also still holds here, with the Chern vector and Dirac loops replaced with more general Chern numbers and Dirac strings, respectively.

4.2.3 The semimetal Mayer–Vietoris sequence

In the previous section, a heuristic Stokes’ theorem argument was presented for charge cancellation on Weyl points. This argument can be generalized by moving to a more abstract cohomology setting, where we are not dependent on the integration of forms; this is important because integration will not be well defined once we move

¹⁰To be precise, Poincaré duality does not hold directly because $T^3 \setminus W$ is not a closed manifold. Instead, for non-compact manifolds M there is a generalized duality $H^n(M) \cong H_{d-n}^{\text{BM}}(M)$ where the group on the right is the *Borel–Moore homology*, and this is in turn equivalent to the relative homology in this case. Alternatively, Equation (4.10) can be interpreted as a result of the so-called *Lefschetz duality* $H^n(M) \cong H_{d-n}(M, \partial M)$ for manifolds with a boundary.

to a non-orientable setting. As an added bonus, the abstract description proves to be richer and provide more detailed information on the possible topological phases for a Weyl semimetal.

The idea is that the relation between the global semimetal topology in Equation (4.8) and the local charge data in Equation (4.6) can be understood by considering how cohomology classes are mapped between them. That is, one needs to find and study a homomorphism

$$\beta : H^2(\mathbb{T}^3 \setminus W) \rightarrow \bigoplus_{w \in W} H^2(S_w^2).$$

Such a map arises naturally in the context of the *Mayer–Vietoris sequence* for cohomology.

Mayer–Vietoris sequences are used to study how the homology or cohomology of a topological space relates to that of its subspaces. To be precise, let X be a topological space and let $A, B \subset X$ be two subspaces that cover it (i.e. $A \cup B = X$). Then, there is an *exact sequence* of homomorphisms between cohomology groups,

$$\cdots \rightarrow H^n(X) \rightarrow H^n(A) \oplus H^n(B) \rightarrow H^n(A \cup B) \rightarrow H^{n+1}(X) \rightarrow \cdots,$$

which continues indefinitely in both directions. Exactness means that the image of each map in the sequence is exactly equal to the kernel of the next. In other words, the elements in each term in the sequence which are mapped to zero in the next term are precisely those which “descend” from the previous term. In particular, the composition of two subsequent maps always yields zero.

In the context of a Weyl semimetal, there is a natural way to divide the Brillouin torus \mathbb{T}^3 into two subspaces; this is illustrated in Figure 4.8. The first subspace in the covering is the punctured torus $\mathbb{T}^3 \setminus W$; we have already encountered this space in classifying topological semimetal phases. The other is the collection $\bigcup_{i=1}^k D_{w_i}^3$ of small open 3-balls centred on the Weyl points w_i . The intersection of these two spaces is the same collection of open balls, but each with a single puncture. For our purposes, this intersection has the same topology as the collection of 2-spheres $\bigcup_{i=1}^k S_{w_i}^2$ that we encountered in the context of local Weyl point charges.¹¹ A Mayer–Vietoris sequence can now be written down for these subspaces. The section of this sequence which is relevant to classification is referred to as the *semimetal Mayer–Vietoris sequence*:¹²

$$0 \rightarrow \underbrace{H^2(\mathbb{T}^3)}_{\text{3D Chern insulator}} \rightarrow \underbrace{H^2(\mathbb{T}^3 \setminus W)}_{\text{Semimetal}} \xrightarrow{\beta} \underbrace{\bigoplus_{w \in W} H^2(S_w^2)}_{\text{Local charges}} \xrightarrow{\Sigma} H^3(\mathbb{T}^3) \rightarrow 0. \quad (4.11)$$

The first three groups in this sequence are already familiar from Equations (4.4), (4.8), and (4.6) respectively. [The comma before respectively is not necessary in British English, which I’m writing in (similarly for things like i.e. and e.g.)] The

¹¹To be precise, the punctured 3-balls can be *deformation retracted* into the 2-spheres, making them *homotopy equivalent*. Homotopy equivalent spaces have the same homology and cohomology groups.

¹²Note that the open balls $D_{w_i}^3$ do not appear in this sequence at all. This is because they can be contracted to a point, and hence are topologically trivial in a sense.

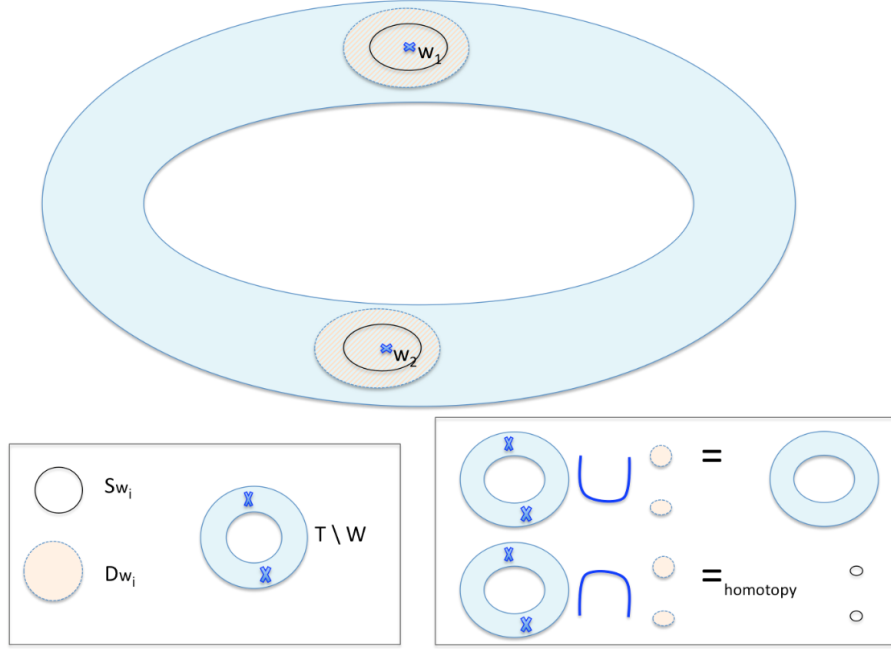


Figure 4.8: Schematic two-dimensional representation of the Brillouin torus and the subspaces used to cover it. Figure from Ref. [36].

last group $H^3(\mathbb{T}^3) \cong \mathbb{Z}$ is represented by volume forms¹³ on the torus; one notable example of such a form is the trivial 3-form

$$d\mathcal{F} = 0 \in H^3(\mathbb{T}^3)$$

which appeared in the Stokes' theorem arguments previously. Indeed, the map labelled Σ above can be loosely interpreted as the exterior derivative d . However, a more physically useful interpretation is that Σ gives the total charge in the system: it sends a set of Chern numbers on the Weyl points to their sum in \mathbb{Z} .

Explicitly, the semimetal Mayer–Vietoris sequence is¹⁴

$$0 \rightarrow \mathbb{Z}^3 \rightarrow \mathbb{Z}^3 \oplus \mathbb{Z}^{k-1} \xrightarrow{\beta} \mathbb{Z}^k \xrightarrow{\Sigma} \mathbb{Z} \rightarrow 0. \quad (4.12)$$

The exactness of this sequence can be used to extract useful information, especially around the group of local charges \mathbb{Z}^k . Here, exactness means that $\text{im}(\beta) = \ker(\Sigma)$. This implies that the local charges on the Weyl points sum to zero if and only if they descend from a semimetal. In other words, it implies not only the Nielsen–Ninomiya charge cancellation theorem, but also its converse: any set of Weyl points with charges adding to zero is admissible as a topological Weyl semimetal phase.

In fact, more can be inferred by looking at the maps around the semimetal group $\mathbb{Z}^3 \oplus \mathbb{Z}^{k-1}$. Here, exactness tells us that $\ker(\beta) \cong \mathbb{Z}^3$. This makes physical sense: if all local charges are zero, the Weyl points are not topologically protected and the system is really in a 3D Chern insulator phase. However, since β is a homomorphism,

¹³I.e. 3-forms, which are locally proportional to $dk_x \wedge dk_y \wedge dk_z$.

¹⁴In principle the direct sum in the semimetal group has little mathematical significance; we write $\mathbb{Z}^3 \oplus \mathbb{Z}^{k-1}$ instead of \mathbb{Z}^{k+2} to aid the physical interpretation.

we also find $\beta^{-1}(c) \cong \mathbb{Z}^3$ for a generic charge configuration $c \neq 0 \in \mathbb{Z}^k$; that is, every configuration with total charge zero admits a \mathbb{Z}^3 worth of topologically different semimetal phases. This makes precise a principle that is also hinted at in Figure 4.6: Weyl semimetals with identical charge configurations may nevertheless be topologically distinct, and their topologies differ by a bulk Chern vector in \mathbb{Z}^3 .¹⁵

The dual homology sequence

In previous subsections, we have already seen that the cohomology invariants on Chern insulators and Weyl semimetals can be understood equally well in terms of homology groups. As it turns out, this duality can be extended to the semimetal Mayer–Vietoris sequence (4.11). The dual of the first two groups was already explored in Equations (4.5) and (4.10). The latter two groups act on closed manifolds, and so their dual can be obtained from Poincaré duality directly:

$$\bigoplus_{w \in W} H^2(S_w^2) \cong \bigoplus_{w \in W} H_0(S_w^2), \quad H^3(\mathbb{T}^3) \cong H_0(\mathbb{T}^3).$$

In both cases, we have a top-dimensional cohomology group (containing volume forms) being dualised to a zeroth homology group, which counts the number of connected components. In particular, since the connected components are the important aspect, the 2-spheres S_w may be substituted for the Weyl points w to simplify:

$$\bigoplus_{w \in W} H_0(S_w^2) \cong \bigoplus_{w \in W} H_0(w) \cong H_0(W).$$

The complete homology dual of (4.11) is then

$$0 \rightarrow \underbrace{H_1(\mathbb{T}^3)}_{\text{Dirac loops}} \rightarrow \underbrace{H_1(\mathbb{T}^3, W)}_{\text{Dirac strings}} \xrightarrow{\partial} \underbrace{H_0(W)}_{\text{Local charges}} \xrightarrow{\Sigma} H_0(\mathbb{T}^3) \rightarrow 0. \quad (4.13)$$

This exact sequence has arisen through taking Poincaré duals of groups in the Mayer–Vietoris sequence, but somewhat miraculously, it continues to be valid even in the absence of Poincaré duality (e.g. on a non-orientable manifold). In fact, it can be considered a more fundamental sequence in some ways: it describes the homology of the torus with respect to a single subspace W , whereas the Mayer–Vietoris sequence relies on multiple subspaces that cover the torus.¹⁶

The map indicated by ∂ is the boundary map that is used to define homology groups in the first place.¹⁷ In this case, it sends classes of oriented Dirac strings in the bulk to the Weyl points that bound them, with a sign given by which end of the

¹⁵Properly speaking, the set of topological phases for a given charge configuration is an affine space for $H^2(\mathbb{T}^3)$, since there is no canonical zero Chern vector on a Weyl semimetal. This is worked out in greater mathematical detail in Section 3 of Ref. [32].

¹⁶Indeed, this is the first exact sequence introduced in the standard algebraic topology textbooks, e.g. in Theorem 2.13 of Ref. [1].

¹⁷To be precise, homology is defined using boundaries of chains; the present map is the *pushforward* of the boundary map, and one can think of it as acting on the chains that represent different homology classes.

string the points are on. For example, for a Weyl semimetal with two Weyl points $W = \{w_1, w_2\}$ connected by a Dirac string s , we have $[s] \in H_1(\mathbb{T}^3, W)$ and

$$\partial([s]) = (1, -1) \in H_0(W) \cong \mathbb{Z}^2.$$

This gives rise to a very natural interpretation of charge cancellation: it automatically follows from the fact that Weyl points on opposite ends of a Dirac string are assigned opposite signs. These opposite charges are then summed to zero by the total charge map Σ , i.e. $\Sigma \circ \partial = 0$. This can also be inferred from the exactness of (4.13), which additionally tells us that there exists a configuration of Dirac strings compatible with any set of Weyl points with total charge zero.

As emphasised before, this homology sequence encodes exactly the same information as the cohomology Mayer–Vietoris sequence in the simple case where Poincaré duality is preserved. However, once symmetries are imposed on the system, this duality may be altered, in which case the two basic sequences become essentially different. It then becomes necessary to study how the cohomology and/or homology groups must be altered to encode relevant information about the topological phases of the system. We will review one example of this in the next section.

4.2.4 Time-reversal symmetric Weyl semimetals

The preceding topological review of Weyl semimetals has thus far been in the context of the basic symmetry class A—that is, we have not imposed any additional symmetries on the system. However, such additional symmetries are not necessarily forbidden in a Weyl semimetal: the type A classification merely tells us that the semimetal topology is very robust, not relying on any symmetry protection.¹⁸ As discussed in Section 4.1, all of the experimentally observed electronic Weyl semimetals actually preserve time-reversal symmetry, which is a natural condition in the absence of a magnetic field. An excellent topological description of such systems was published by Guo Chuan Thiang, Koji Sato and Kiyonori Gomi in 2017, and we will spend the rest of this section reviewing its main aspects [36].

Time-reversal symmetric systems belong to class AII of the tenfold way classification in Table [cite table], meaning the underlying insulating topology (i.e. the topology with zero Weyl points) is that of the strong and weak insulators described in Section 3.4.3. This means the four \mathbb{Z}_2 invariants (three weak and one strong) in such systems also play a role in the semimetal topology. Just as class A Weyl semimetals can be considered intermediate phases between different 3D Chern insulators (as shown in Figure 4.7), it is shown in Ref. [36] that class AII semimetals can mediate phase transitions between different strong and weak 3D insulators via Weyl point creation and annihilation.

As discussed in Section 4.1, time reversal symmetry squaring to $T^2 = -1$ forces Weyl points to appear in Kramers pairs of the same chirality, related by $\mathbf{k} \leftrightarrow -\mathbf{k}$ in the Brillouin zone. The topology induced by the presence of these pairs must also respect the symmetry, and as such it cannot be studied by simply moving integration planes freely over the individual Weyl points (as previously shown in

¹⁸By contrast, for example, the SSH model introduced in Section 3.2 has chiral symmetry-protected topological phases.

Figure 4.5). Indeed, recall from Section 3.4.3 that the insulating \mathbb{Z}_2 invariants must be calculated specifically at the T-invariant planes sitting at $k_{x,y,z} \in \{0, \pm\pi\}$. To study how Kramers pairs affect these invariants, their respective planes must be continuously deformed across them in a way that respects the symmetry, leading to the concept of *curved T-planes*; see Figure 4.9.

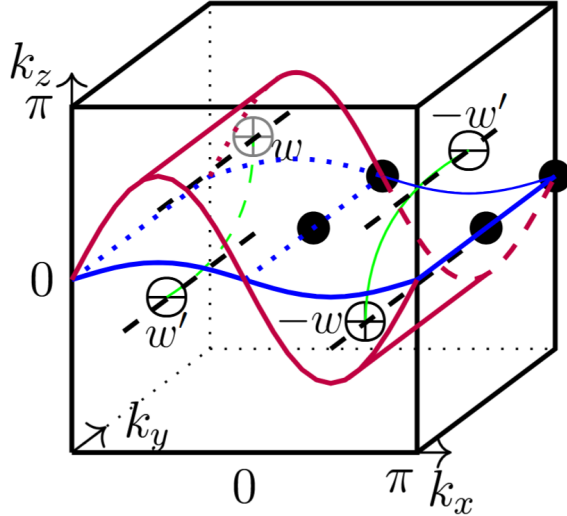


Figure 4.9: Figure from Ref. [36]. Curved T-planes are shown in blue and purple; both are deformations of the $k_z = 0$ plane. Deforming the blue plane into the purple one makes it cross the Kramers pair at $\mathbf{k} = \pm w$. This induces a change in the related \mathbb{Z}_2 invariant: if the Weyl points in this pair have individual charges of q , then the invariants on these planes are related by $\Delta_{z,0}^{\text{purple}} \equiv \Delta_{z,0}^{\text{blue}} + q \pmod{2}$.

The cohomology description must be altered in several ways in order to accommodate this more complex topology. First of all, the cohomology classes must respect the $\mathbf{k} \leftrightarrow -\mathbf{k}$ symmetry on the Brillouin zone, leading to the use of *equivariant* cohomology groups $H_{\mathbb{Z}_2}^n$, where the \mathbb{Z}_2 stands for the \mathbb{Z}_2 action of the symmetry. Mathematically, this is similar in spirit to studying the topology of the *effective Brillouin zone* covering half the torus \mathbb{T}^3 , obtained from the quotient $\mathbb{T}^3/\mathbb{Z}_2$ of the symmetric action. However, the presence of high-symmetry points means some topological information is lost in passing to this effective Brillouin zone, and so a somewhat more involved construction called the *homotopy quotient* must be employed instead.¹⁹

Secondly, the non-trivial topology existing at the time-reversal invariant momenta (TRIM) necessitates that the cohomology groups be calculated relative to these points. This relative cohomology is defined in much the same way as the relative *homology* featured in Equation (4.9).

¹⁹This homotopy quotient is obtained from the *Borel construction*, relying on the fact that there is always a contractible space EG (the total space of the so-called *universal bundle*, in this case S^∞) on which the symmetry group G acts freely. The product space $EG \times \mathbb{T}^3$ is then homotopy equivalent to \mathbb{T}^3 , but the diagonal action has no fixed points. Equivariant cohomology is defined as the cohomology of the quotient space of this action: $H_G^n(\mathbb{T}^3) := H^n(EG \times_G \mathbb{T}^3)$.

Lastly, the cohomology must be *twisted*; that is, it is endowed with *local coefficients* $\tilde{\mathbb{Z}}$, which change sign under the \mathbb{Z}_2 action of the symmetry. We will provide a more geometric intuition behind these local coefficients in Section 5.2.

All in all, the regular cohomology groups in the Mayer–Vietoris sequence in Equation (4.11) must be changed to rather complicated *twisted equivariant* cohomology relative to the TRIM. For example, the insulating invariants (i.e. Chern vectors) in $H^2(\mathbb{T}^3) \cong \mathbb{Z}^3$ are altered to

$$H_{\mathbb{Z}_2}^2(\mathbb{T}^3, \text{TRIM}; \tilde{\mathbb{Z}}) \cong \mathbb{Z}_2^4,$$

containing precisely the four \mathbb{Z}_2 invariants: three weak and one strong. The use of this form of cohomology is motivated in Ref. [36] by the classification of so-called “Quaternionic” vector bundle structures on the Brillouin zone, which are a modification of the usual complex vector bundles induced by the $T^2 = -1$ symmetry [37, 38].

The dual homology picture is considerably simpler in this case. The only modification necessary to the groups in the homology sequence in Equation (4.13) is the use of equivariant homology $H_n^{\mathbb{Z}_2}$; that is, instead of generic Dirac loops and strings, the homology classes must be represented by their *T-stable* variants which respect the $\mathbf{k} \leftrightarrow -\mathbf{k}$ symmetry and avoid the TRIM. Just as in the type A system, this leads to an intuitive description of the associated invariants; see for example Figure 4.10.

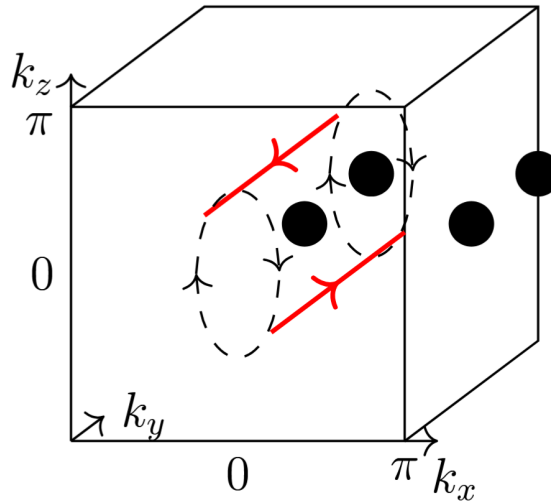


Figure 4.10: Figure from Ref. [36]. A T -stable pair of oriented Dirac loops l_y is shown spanning the k_y direction. The loops may be interchanged while maintaining T -stability, by rotating them along the dashed lines. Doing so recovers the original pair with opposite orientation. It follows that $l_y = -l_y$, that is, $2l_y = 0$; as a result, l_y generates a \mathbb{Z}_2 invariant, dual to the cohomology invariant ν_y .

Calculated using either homology or cohomology, the semimetal Mayer–Vietoris sequence takes on the following explicit form in a class AII system:

$$0 \rightarrow \mathbb{Z}_2^4 \rightarrow \mathbb{Z}_2^4 \oplus \mathbb{Z}^{r-1} \xrightarrow{\beta} \mathbb{Z}^r \xrightarrow{\Sigma} \mathbb{Z} \rightarrow 0, \quad (4.14)$$

where in this case, r labels the number of Kramers pairs rather than individual Weyl points. Its features are very much analogous to the class A sequence in Equation (4.12): it is essentially obtained by substituting the \mathbb{Z}^3 relating to insulating Chern vectors with a \mathbb{Z}_2^4 indexing the weak and strong invariants. Just as before, the map Σ can be used to deduce Nielsen–Ninomiya charge cancellation, and the semimetal group $\mathbb{Z}_2^4 \oplus \mathbb{Z}^{r-1}$ combines the insulating invariants on the left with a \mathbb{Z}^{r-1} representing the set of allowed Weyl point charge configurations. The main difference from the class A case is that the topology is framed in terms of pairs of Weyl points, and as such the minimum number of Weyl points is four instead of two—as we also covered in the physical setting of Section 4.1.

One might reasonably question whether the classification of Weyl semimetals with additional symmetries always comes down to a mere change in the underlying insulating topology, as it does in this case. In Chapter 5, we will discuss a counterexample to this: we show that the Mayer–Vietoris sequence is altered more radically under a symmetry which has previously been demonstrated to induce novel semimetal topology.

Chapter 5

Non-orientable systems

Symmetries play a crucial role in establishing and differentiating topological properties of physical systems; this is attested by the tenfold way classification discussed in Section 3.3. However, in recent years researchers have begun to recognise that symmetries beyond the standard time reversal, charge conjugation and chiral symmetries can give rise to distinct topological invariants that are not fully captured by this classification.

An important class of these extended symmetries is comprised by the space groups acting on periodic lattices. These impose additional structure on the unit cell of the lattice, such as rotational or reflection symmetry. Of special interest here are the so-called *non-symmorphic* space group symmetries, which combine basic rotation, reflection or inversion with a fractional lattice translation. These symmetries have no fixed points and may induce novel topological states when applied to a material lattice. This type of symmetry has been studied extensively in real space [39–50]; a review can be found at Ref. [51].

Very recently, the feasibility of applying these non-symmorphic symmetries in momentum space has been demonstrated both theoretically and experimentally. This opens up new and interesting avenues of research relating to Brillouin zone topology. In particular, the Brillouin zone may become effectively non-orientable, challenging the notion of chirality for Weyl points.

We begin this chapter with a short review of existing literature surrounding these momentum-space non-symmorphic symmetries in Section 5.1, culminating in a treatment of a recent paper which applies them to Weyl semimetals. We then present a novel topological analysis of the system described in this paper in Section 5.2, in terms of the cohomology and homology tools presented in Chapter 4. Finally, in Section 5.3, we provide a full classification of Weyl semimetal phases on all possible non-orientable Brillouin zones in three dimensions.

5.1 Review of recent literature

Non-symmorphic symmetries have been studied somewhat extensively in real space, but their momentum space counterparts have long eluded study. There is a practical reason for this: normally, any space group symmetry in real space gives rise to a symmorphic (i.e. point group) symmetry in momentum space after Fourier transform-

mation, regardless of the nature of the real space symmetry [52]. In order to obtain a non-symmorphic symmetry in momentum space, it is necessary to change how the real-space symmetry group acts on states in the Hilbert space. The reasoning is as follows: a symmetry group G acts on states in the Hilbert space through a representation ρ . This representation is normally a homomorphism, i.e. it obeys

$$\rho(g)\rho(h) = \rho(gh)$$

for $g, h \in G$. However, since quantum states are physically equivalent up to a $U(1)$ phase, the representation ρ may also include $U(1)$ factors:

$$\rho(g)\rho(h) = \nu(g, h)\rho(gh),$$

where $\nu : G \times G \rightarrow U(1)$ is known as a factor system [53]. Such a representation is called *projective*, and it may fundamentally alter the algebraic properties of the symmetry group—for example, it can lead symmetry operations that commute in real space to anticommute instead in Hilbert space. Projective representations have previously been studied in more abstract systems, and may give rise to novel topological phases on their own [53–58]. The usual strategy is to implement *gauge fluxes* on the real-space lattice; these are structures that induce $U(1)$ phase changes in particles hopping around the lattice.

The first theoretical realisation of non-symmorphic momentum space symmetries was published by Z. Y. Chen, Shengyuan A. Yang and Y. X. Zhao in 2022 [59]. In their work, the authors take a lattice with a mirror symmetry M_x and perpendicular translation symmetry L_y , and demonstrate how negative hopping amplitudes may be implemented in such a way that the resulting gauge fluxes make M_x and L_y anticommute rather than commute; see Figure 5.1(a). This anticommutation changes how the mirror operator acts in momentum space: denoting the momentum space operators by \hat{M}_x and $\hat{L}_y = e^{ik_y}$ (assuming unit lattice spacing in the real y direction), anticommutation implies

$$\hat{M}_x e^{ik_y} \hat{M}_x = -e^{ik_y} = e^{i(k_y + \pi)}.$$

That is, \hat{M}_x induces not only a mirroring $k_x \mapsto -k_x$, but also a translation by π in the k_y direction. It follows that the momentum-space Hamiltonian must obey the *glide symmetry*

$$U\mathcal{H}(k_x, k_y)U^\dagger = \mathcal{H}(-k_x, k_y + \pi). \quad (5.1)$$

Crucially, the action of this symmetry is free, i.e. there are no high-symmetry momenta that are fixed by \hat{M}_x . Similar to the way in which the free translation symmetries on the 2D lattice reduce momentum space from \mathbb{R}^2 down to the Brillouin torus \mathbb{T}^2 , this free \mathbb{Z}_2 glide symmetry reduces the torus further down to a *fundamental domain* covering half the torus from $k_y = -\pi$ to $k_y = 0$. Whereas the boundary conditions on the full torus are periodic, this fundamental domain features anti-periodic boundary conditions in the k_y direction, in the sense that the $k_y = -\pi$ and $k_y = 0$ boundaries must be identified with opposite orientations. As such, it assumes the topology of the Klein bottle K^2 , which is a non-orientable surface; see Figure 5.1(b).

This glide symmetric system is found to feature a \mathbb{Z}_2 invariant ν , different from the \mathbb{Z} invariant on the 2D Chern insulators discussed in Section 3.4.1. The difference

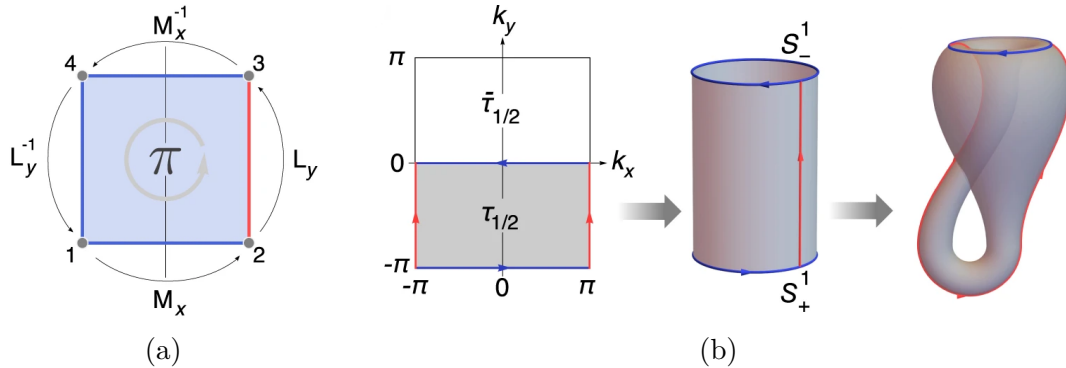


Figure 5.1: Figures adapted from Ref. [59]. (a) A square section of the lattice is shown with a negative hopping amplitude in red. This induces a phase change of π (i.e. a sign change) on a test particle which is moved around the square by successive symmetry operations $L_y^{-1}M_x^{-1}L_yM_x$. The operators M_x and L_y anticommute as a result. (b) The momentum space symmetry \hat{M}_x reduces the Brillouin torus to the fundamental domain shaded in grey on the left. The boundaries of this domain are identified in such a way that it assumes the topology of the Klein bottle K^2 (shown on the right). This surface cannot be given a consistent orientation: one can imagine starting on the outside of the main bulb, entering through the funnel at the top and ending up on the inside.

may be explained in terms of cohomology: the regular Chern number is related to $H^2(\mathbb{T}^2) \cong \mathbb{Z}$, whereas in the case of the Klein bottle, the invariant is classified by $H^2(K^2) \cong \mathbb{Z}_2$. This \mathbb{Z}_2 invariant cannot be stated simply in terms of a Berry curvature integral on the fundamental domain: the boundaries at $k_y = -\pi$ and $k_y = 0$ are identified in opposite directions, and their contributions to the integral no longer cancel by Stokes' theorem. Instead, the invariant takes the following two forms in Ref. [59]:

$$\nu \equiv \frac{1}{2\pi} \int_{\tau_{1/2}} \mathcal{F} + \frac{1}{\pi} \gamma(0) \mod 2 \quad (5.2)$$

$$\equiv \frac{1}{2\pi}[\gamma(0) + \gamma(-\pi)] \mod 2, \quad (5.3)$$

where $\tau_{1/2}$ is the fundamental domain and $\gamma(k_y)$ is the Berry phase over the loop at k_y . These two forms are related by Stokes' theorem, and the modulus 2 is necessary to ensure gauge invariance.¹

In 2023, Chen Zhang et al. (including two of the authors of the aforementioned Klein bottle paper) generalised this theoretical framework [52]. In particular, they specify how to obtain all 157 non-symmorphic symmetries in three dimensions (and all four in two dimensions) from real-space gauge symmetries.

Several experimental verifications of these momentum-space non-symmorphic symmetries were published in 2024: Ref. [60] by Yu-Liang Tao, Mou Yan et al. and

¹Note that in the latter equation, it is important that $\gamma(0)$ and $\gamma(-\pi)$ are both calculated in the same gauge, which must be continuous across the fundamental domain $\tau_{1/2}$.

Ref. [61] by Zhenxiao Zhu et al. In both works, a 3D acoustic lattice is constructed—an artificial crystal in which the band structure is represented by frequencies of sound waves—featuring negative hopping amplitudes, which induce non-symmorphic symmetries in momentum space; see Figure 5.2. These symmetries are shown to give

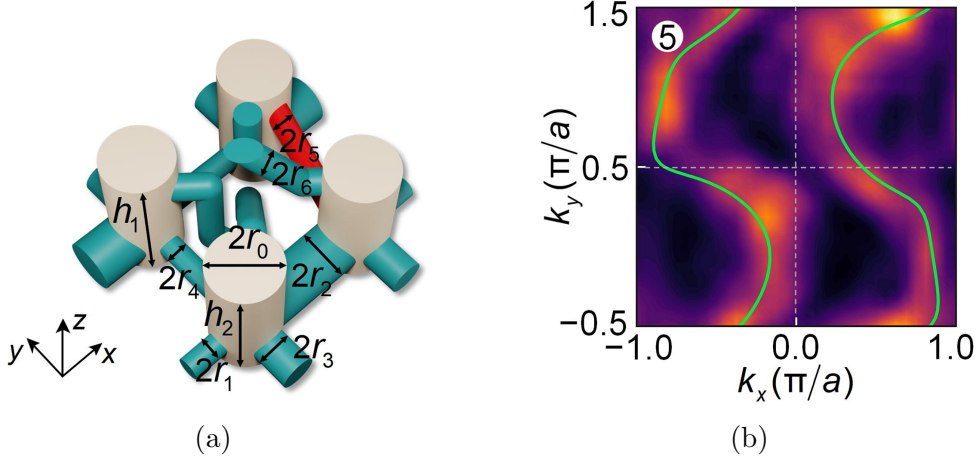


Figure 5.2: Figure adapted from Ref. [61]. (a) Unit cell of the acoustic crystal used in the experiment. The resonant cavities shown in beige approximate tight-binding orbitals in electronic systems, while the coupling tubes in green simulate hopping between lattice sites. The tube indicated in red has an effective negative hopping amplitude. (b) Experimental (colour map) and numeric (green) data from a 2D slice of the system’s Brillouin zone. The figure shows the response to a specific frequency, equivalent to an equal-energy contour (i.e. section of the bands) in an electronic system. This 2D slice features a glide symmetry: the lower half can be obtained by mirroring the upper half in the horizontal k_x direction.

rise to novel topological phases and surface behaviour.

Several other works have explored a specific non-symmorphic symmetry group in two dimensions, where besides the glide symmetry \hat{M}_x giving rise to Equation (5.1), there is also a perpendicular glide symmetry \hat{M}_y in which the roles of k_x and k_y are reversed [62–64]. This double glide symmetry is notable in that, even though the action of each individual glide symmetry \hat{M}_x and \hat{M}_y on the Brillouin torus is free, the combined action of the two is not. Instead, there are four high-symmetry momenta² at $\mathbf{k} = (\pm\pi/2, \pm\pi/2)$ which are fixed under $\hat{M}_y\hat{M}_x$; see Figure 5.3. It is noted in Refs. [62] and [63] that a \mathbb{Z}_2 topological invariant can be calculated based on the eigenvalues of $\hat{M}_x\hat{M}_y$ at these high-symmetry points, similar to the \mathbb{Z}_2 invariants in the time-reversal invariant systems encountered in Section 3.4.

5.1.1 Non-orientable Weyl semimetals

The first work in which non-symmorphic symmetries were explored in the context of Weyl semimetals was a 2024 paper by André Grossi Fonseca, Sachin Vaidya et al.

²In crystallographic terms, the 2D wallpaper group Pgg has four special Wyckoff positions.

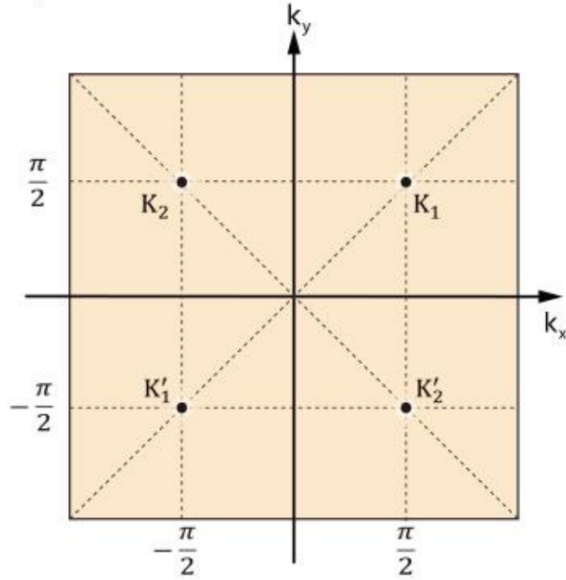


Figure 5.3: Figure from Ref. [63]. The points labelled K_a with $a \in \{1, 2\}$ are related by either single glide symmetry to those labelled K'_a respectively. As a result, applying both symmetries at once fixes all four of these points. The indicated dashed lines are also fixed sets of the combined symmetry.

[12]. The remainder of this section is dedicated to summarizing the main findings in this paper.

The basic setup in Ref. [12] is that of an abstract 3D Brillouin torus featuring a glide symmetry of the form

$$\mathcal{H}(k_x, k_y, k_z) = \mathcal{H}(-k_x, k_y + \pi, k_z); \quad (5.4)$$

no assumptions are made on the source of this symmetry.³ The free action of this symmetry gives rise to a non-orientable fundamental domain: slices of constant k_z take on the topology of the Klein bottle K^2 in the same way as in Ref. [59] discussed above. Taking into account the additional periodic k_z direction, the total fundamental domain is topologically the non-orientable manifold $K^2 \times S^1$; see Figure 5.4. In Ref. [12], the fundamental domain is taken to be the half torus with $k_y \leq 0$, with additional boundary identifications between the planes $k_y = -\pi$ and $k_y = 0$ which respect the symmetry.

The non-orientability of the fundamental domain is shown to lead to some novel properties. Most notably, the chirality of Weyl points is no longer well-defined in a non-orientable setting: for example, when a Weyl point which has a Chern number of -1 leaves the fundamental domain at the $k_y = -\pi$ plane, it returns at the corresponding point on the $k_y = 0$ plane with a Chern number of $+1$. Physically, this is because the glide symmetry in Equation (5.4) is parity-reversing, which induces a sign change in the Berry curvature.

³The symmetry is presented without unitary conjugation, but as noted in the supplement to Ref. [12], the presence of such a conjugation [as in Equation (5.1)] makes no difference topologically.

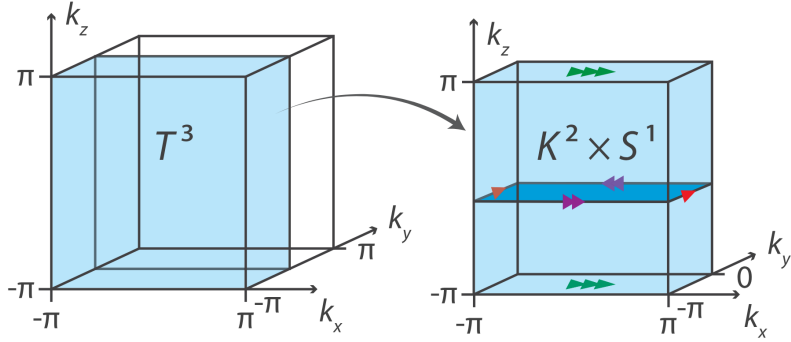


Figure 5.4: Figure adapted from Ref. [12]. The glide symmetry in Equation (5.4) acts on the Brillouin torus \mathbb{T}^3 in such a way that the fundamental domain (covering half the torus) is topologically $K^2 \times S^1$. Coloured arrows indicate the correct boundary identifications.

These chirality changes may result in a system in which the total chirality of Weyl points does not add to zero on the fundamental domain; that is, the Nielsen–Ninomiya charge cancellation theorem in Equation (4.7) is circumvented. In particular, two Weyl points with the same chirality may be connected by a Fermi arc on an xy -like surface, see Figure 5.5. It is demonstrated that a Fermi arc on such a surface connects

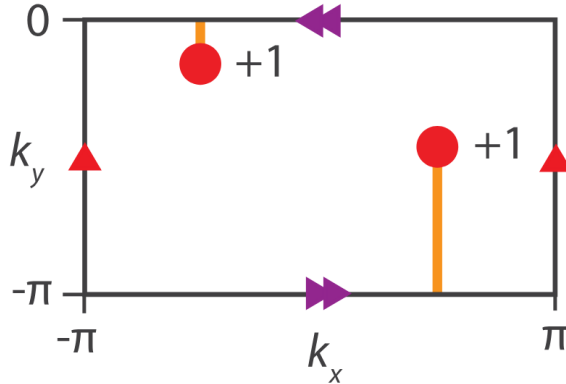


Figure 5.5: Figure from Ref. [12]. Surface Brillouin zone obtained from imposing open boundary conditions in the z direction. A Fermi arc is shown which connects (projections of) Weyl points of the same chirality. This Fermi arc crosses the orientation-reversing boundary at $k_y = 0$ once (i.e. an odd number of times).

two same-chirality Weyl points if and only if it lies on an “orientation-reversing path”, i.e. it crosses the line at $k_y = 0$ an odd number of times.

Moreover, a new charge cancellation theorem is derived from a \mathbb{Z}_2 invariant ν existing on gapped K^2 -like slices of constant k_z . This invariant is equivalent to that on the Klein bottle insulator in Ref. [59], and is calculated using Equations (5.2) and (5.3). It is shown that this invariant changes whenever such a slice is moved across a Weyl point of odd chirality in the k_z direction, see Figure 5.6. It is then argued that, since the fundamental domain is periodic in the k_z direction, there must be an even number of such changes in ν . This leads to a novel \mathbb{Z}_2 charge cancellation condition

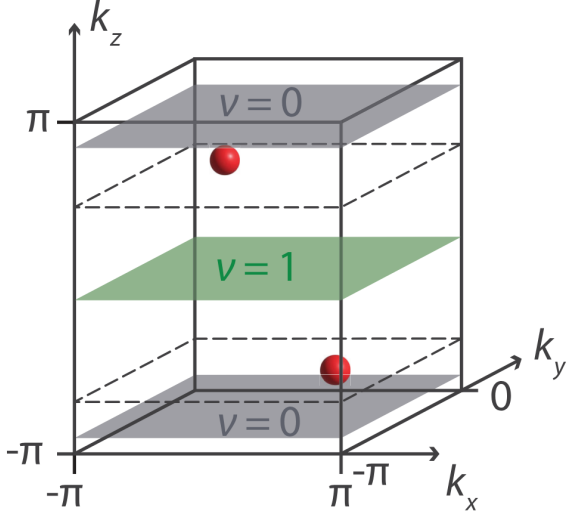


Figure 5.6: Figure from Ref. [12]. The $K^2 \times S^1$ fundamental domain is shown featuring two Weyl points, both with chirality +1. The invariant ν is shown to vary in the k_z direction, depending on the presence of Weyl points. Periodicity in the k_z direction then dictates that the total parity of the Weyl points must be even.

for Weyl points on $K^2 \times S^1$: if there are k Weyl points $w_i \in W$ in the fundamental domain, then their Chern numbers C_{w_i} must obey

$$\sum_{i=1}^k C_{w_i} = 0 \mod 2. \quad (5.5)$$

Finally, Ref. [12] includes an experimental realisation of a Weyl semimetal with momentum-space glide symmetry. The authors make use of one-dimensional photonic crystals, whose longitudinal coordinate z represents the z direction inside a three-dimensional semimetal. The optical properties of the unit cells of each crystal are parametrised by two periodic variables k_1 and k_2 , which effectively act as synthetic versions of the momenta k_x and k_y . These synthetic momenta are made to obey the glide symmetry in Equation (5.4), in such a way that the resulting system acts like a Weyl semimetal with two Weyl points of equal chirality in the fundamental domain. The optical crystals are then truncated in the z direction, so that surface states on the K^2 -like (k_x, k_y) surface may be probed at specific momenta. In this way, a Fermi arc is demonstrated which terminates in two points of similar chiralities; see Figure 5.7.

5.2 Topological exploration

The purpose of this section is to reframe and analyse the non-orientable Weyl semimetals described in Ref. [12] in terms of the algebraic topology language from Chapter 4. This approach has the advantage of being coordinate-free, and as such it provides a more fundamental understanding of the system's topological properties.

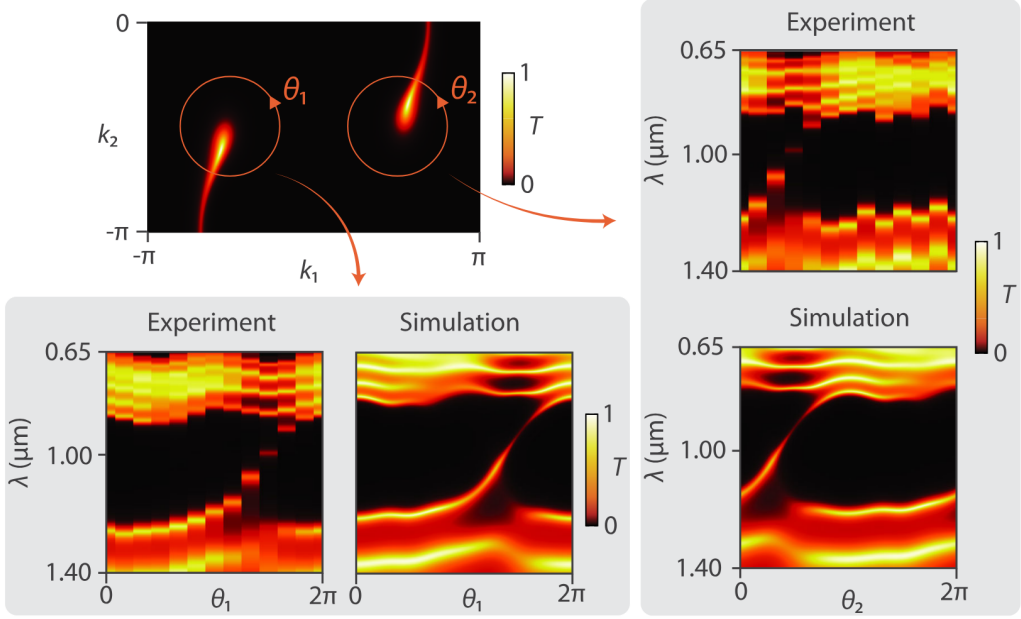


Figure 5.7: Figure from Ref. [12]. Top left: simulated K^2 surface Brillouin zone featuring a Fermi arc that crosses the orientation-reversing boundary at $k_2 = -\pi \sim 0$. Two circular contours are shown, parametrised by θ_1 and θ_2 . Bottom left: experimental (photonic) samples are prepared for several discrete values of θ_1 , with their synthetic momenta matched to the (k_1, k_2) corresponding to θ_1 . The plots show the frequency response (i.e. band structure) on the surface Brillouin zone as θ_1 runs from 0 to 2π . The rising dispersion indicates a positive chirality of the underlying Weyl point. Right: Similar samples are prepared for values of θ_2 . The dispersion is also ascending here, indicating a second positively charged Weyl node.

We obtain a direct description of how the Nielsen–Ninomiya theorem is modified into the \mathbb{Z}_2 charge cancellation condition in Equation (5.5). We also obtain a more complete picture of the different invariants associated with such a system, and are able to distinguish which are related to the topological insulator phase, and which relate to the introduction of Weyl nodes. To the knowledge of the author, the insights contained in this section are novel.

5.2.1 Preliminary clarifications

As a motivation for the proposed coordinate-free description, we begin by elucidating some minor points of confusion present in Ref. [12].

First of all, there is a relatively strong emphasis on the two “orientation-reversing planes” at $k_y = \pm\pi$ and $k_y = 0$. For example, it is stated that relative chirality can be defined unambiguously on fundamental domains that avoid these planes. This is true on a technical level, but it creates the impression that the orientation reversal occurs locally at the boundary of the fundamental domain, raising questions about the nature of Weyl points existing on these planes.

In reality, orientation reversal is a global feature. We are free to reparametrise the fundamental domain in a way that includes the planes $k_y = \pm\pi$ and $k_y = 0$, and the notion of relative chirality may change as a result; this is illustrated in Figure 5.8. For any given set of distinct Weyl points obeying the symmetry, it is possible in

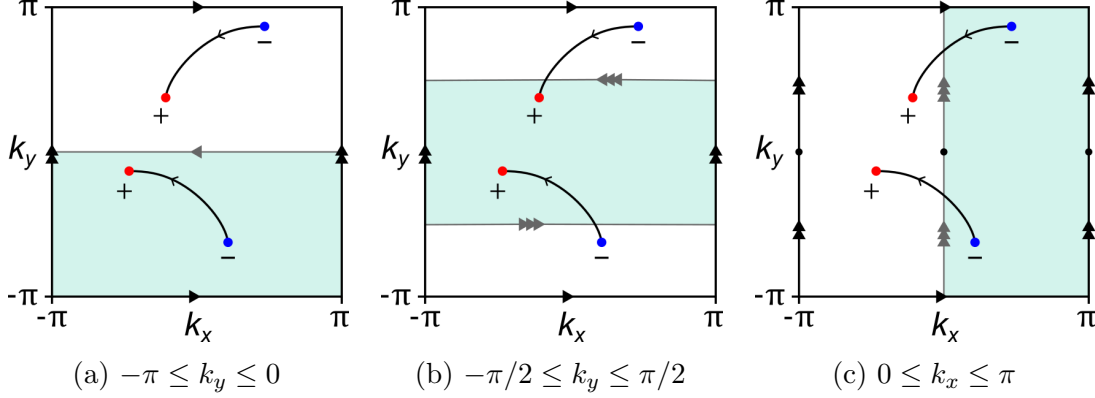


Figure 5.8: Top view of the 3D Brillouin torus (or 2D surface torus) for a given Weyl semimetal state obeying the glide symmetry in Equation (5.4), with Weyl points and oriented Dirac strings (Fermi arcs) drawn in. Different parametrisations of the fundamental domain are shaded in teal: (a) the domain outlined in Ref. [12]; (b) the same domain shifted in the k_y direction; (c) a domain spanning the k_y direction. Each of these domains is homeomorphic to $K^2 \times S^1$ (K^2) under the boundary identifications shown. Note that both the absolute and relative chirality of the two Weyl nodes in the fundamental domain change under these alternative parametrisations.

principle to achieve any relative chirality by reparametrising the fundamental domain. It should be noted that there do exist two planes that are of special significance, namely the so-called *glide planes* at $k_x = 0$ and $k_x = \pm\pi$; these planes are (taken as a whole) invariant under the symmetry, and as such they cannot be excluded completely from any given parametrisation.

A similar point of confusion arises in explaining how the usual relation between Nielsen–Ninomiya and the Poincaré–Hopf theorem for vector fields breaks down. On the regular Brillouin torus, the factor $\mathbf{h}(\mathbf{k})$ in the Bloch Hamiltonian can be considered a continuous vector field tangent to the torus. The Poincaré–Hopf theorem then tells us that the zeroes of such vector fields must have topological indices (corresponding to Weyl point chiralities) adding up to zero.

In the supplement to Ref. [12], the failure of Poincaré–Hopf is attributed to a discontinuity of the vector field at the planes $k_y = \pm\pi$ and $k_y = 0$; see Figure 5.9. However, this mischaracterises the situation somewhat; in reality, $\mathbf{h}(\mathbf{k})$ cannot be considered a well defined tangent vector field to $K^2 \times S^1$ to begin with. This is illustrated in Figure 5.10: two vectors which point away from each other in the fundamental domain may instead point towards each other after applying the glide symmetry. As such, \mathbf{h} should be thought of as a more abstract map $K^2 \times S^1 \rightarrow \mathbb{R}^3$ rather than a tangent vector field. To be precise, \mathbf{h} is a section of the trivial \mathbb{R}^3 -bundle

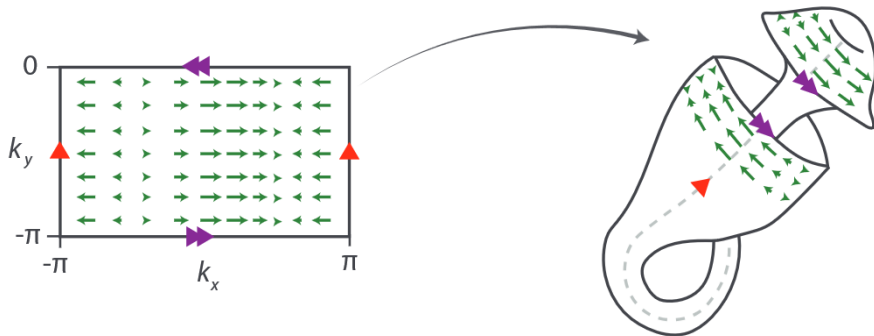


Figure 5.9: Figure from the supplement to Ref. [12]. The k_x component of an example $\mathbf{h}(\mathbf{k})$ is mapped onto a K^2 slice of the fundamental Brillouin zone and then “bent into shape” to demonstrate discontinuity.

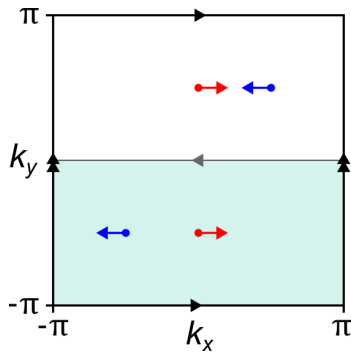


Figure 5.10: Example vectors $\mathbf{h}(\mathbf{k})$ on the glide symmetric Brillouin zone. Similar colours indicate that the vectors are related by glide symmetry.

over $K^2 \times S^1$, not of its tangent bundle.⁴ The resulting mod 2 charge cancellation is not necessarily a sign that Poincaré–Hopf has failed, but rather that we are operating outside its realm of applicability. In fact, instead of rendering the theorem broken in some way, it may be more constructive to reason the other way around. The argument goes as follows: Poincaré–Hopf usually holds because one can always locally induce a canonical orientation on the tangent bundle from an orientation on the manifold itself. However, in the case of a map $K^2 \times S^1 \rightarrow \mathbb{R}^3$, one has an orientable \mathbb{R}^3 -bundle over a non-orientable base manifold. This means that the orientation of the bundle becomes fundamentally disconnected from that of the manifold, and a relative orientation between the two must be chosen arbitrarily and—since the base manifold does not admit a global orientation—locally. The mod 2 charge cancellation then tells us how Poincaré–Hopf needs to be modified to accommodate this arbitrary orientation: in some sense it gives rise to a “generalised” or “modified” Poincaré–Hopf theorem. Note that choosing between different fundamental domains on the torus (in the way outlined in Figure 5.8) is precisely a way of inducing such a relative orientation between $K^2 \times S^1$ and its \mathbb{R}^3 -bundle; we will see this idea play out in more detail once we derive the mod 2 charge cancellation from more fundamental

⁴In the usual case of the torus, these descriptions are equivalent: \mathbb{T}^3 is parallelisable, i.e. $T\mathbb{T}^3 \cong \mathbb{T}^3 \times \mathbb{R}^3$. This is what allows Poincaré–Hopf to apply naturally.

cohomology arguments.

It is worth emphasizing that this modification of Poincaré–Hopf is a general feature of non-orientable manifolds, not one that is specific to the model Hamiltonian. Smooth tangent vector fields can in fact be defined on $K^2 \times S^1$, but a Hamiltonian cannot be associated to them in a canonical way. Such a construction usually requires using gamma matrices that “twist along” with the tangent bundle of the manifold instead of the regular vector of Pauli matrices, but these gamma matrices cannot be defined consistently on a non-orientable manifold.⁵ As a result, the notion of a tangent vector field loses some of its utility in studying the topological properties of a non-orientable system. Instead, any topological analysis must be performed in terms of more fundamental algebraic topology tools, such as the homology and cohomology relied on in this work.

A final point that merits clarification is the inclusion of a second glide symmetry. The supplement to Ref. [12] discusses imposing Equation (5.4) together with a similar symmetry along the glide plane $k_y = 0$:

$$H(k_x, k_y, k_z) = H(k_x + \pi, -k_y, k_z). \quad (5.6)$$

It is claimed that this double symmetry subdivides the 3-torus into four copies of a different non-orientable manifold $\mathbb{R}P^2 \times S^1$. Here $\mathbb{R}P^2$ is the real projective plane, i.e. the space of all lines through the origin in \mathbb{R}^3 ; it can be obtained by identifying all antipodal points on a 2-sphere. In this case, $\mathbb{R}P^2 \times S^1$ is obtained by imposing anti-periodic boundary conditions in both the k_x and k_y directions on a quarter of the Brillouin zone. However, this direct identification with $\mathbb{R}P^2 \times S^1$ cannot be made as straightforwardly as in the case of a single glide symmetry. As discussed in our review of Refs. [62] and [63], the combination of two perpendicular glide symmetries in two dimensions does not have a free action, leading to the fixed points shown in Figure 5.3.

The situation is analogous in three dimensions: the four lines at the momenta $\mathbf{k} = (\pm\pi/2, \pm\pi/2, k_z)$ are fixed under application of both glide symmetries at once. As a result, a Weyl point existing on one of these lines must have an even chirality, and it only has one symmetric partner in the 3-torus rather than the three one would expect from four identical copies of $\mathbb{R}P^2 \times S^1$.⁶ Such Weyl points are physically fine-tuned and are expected to split into pairs under perturbations. Nevertheless, additional symmetries may exist which force Weyl points to exist on these lines, in which case the exceptional behaviour becomes key to the description. Moreover, the reduction to a fundamental domain is predicated on a free group action in the main

⁵The proper construction is that of a Clifford algebra bundle over the tangent bundle, see Section 4.2 of Ref. [32]. This construction relies on the existence of a so-called *spin^c structure* (essentially a basis of spinors) on the base manifold, but non-orientable manifolds do not admit such a structure on their tangent bundle.

⁶One can also argue that this must be the case topologically: if a manifold M has an n -sheeted cover \tilde{M} , then the Euler characteristics of both spaces must be related by $\chi(\tilde{M}) = n\chi(M)$. Reducing the system down to two dimensions, we find $\chi(\mathbb{T}^2) = 0$ and $\chi(\mathbb{R}P^2) = 1$, so that the former cannot cover the latter. Instead, the only possible covering space for $\mathbb{R}P^2$ is the double cover $S^2 \rightarrow \mathbb{R}P^2$, since $\chi(S^2) = 2$. Technically speaking, this means the fundamental domain needs to be described as an *orbifold* rather than a manifold, i.e. a space that encodes data about orbits of a group action. For example, the Euler characteristic of $\mathbb{R}P^2$ is zero as an orbifold.

text of Ref. [12]. As such, analysis of a purely $\mathbb{R}P^2 \times S^1$ Brillouin zone cannot a priori be expected to provide the correct topological classification for this double glide symmetry. Indeed, similar to the case of time reversal in Section 4.2.4, a proper classification scheme should involve equivariant cohomology on the torus, bearing in mind the topological role of the high-symmetry points. This becomes manifestly clear from the existence of a topological invariant at these high-symmetry points [62, 63]. This full analysis is somewhat beyond the scope of the present text, and in what follows we will restrict our attention to the case of a single glide symmetry.

5.2.2 Classification scheme

There are two main conceptual challenges that present themselves in attempting to apply consistent cohomology and homology frameworks to non-orientable systems, and in particular in developing a physical intuition for them. First of all, the analogy between second cohomology classes and differential two-forms such as the Berry curvature \mathcal{F} breaks down in this case, and a statement like Equation (4.4) can no longer be taken to hold directly. This is because differential forms like \mathcal{F} cannot be integrated over non-orientable manifolds, and the associated (de Rham) cohomology group is actually real-valued—as discussed in Section 2.2.2, it cannot readily encode the \mathbb{Z}_2 invariants induced by changes in orientation. As an example, suppose we are trying to find an invariant for the 2D Klein bottle insulator obeying Equation (5.1). Integrating a Berry curvature on K^2 directly is not well defined, while integrating over the entire Brillouin torus always yields zero: the integration is over two oppositely oriented areas. The correct \mathbb{Z}_2 invariant can be interpreted as integration with different signs on both halves of the torus, bearing in mind that the result is only gauge invariant mod 2. In order to capture this behaviour generally, we need to move to the richer but more abstract integer-valued cohomology laid out in Section 2.2.

The second obstacle is that Poincaré duality is altered in this context. In Section 4.2, this form of duality was used to identify the familiar cohomology invariants with homology invariants, in the form of non-trivial oriented loops and Dirac strings. In a non-orientable system, this identification cannot be made directly; in this case, either the homology or the cohomology must be *twisted* by the introduction of a *local coefficient system* $\tilde{\mathbb{Z}}$ [1, 65]. Such a coefficient system compensates for the twist in orientation by tracking sign changes across the manifold. Introducing local coefficients on an n -manifold M gives rise to the twisted homology and cohomology groups $H_k(M; \tilde{\mathbb{Z}})$ and $H^k(M; \tilde{\mathbb{Z}})$. Poincaré duality then takes the following forms [1, Theorem 3H.6]:

$$\begin{aligned} H_k(M; \tilde{\mathbb{Z}}) &\cong H^{n-k}(M), \\ H^k(M; \tilde{\mathbb{Z}}) &\cong H_{n-k}(M). \end{aligned}$$

That is, twisting either one of the homology or cohomology restores Poincaré duality; if the homology is twisted, ordinary cohomology must be used and vice versa. When M is orientable, the local coefficients become trivial and the original form of Poincaré duality is recovered from both relations.

Given the fact that Poincaré duality can be restored by twisting either the homology or the cohomology group, the correct classification of a non-orientable

physical system hinges on this choice of twist. Fortunately, there is a straightforward way to decide between the two in the case of a Weyl semimetal with an orientation-reversing \mathbb{Z}_2 symmetry. In this situation, Poincaré duality is necessary in order to relate the chirality of Weyl points (which are cohomology invariants) to the orientation of their corresponding Dirac strings (which are the dual homology invariants). Under the orientation-reversing symmetry, Poincaré duality breaking manifests itself in the fact that the Weyl point chiralities are naturally reversed, while the orientation of Dirac strings is unchanged. This is illustrated schematically in Figure 5.11. The

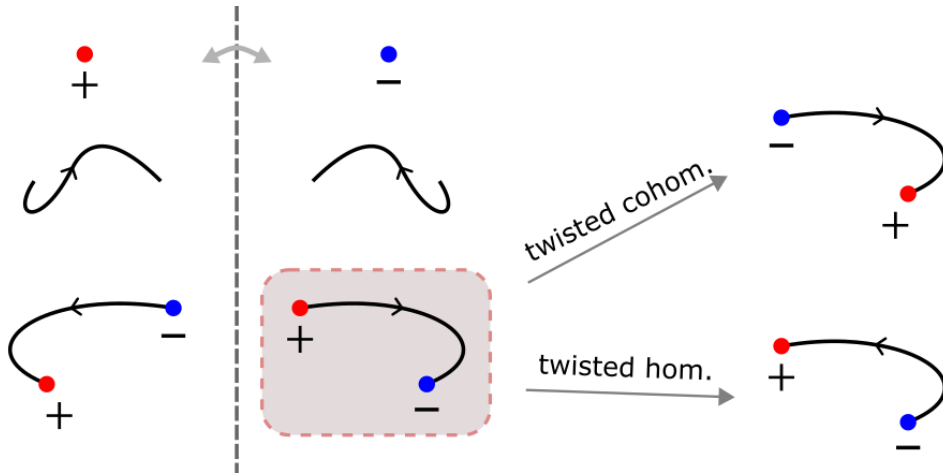


Figure 5.11: On the top left, the action of an orientation-reversing symmetry (represented by the dashed mirror axis) is shown on a Weyl point [of which the chirality is an invariant in $H^2(M \setminus W)$] and a Dirac string [representing an invariant in $H_1(M, W)$]. The Weyl point has its chirality reversed, since the Chern number is a pseudoscalar. On the other hand, the Dirac string is mirrored but maintains its internal orientation (i.e. its image is also oriented away from the “hook” at the end). As a result, when the symmetry acts on a set of two Weyl points connected by a Dirac string, the resulting structure has a Dirac string of which the orientation is inconsistent with the chirality of the Weyl points (shown in the shaded area)—this is a result of Poincaré duality breaking. This problem can be resolved in one of two ways: either the cohomology is twisted into $H^2(M \setminus W; \tilde{\mathbb{Z}})$ to undo the chirality reversal, or the homology is twisted into $H_1(M, W; \tilde{\mathbb{Z}})$ to reverse the Dirac string’s orientation. Poincaré duality is restored in both cases; the correct approach depends on the physical setup.

decision of which group must be twisted can thus be made by noting how the chirality of Weyl points (outside of high-symmetry points) relates to that of their symmetric partners in the full Brillouin torus. To be precise, the presence of same-chirality pairs indicates that the (cohomological) Chern number is not reversed as expected, and the cohomology must be twisted. Meanwhile, pairs with opposite chiralities indicate that the cohomology behaves naturally, and the homology (i.e. the Dirac string orientations) must be twisted to follow suit.

[The next few paragraphs are subject to change, the maths don't quite work out

– e.g. the sign of T^2 appears to be relevant as well. Their contents do not influence the logic in the later paragraphs in any significant way.] Physically, this twisting of the homology may be related to the unitarity or anti-unitarity of the symmetry operation. This can be seen as follows: in the case of a unitary symmetry relating $\mathbf{k} \leftrightarrow \mathbf{k}'$, the Hamiltonian obeys

$$U\mathcal{H}(\mathbf{k})U^\dagger = \mathcal{H}(\mathbf{k}').$$

If $|\psi(\mathbf{k})\rangle$ is an eigenstate of $\mathcal{H}(\mathbf{k})$, it follows that $|\psi(\mathbf{k}')\rangle := U|\psi(\mathbf{k})\rangle$ is an eigenstate of $\mathcal{H}(\mathbf{k}')$, and so the Berry connection transforms as

$$\begin{aligned}\mathcal{A}(\mathbf{k}) &= i\langle\psi(\mathbf{k})|\partial_{\mathbf{k}}\psi(\mathbf{k})\rangle \cdot d\mathbf{k} \\ &= i\langle\psi(\mathbf{k}')|UU^\dagger|\partial_{\mathbf{k}}\psi(\mathbf{k}')\rangle \cdot d\mathbf{k} \\ &= i\langle\psi(\mathbf{k}')|\partial_{\mathbf{k}'}\psi(\mathbf{k}')\rangle \cdot d\mathbf{k}' \quad \Big) \quad UU^\dagger = 1, \quad \partial_{\mathbf{k}}f \cdot d\mathbf{k} = \partial_{\mathbf{k}'}f \cdot d\mathbf{k}' \\ &= \mathcal{A}(\mathbf{k}').\end{aligned}$$

Since the Berry connection one-form is left invariant, so is the Berry curvature two-form. A final minus sign is then induced by the change of orientation when integrating this two-form, so that the Chern number (Weyl point chirality) changes sign under unitary orientation-reversing symmetries. This is exactly what is implied when the Chern number is called a pseudoscalar. Looking back at Figure 5.11, twisted homology (and its dual ordinary cohomology) must be used to obtain the correct invariants.

On the other hand, under an anti-unitary symmetry the Hamiltonian transforms as [for $T^2 = -1$]

$$U\mathcal{H}(\mathbf{k})U^\dagger = \mathcal{H}^*(\mathbf{k}'),$$

and its eigenstates obey $\langle\psi(\mathbf{k}')| = U|\psi(\mathbf{k})\rangle$. The unitary matrix U drops out of the Berry connection as before, and we are left with

$$\begin{aligned}\mathcal{A}(\mathbf{k}) &= i\langle\psi(\mathbf{k})|\partial_{\mathbf{k}}\psi(\mathbf{k})\rangle \cdot d\mathbf{k} \\ &= i\langle\partial_{\mathbf{k}'}\psi(\mathbf{k}')|\psi(\mathbf{k}')\rangle \cdot d\mathbf{k}' \\ &= -(i\langle\psi(\mathbf{k}')|\partial_{\mathbf{k}'}\psi(\mathbf{k}')\rangle)^* \cdot d\mathbf{k}' \\ &= -\mathcal{A}^*(\mathbf{k}') = -\mathcal{A}(\mathbf{k}),\end{aligned}$$

where the last equality holds because \mathcal{A} is a real-valued one-form. It follows that the Berry curvature and its associated Chern numbers pick up an additional minus sign, which cancels out the orientation reversal. As a result, Weyl points have the same sign as their symmetric partners, and the correct description is given by twisted cohomology and ordinary homology.

As an example, we may apply this line of reasoning to the time reversal invariant Weyl semimetal from Section 4.2.4. This system is not usually thought of in terms of non-orientability, but the time reversal symmetry acts in an orientation-reversing way: an odd number (i.e. all three) of momentum directions are inverted, leading to a change of parity. Figure 5.12(a) illustrates that the effective Brillouin zone is indeed non-orientable. As discussed before, **the time-reversal symmetry in this system is anti-unitary, and as such the Kramers pairs of Weyl points at opposite**

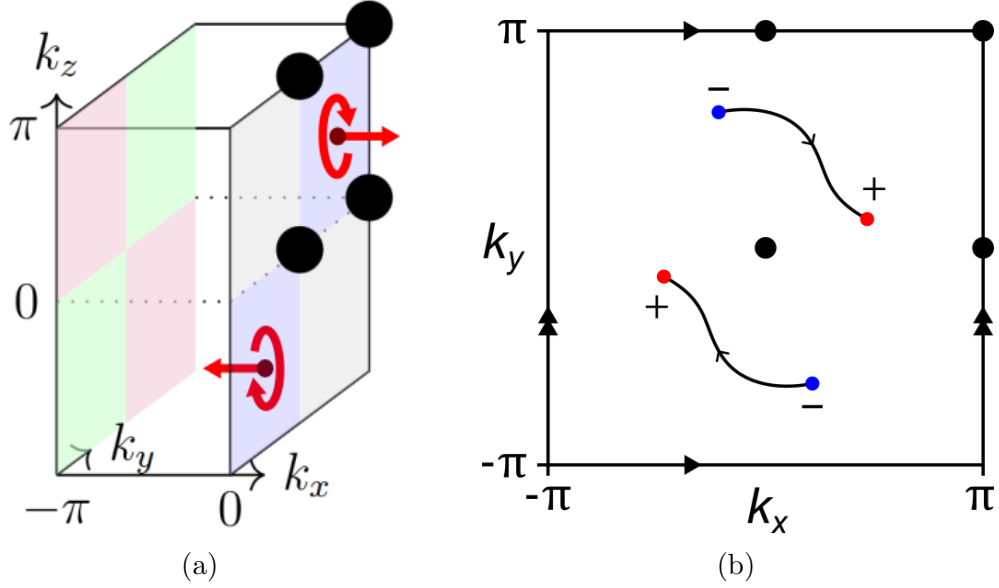


Figure 5.12: (a) Figure adapted from Ref. [36]. The effective Brillouin zone under time reversal symmetry is half of \mathbb{T}^3 , with additional identifications of the coloured areas as $k \sim -k$. The resulting space is non-orientable: a “test particle” with a given helicity is shown travelling out through the boundary at $\mathbf{k} = (0, \pi/2, \pi/2)^T$, and reappearing at $\mathbf{k} = (0, -\pi/2, -\pi/2)^T$ with the opposite helicity. (b) Top view of a time reversal invariant Weyl semimetal, featuring same-chirality Kramers pairs at conjugate momenta, indicating a twist in the cohomology. On the other hand, the orientation of Dirac strings respects the symmetry, indicating ordinary (“untwisted”) homology.

momenta (related by $\mathbf{k} \leftrightarrow -\mathbf{k}$) always have the same chirality; see Figure 5.12(b). Again, these same-chirality pairs are an indication that the Chern numbers of Weyl points do not transform as expected, and so the cohomology must be twisted. It follows that the homology should not be twisted; this can also be seen directly from the Dirac strings in Figure 5.12(b), whose orientation is directly related by the symmetry (i.e. the arrows run in relative directions respecting $\mathbf{k} \leftrightarrow -\mathbf{k}$). This description in terms of twisted cohomology and ordinary homology agrees exactly with the one given in Section 4.2.4, which was derived from more abstract vector bundle classification arguments in Ref. [36]. In this particular case, direct calculation of the (co)homology groups on the effective Brillouin zone is complicated by the existence of high-symmetry points (i.e. the action of the symmetry is not free), which is why the authors of Ref. [36] use equivariant (co)homology on the full torus.

Returning to the case of a momentum-space glide symmetry, we can see from Figure 5.8(a) that the situation is different here. **The unitary nature of the symmetry means that** every Weyl point in the fundamental domain is related by symmetry to an oppositely charged point in the other half of the torus, while the orientation of Dirac strings is reversed under the symmetry. It follows that the classification of topological phases should rely on twisted *homology*, and equivalently, ordinary cohomology. Since there is a proper fundamental domain in this case, there is no need

to compute equivariant (co)homology groups, and we may instead rely on ordinary cohomology and twisted homology on $K^2 \times S^1$.⁷

The choice of ordinary cohomology can be corroborated in two important ways. Firstly, the use of ordinary second cohomology classes indicates that we are classifying complex line bundles over the fundamental domain. An important insight from K-theory tells us that this is equivalent to classifying equivariant line bundles over the full torus [67, Proposition 2.1].⁸ That is, we are classifying states that respect the symmetry directly. Secondly, the \mathbb{Z}_2 invariant found in Ref. [12] on K^2 -like slices of constant k_z is recovered using ordinary cohomology, related to the fact that $H^2(K^2) \cong \mathbb{Z}_2$. Twisted cohomology would give a $H^2(K^2; \mathbb{Z}) \cong \mathbb{Z}$ invariant on these slices.

All in all, we find that the correct classification of semimetal phases in this system is given by the following Mayer–Vietoris exact sequence of cohomology groups on $M := K^2 \times S^1$:

$$0 \rightarrow \underbrace{H^2(M)}_{\text{Insulator}} \rightarrow \underbrace{H^2(M \setminus W)}_{\text{Semimetal}} \rightarrow \bigoplus_{w \in W} H^2(S_w^2) \xrightarrow{\Sigma} H^3(M) \rightarrow 0, \quad (5.7)$$

where as before, W is the set of Weyl points on M and S_w^2 is a small 2-sphere surrounding the Weyl point $w \in W$. Equivalently, the classification may be given in terms of the following dual *twisted* homology sequence:

$$0 \rightarrow \underbrace{H_1(M; \widetilde{\mathbb{Z}})}_{\text{Twisted Dirac loops}} \rightarrow \underbrace{H_1(M, W; \widetilde{\mathbb{Z}})}_{\text{Twisted Dirac strings}} \xrightarrow{\partial} H_0(W; \widetilde{\mathbb{Z}}) \xrightarrow{\Sigma} H_0(M; \widetilde{\mathbb{Z}}) \rightarrow 0, \quad (5.8)$$

where we refer to the Dirac loops and Dirac strings as twisted to emphasise the non-trivial action of the symmetry on their orientation. The concept of a twisted Dirac string on $K^2 \times S^1$ can be difficult to intuit, leading to Dirac strings that appear to change orientation at orientation-reversing boundaries of the fundamental domain in a setup like Figure 5.8(c). As such, they are more readily understood as equivariant (i.e. symmetry-related) pairs of Dirac strings on the full torus \mathbb{T}^3 , of which the orientation is reversed under the symmetry.

In what follows, we will provide explicit computations of these sequences and discuss the associated invariants.

5.2.3 Computation of invariants on $K^2 \times S^1$

The use of ordinary cohomology groups in the Mayer–Vietoris sequence (5.7) means that calculations are relatively straightforward, and standard techniques such as cellular cohomology can be applied. [Given enough time, I can include a small Appendix B containing an example cellular cohomology calculation.] Using these methods, we calculate the sequence to be

$$0 \rightarrow \mathbb{Z} \oplus \mathbb{Z}_2 \xrightarrow{\alpha} \mathbb{Z} \oplus \mathbb{Z}_2 \oplus \mathbb{Z}^k \xrightarrow{\beta} \mathbb{Z}^k \xrightarrow{\Sigma} \mathbb{Z}_2 \rightarrow 0, \quad (5.9)$$

⁷ Formally speaking, equivariant cohomology of a space M with a free action of the group G is equivalent to ordinary cohomology on the quotient space M/G [66, Corollary 9.6].

⁸This is related to footnote 7 in the sense that K-theory is a *generalised cohomology* theory.

where $k = |W|$ is the number of Weyl points. Given that the twisted homology sequence (5.8) is related to the Mayer–Vietoris sequence by Poincaré duality, it features the exact same groups in the same order; the difference is only in the interpretation.

For comparison, we recall here the semimetal Mayer–Vietoris sequence on \mathbb{T}^3 from Section 4.2.3:

$$0 \rightarrow \mathbb{Z}^3 \rightarrow \mathbb{Z}^3 \oplus \mathbb{Z}^{k-1} \xrightarrow{\beta} \mathbb{Z}^k \xrightarrow{\Sigma} \mathbb{Z} \rightarrow 0. \quad (5.10)$$

Some relevant differences between these two sequences are highlighted below.

Insulating phases

The first difference between the Mayer–Vietoris sequences on \mathbb{T}^3 and $K^2 \times S^1$ lies in the insulating topology of the system, in the absence of any Weyl points. Whereas the 3D Chern insulator on the plain torus features a Chern vector in $H^2(\mathbb{T}^3) \cong \mathbb{Z}^3$, this group is reduced to $H^2(K^2 \times S^1) \cong \mathbb{Z} \oplus \mathbb{Z}_2$ under the action of the glide symmetry. As a result, the $K^2 \times S^1$ insulator is not classified by three Chern numbers $C_{x,y,z} \in \mathbb{Z}$, but by a \mathbb{Z} invariant ν_x and a \mathbb{Z}_2 invariant ν_z —the reasoning behind our choice of symbols will become apparent shortly.

The reduction to two invariants can be most readily understood from the twisted homology point of view. On \mathbb{T}^3 , the three generators of $H_1(\mathbb{T}^3) \cong \mathbb{Z}^3$ are represented by oriented Dirac loops $\ell_{x,y,z}$ that wind around the 3-torus once in each respective coordinate direction. Under glide symmetry, each of these loops obtains a symmetric partner $\ell'_{x,y,z}$ with a reversed internal orientation—this is due to the twist in the homology. Taken together with the original loop, $\ell_{x,y,z} + \ell'_{x,y,z}$ is equivalent to a twisted Dirac loop $\tilde{\ell}_{x,y,z}$ on $K^2 \times S^1$, representing an invariant in $H_1(K^2 \times S^1; \widetilde{\mathbb{Z}})$. The reduction to $\mathbb{Z} \oplus \mathbb{Z}_2$ is then caused by specific degeneracies in these twisted Dirac strings: $\tilde{\ell}_x$ generates the full \mathbb{Z} invariant ν_x , $\tilde{\ell}_y$ turns out to be trivial, and $\tilde{\ell}_z$ generates the \mathbb{Z}_2 invariant ν_z . This is illustrated in more detail in Figure 5.13.

The invariant $\nu_z \in \mathbb{Z}_2$ corresponds precisely to the \mathbb{Z}_2 invariant on K^2 slices described in Ref. [12], and stems from the 2D Klein bottle insulator in Ref. [59]. It may be calculated on any K^2 slice using Equations (5.2) and (5.3).

The \mathbb{Z} invariant ν_x appears to be novel; as discussed under Figure 5.13(a), it manifests as an even Chern number $C_x = 2\nu_x \in 2\mathbb{Z}$ on the full Brillouin torus, relating to the fact that the torus contains two copies of $K^2 \times S^1$. This suggests one way of calculating this invariant in practice: it may be obtained from \mathbb{T}^3 as

$$\nu_x = \frac{1}{2}C_x = \frac{1}{4\pi} \int_{\mathbb{T}_{yz}^2} \mathcal{F}, \quad (5.11)$$

where \mathbb{T}_{yz}^2 is any slice of \mathbb{T}^3 running in the yz -direction. This calculation does not generally respect the glide symmetry, since such a \mathbb{T}_{yz}^2 is not invariant outside of the glide planes at $k_x = 0$ and $k_x = \pm\pi$. Still, it results in the correct invariant in the insulating case: by regular Poincaré duality on the full torus, the integral over \mathbb{T}_{yz}^2 counts the number of ℓ_x -like Dirac loops, and the generator $\tilde{\ell}_x$ features precisely two

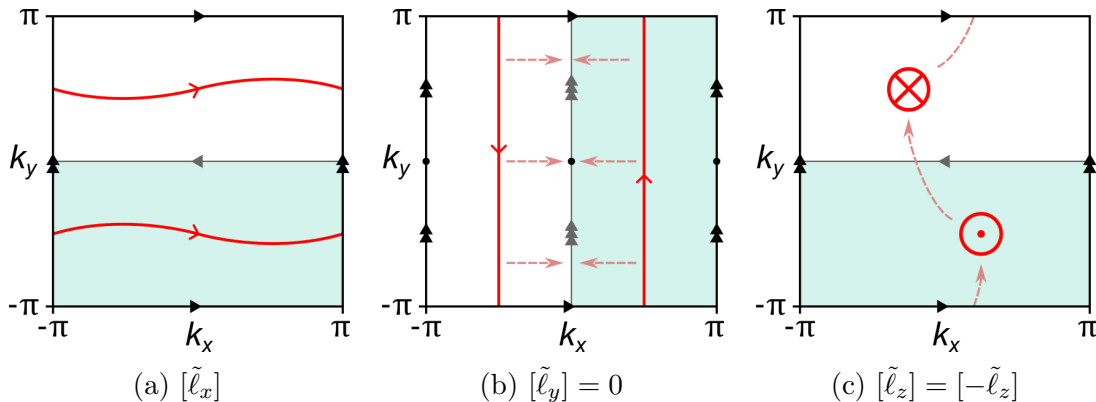


Figure 5.13: Top view of \mathbb{T}^3 . Each graphic shows one of the three basic Dirac loops $\ell_{x,y,z}$ [representing the generators of $H_1(\mathbb{T}^3)$] sitting inside a fundamental domain (shaded teal). Each loop is doubled by the action of the symmetry, into what can be considered a twisted Dirac loop $\tilde{\ell}_{x,y,z}$ [representing an invariant in $H_1(K^2 \times S^1; \widetilde{\mathbb{Z}})$] shown in red. (a) In the case of ℓ_x , the orientation reversal cancels out the $k_x \mapsto -k_x$ parity change from the glide symmetry, and the resulting twisted Dirac string $\tilde{\ell}_x$ has a consistent orientation. It follows that the associated invariant $\nu_x \in \mathbb{Z}$ induces an even Chern number $C_x = 2\nu_x \in 2\mathbb{Z}$ on the full torus. (b) The alternative fundamental domain from Figure 5.8(c) paints a clearer picture for ℓ_y . The loop is mirrored along the glide plane $k_x = 0$ and has its orientation reversed. The resulting twisted Dirac string $\tilde{\ell}_y$ is trivial: as indicated by the dashed arrows, the two copies can be moved together while maintaining glide symmetry, and they cancel out when they meet on the glide plane. As a result, there is no invariant ν_y . (c) The Dirac loop ℓ_z running in the positive z direction (“out of the page”) in the fundamental domain is doubled to a second loop running in the negative z direction (“into the page”). In this case, the two loops cannot be brought together while respecting the symmetry, but they can be interchanged by moving them along the dashed arrows. It follows that the resulting twisted Dirac string $\tilde{\ell}_z$ is equivalent to its own inverse $-\tilde{\ell}_z$, meaning it generates a \mathbb{Z}_2 invariant ν_z .

such loops on the torus.⁹ We will return to the case with Weyl points when we study the full group of semimetal invariants.

Mod 2 charge cancellation

A second feature that stands out is the appearance of a \mathbb{Z}_2 group on the far right side of the exact sequence in Equation (5.9). It is worth mentioning that this is a general feature of ordinary cohomology on non-orientable manifolds: the rightmost group is the top cohomology group of the Brillouin zone, and any non-orientable

⁹A Dirac loop may in principle also contain y and z components, but these do not affect this integral. From a homology perspective, such loops may be decomposed into their basic $\ell_{x,y,z}$ components because the first homology group is Abelian.

n -manifold M has $H^n(M) \cong \mathbb{Z}_2$.

Recall from Section 4.2.3 that the map Σ in Equation (5.10) can be interpreted as a sum over all Weyl point charges on \mathbb{T}^3 . The Nielsen–Ninomiya charge cancellation theorem on the torus then arises from the fact that $\Sigma \circ \beta = 0$; that is, a semimetal structure $a \in \mathbb{Z}^3 \oplus \mathbb{Z}^{k-1}$ must always feature a charge configuration $\beta(a) \in \mathbb{Z}^k$ such that the charges sum to $\Sigma(\beta(a)) = 0 \in \mathbb{Z}$.

The situation is somewhat more subtle on $K^2 \times S^1$: the \mathbb{Z}^k group $H^2\left(\bigcup_{i=1}^k S_{w_i}^2\right)$ and its dual $H_0(W; \tilde{\mathbb{Z}})$ no longer have a direct interpretation in terms of Weyl point charges, since both the absolute and relative chiralities of these points are ill defined (see Figure 5.8). That is, the spheres S_{w_i} no longer have a canonical orientation descending from the ambient manifold.¹⁰ Instead, $H^2\left(\bigcup_{i=1}^k S_{w_i}^2\right)$ must be interpreted as the group of charges χ_i given a choice of orientation at each Weyl point w_i . This choice of orientation is exactly what is induced by choosing a specific fundamental domain: the changes of (absolute and relative) chirality in Figure 5.8 correspond to a change of basis of this \mathbb{Z}^k . Nevertheless, the map Σ can still be interpreted as a sum over these charges, precisely because it maps into \mathbb{Z}_2 :¹¹ to be exact, the map

$$\Sigma : \mathbb{Z}^k \rightarrow \mathbb{Z}_2, \quad (\chi_1, \dots, \chi_k) \mapsto \sum_{i=1}^k \chi_i \mod 2 \quad (5.12)$$

is invariant under change of orientation at each w_i because

$$\chi_i \equiv -\chi_i \mod 2.$$

It follows that the tail end of the sequence (5.9) can be interpreted unambiguously in terms of \mathbb{Z}_2 charge cancellation: regardless of the parametrisation of the fundamental domain, the charges belonging to a semimetal (i.e. mapped into \mathbb{Z}^k by β) must sum to $0 \in \mathbb{Z}_2$. This is the same charge cancellation condition presented in Equation (5.5).

Importantly, the exactness of Equation (5.9) also implies the converse statement by $\text{im}(\beta) = \ker(\Sigma)$: for a given set of Weyl points $W \subset K^2 \times S^1$, any configuration of charges with an even total [i.e. an element of $\ker(\Sigma)$] must be realised in some set of semimetal invariants [i.e. be an element of $\text{im}(\beta)$]. In the homology picture, this means there must exist configurations of twisted Dirac strings in $H_1(M, W; \tilde{\mathbb{Z}})$ realising any given set of charges adding to $0 \in \mathbb{Z}_2$.

One must be careful in interpreting this mod 2 charge cancellation in terms of a potentially non-zero total chirality. The \mathbb{Z}_2 group in the Mayer–Vietoris sequence tells us that total charge is fundamentally a \mathbb{Z}_2 invariant, and the semimetal topology fixes it to zero. Given any particular parametrisation of the fundamental domain, there may appear to be a net non-zero chirality on the Brillouin zone $K^2 \times S^1$, but this is not a topological invariant: for example, in Figure 5.8, the net chirality of a single topological state may be found to be 0, 2 or -2 depending on the parametrisation. In

¹⁰This is closely related to our observation in Section 5.2.1 that Poincaré–Hopf fails to apply because the trivial \mathbb{R}^3 -bundle over $K^2 \times S^1$ does not have a canonical orientation with respect to its base manifold.

¹¹Indeed, the group $H^3(K^2 \times S^1) \cong \mathbb{Z}_2$ is closely linked to the orientation of $K^2 \times S^1$; in technical terms, we say that $K^2 \times S^1$ is \mathbb{Z}_2 -orientable but not \mathbb{Z} -orientable [1, §3.3].

other words, the total chirality is ill defined as an integer in \mathbb{Z} , while the *parity* of the total charge is well defined and topologically invariant.

The appearance of non-zero total chirality is in close analogy to the concept of ghost fields in quantum field theory. There, apparent quantum fields may arise when fixing unphysical local gauge degrees of freedom. These ghost fields can usually be removed by a suitable change of gauge, and in any case they never appear in external physical observables. Similarly, the choice of orientation for a Weyl point on $K^2 \times S^1$ is an unphysical local degree of freedom, and one can usually choose these orientations (i.e. fix a fundamental domain) in a way that results in a total chirality of zero. In particular, this implies that one cannot readily assign physical meaning (e.g. in terms of an uncancelled chiral anomaly) to the net chirality appearing in a certain fundamental domain.

This can also be understood in field theory terms: as discussed in Section 5.2.1, a Hamiltonian cannot be defined on $K^2 \times S^1$ in terms of the tangent vector field, since it lacks a spinor basis (i.e. choice of gamma/Pauli matrices). Instead, any effective field theory on $K^2 \times S^1$ must rely on a choice of coordinates, and will not be invariant under change of coordinates in general. In such a theory, a net chiral anomaly will not generally represent a physically observable phenomenon. In other words, while the Nielsen–Ninomiya theorem is altered mathematically on $K^2 \times S^1$, its core physical implications of chiral anomaly cancellation cannot necessarily be circumvented. In this respect, the description in terms of the full Brillouin torus \mathbb{T}^3 with a glide symmetry may be more useful phenomenologically, where Nielsen–Ninomiya is more straightforwardly preserved and each Weyl point has a canonical orientation.

Semimetal invariants

Finally, central to the sequence in Equation (5.9) is the group of semimetal invariants,

$$H^2(K^2 \times S^1 \setminus W) \cong H_1(K^2 \times S^1, W; \widetilde{\mathbb{Z}}) \cong \mathbb{Z} \oplus \mathbb{Z}_2 \oplus \mathbb{Z}^k. \quad (5.13)$$

Much like the $\mathbb{Z}^3 \oplus \mathbb{Z}^{k-1}$ in the case of \mathbb{T}^3 , this group does not admit a canonical basis of invariants. Rather, the exactness of Equation (5.9) around this group provides information about the structure of the different semimetallic phases. The argument is similar to that at the end of Section 4.2.3: given a charge configuration c in the image of the map β (i.e. any c with an even total charge), the pre-image must obey

$$\beta^{-1}(c) \cong \beta^{-1}(0) =: \ker(\beta),$$

since β is a homomorphism. By exactness, we have $\ker(\beta) \cong \text{im}(\alpha) \cong \mathbb{Z} \oplus \mathbb{Z}_2$. That is, for each $c \in \text{im}(\beta)$ there are $\mathbb{Z} \oplus \mathbb{Z}_2$ worth of semimetal invariants (or equivalently, twisted Dirac string configurations) in its pre-image, differing from each other by the bulk invariants $\nu_x \in \mathbb{Z}$ and $\nu_z \in \mathbb{Z}_2$.

There is a subtle difference from the argument on the torus: on \mathbb{T}^3 , \mathbb{Z} charge cancellation ensures that the valid charge configurations exist in

$$\text{im}(\beta) = \ker(\Sigma) = \bigoplus_{w \in W} H^2(S_w^2) / H^3(\mathbb{T}^3) \cong \mathbb{Z}^k / \mathbb{Z} \cong \mathbb{Z}^{k-1},$$

explaining the \mathbb{Z}^{k-1} summand in the semimetal group. This \mathbb{Z}^{k-1} cannot be given a basis in terms of the k different Weyl point charges on the semimetal, and it must be interpreted more abstractly as the set of valid charge configurations. On $K^2 \times S^1$, the \mathbb{Z}_2 charge cancellation implies that

$$\text{im}(\beta) = \ker(\Sigma) \cong \mathbb{Z}^k / \mathbb{Z}_2 \cong \mathbb{Z}^k,$$

and this is the \mathbb{Z}^k which appears in the semimetal group in Equation (5.13). Just as on the torus, we should be careful not to interpret this \mathbb{Z}^k directly in terms of the charges of the k Weyl points. Even though it contains k factors of \mathbb{Z} , not all possible combinations of charges are contained in this subgroup: after all, charge configurations with an odd total are not in the kernel of Σ . Instead, it should be considered an index 2 subgroup of the charge configurations, containing only those with an even total.

Physically, the \mathbb{Z}^k summand in the semimetal group implies that a system with a single Weyl point ($k = 1$) on $K^2 \times S^1$ may already feature semimetal topology. The single Weyl point must have even charge by \mathbb{Z}_2 charge cancellation; an example of such a system is featured in the supplement to Ref. [12] and reproduced in Figure 5.14.

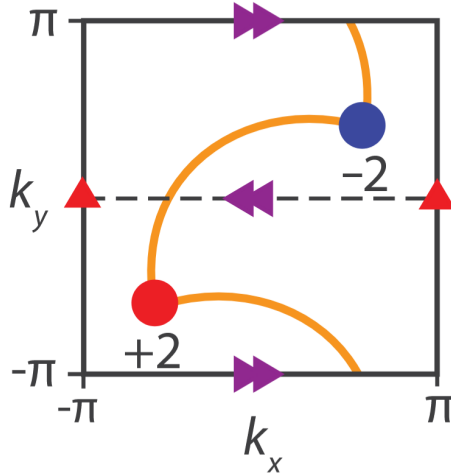


Figure 5.14: Figure from the supplement to Ref. [12]. Originally intended as a surface Brillouin zone with Fermi arcs, it can be interpreted equally well as a top view of a 3D system with two Dirac strings. Both Dirac strings are oriented towards the positively charged point.

Finally, we have seen in Section 4.2.2 that the Chern number on a 2D slice of \mathbb{T}^3 changes by $q \in \mathbb{Z}$ as the slice is passed over a Weyl point of charge q . We might expect this to be problematic in the non-orientable case, given that the Brillouin zone is periodic and the total charge need not add up to zero. This is resolved in two different ways for the two invariants ν_x and ν_z . The latter is saved by being a \mathbb{Z}_2 invariant, restoring the periodicity over an even total charge—as was also observed in Ref. [12].

The \mathbb{Z} invariant ν_x requires us to define the integration more carefully: as noted before, the integration in Equation (5.11) does not respect the symmetry, and it may

not yield the right invariant when Weyl points are introduced. This is illustrated in Figure 5.15(a). Instead, it becomes necessary to integrate over a symmetry-

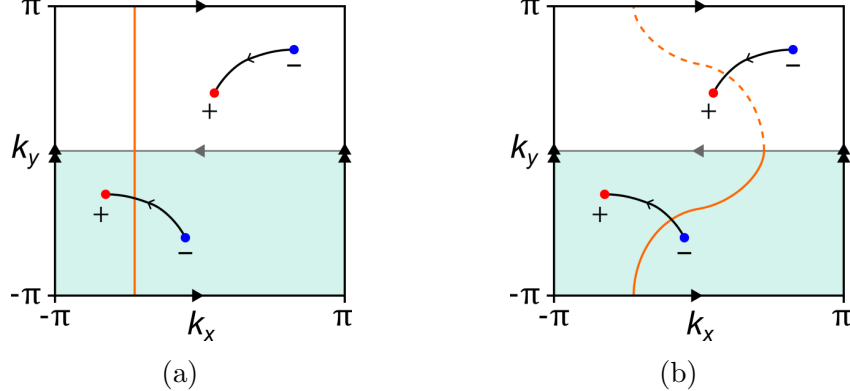


Figure 5.15: (a) In the presence of Weyl points, a given \mathbb{T}_{yz}^2 (orange) may only intersect a single Dirac string, leading to a non-integer value of $1/2$ from Equation (5.11). (b) Integration over an invariant surface always yields a well defined ν_x outside of Weyl points, since it intersects the twisted Dirac strings in a consistent manner. The dashed half of the surface is redundant, since both halves yield the same integral. The pictured setup yields $\nu_x = 1$.

invariant surface S which is continuously deformable to a \mathbb{T}_{yz}^2 , such as that shown in Figure 5.15(b). This is similar in spirit to the \mathcal{T} -invariant surfaces used to calculate invariants in the time-reversal symmetric case [36]. In principle, only the half of the surface $S_{1/2}$ which intersects the fundamental domain at $k_y \leq 0$ needs to be integrated over; this half surface can be considered a compact surface subspace of $K^2 \times S^1$. The calculation then takes the form

$$\nu_x = \frac{1}{2\pi} \int_{S_{1/2}} \mathcal{F}. \quad (5.14)$$

The question of periodicity is now resolved by the fact that the surface S cannot be moved across the entire Brillouin zone without breaking the symmetry: any such surface can be deformed equivariantly into exactly one of the glide planes at $k_x = 0$ and $k_x = \pm\pi$, but one cannot be deformed into the other. For example, if we start with S at the $k_x = 0$ plane and perturb a small section of S continuously in the positive x direction, then another section must be moved in the negative x direction at the same time to maintain glide symmetry. By continuity, it follows that S must still intersect $k_x = 0$ somewhere.¹² As such, there is no deformation that can completely remove S from the $k_x = 0$ plane, and in particular it cannot be taken fully to the glide plane at $k_x = \pm\pi$. An analogous argument holds the other way

¹²The argument can be formalised using the mean-value theorem if we take the momenta to live in \mathbb{R}^3 rather than identifying equivalent momenta into a torus.

around.¹³

As a final remark, we note that the only \mathbb{Z}_2 factor in the semimetal group in Equation (5.13) stems directly from the underlying insulating topology; any Weyl points that are added only introduce additional \mathbb{Z} factors. As such, it is the opinion of the author that no intrinsic \mathbb{Z}_2 charge should be assigned to Weyl points, as is done in Ref. [12].¹⁴ Instead, the \mathbb{Z}_2 invariant on gapped K^2 -like slices should be taken to be directly influenced by the \mathbb{Z} charge on Weyl points. To be precise, if such a slice with invariant ν_z is moved over a Weyl point of charge C in the k_z direction, the new \mathbb{Z}_2 invariant is

$$\nu'_z = \nu_z + C \mod 2,$$

requiring no \mathbb{Z}_2 charge on the Weyl point. This is also the position taken with respect to time-reversal invariant Weyl semimetals in Ref. [36].

5.2.4 Classification of K^2 surface states

We now turn our attention to the classification of surface states (i.e. Fermi arcs) on the two-dimensional surfaces of the $K^2 \times S^1$ system obeying the glide symmetry in Equation (5.4). As mentioned in Section 4.2.2, Fermi arcs may be considered projections of the topological Dirac strings existing in the bulk. The same line of reasoning holds in this case: the twisted Dirac strings may be projected onto a surface Brillouin zone to obtain oriented Fermi arcs.

Of the three coordinate directions that we may project along, the k_z direction is the most tractable, since there is no additional symmetry in this direction beyond the usual lattice translation. As such projecting along k_z amounts to integrating out the periodic S^1 direction in $K^2 \times S^1$, to obtain a Klein bottle shaped K^2 surface Brillouin zone spanning the k_x and k_y directions. This is the surface that is discussed extensively and probed experimentally in Ref. [12].

Because the projection π_z along the k_z direction loses no essential information about the symmetries of the system, it has a clear interpretation in terms of homology groups. Recall that, given a set of Weyl points $W \subset K^2 \times S^1$, a configuration of twisted Dirac strings c defines a twisted relative homology class:

$$[c] \in H_1(K^2 \times S^1, W; \widetilde{\mathbb{Z}}).$$

The projection π_z acts on c to give a configuration of Fermi arcs $\pi_z(c)$. Taking into account the twist in orientation, $\pi_z(c)$ can be taken to represent a homology class:

$$[\pi_z(c)] \in H_1(K^2, W'; \widetilde{\mathbb{Z}}),$$

¹³By the same logic, we can generally infer which of the two glide planes S deforms to by studying these intersections: for example, the surface in Figure 5.15(b) does not intersect the plane at $k_x = \pm\pi$, and so it must deform to $k_x = 0$. In general, we can count the number of times S intersects with $k_x = 0$ in the range $-\pi < k_y \leq 0$ (at any k_z); an odd number of intersections [such as the single crossing in the fundamental domain in Figure 5.15(b)] indicates that the surface deforms to $k_x = 0$.

¹⁴Explicit calculations are provided for this \mathbb{Z}_2 charge in Ref. [12], but these rely on integration over K^2 -like tubes spanning the fundamental domain in the k_y direction. As a result, these invariants are an expression of the global topology of $K^2 \times S^1 \setminus W$, not the local topology around a Weyl point.

where $W' := \pi_z(W)$ denotes the projection of the Weyl points on the surface. Formally, there is a surjective map

$$\pi_z^* : H_1(K^2 \times S^1, W; \widetilde{\mathbb{Z}}) \rightarrow H_1(K^2, W'; \widetilde{\mathbb{Z}}), \quad [c] \mapsto [\pi_z(c)]$$

called the *pushforward* of π_z on homology classes. The surjectivity of this map ensures that all possible configurations of Fermi arcs in $H_1(K^2, W'; \widetilde{\mathbb{Z}})$ are physically realisable, meaning this group provides a full classification of Fermi arcs on the K^2 surface.

The other groups in the twisted homology semimetal sequence in Equation (5.8) may also be mapped by similar pushforwards of π_z , and in particular this operation preserves the nature of the maps featured in the sequence. This then gives rise to a similar exact sequence of twisted homology groups on the K^2 surface:

$$0 \rightarrow \underbrace{H_1(K^2; \widetilde{\mathbb{Z}})}_{\text{Twisted Fermi loops}} \rightarrow \underbrace{H_1(K^2, W'; \widetilde{\mathbb{Z}})}_{\text{Twisted Fermi arcs}} \xrightarrow{\partial} H_0(W'; \widetilde{\mathbb{Z}}) \rightarrow H_0(K^2; \widetilde{\mathbb{Z}}) \rightarrow 0. \quad (5.15)$$

We can then make use of twisted Poincaré duality in order to turn this into a more computable Mayer–Vietoris sequence of ordinary cohomology groups:¹⁵

$$\dots \xrightarrow{0} H^1(K^2) \rightarrow H^1(K^2 \setminus W') \rightarrow \bigoplus_{w' \in W'} H^1(S^1_{w'}) \rightarrow H^2(K^2) \rightarrow 0. \quad (5.16)$$

Note that compared to the bulk sequence in Equation (5.7), this sequence classifies topological states in terms of first cohomology groups H^1 rather than second cohomology groups H^2 . This is indicative of the fact that the chiralities of surface states are given by winding numbers of the Berry connection 1-form \mathcal{A} , rather than Chern numbers obtained from the Berry curvature 2-form \mathcal{F} .

Just as in the bulk, the Mayer–Vietoris sequence in Equation (5.16) can be computed using standard tools such as cellular homology. The resulting explicit sequence is as follows:

$$\dots \xrightarrow{0} \mathbb{Z} \rightarrow \mathbb{Z} \oplus \mathbb{Z}^k \rightarrow \mathbb{Z}^k \xrightarrow{\Sigma} \mathbb{Z}_2 \rightarrow 0. \quad (5.17)$$

This sequence is very similar in nature and interpretation to the bulk sequence in Equation (5.9). The only essential difference is that the insulating \mathbb{Z}_2 invariant ν_z has disappeared as a result of the projection in the k_z direction.

In particular, this sequence features a similar mod 2 charge cancellation property to the one seen in the bulk, implying that the winding numbers of the Berry connection \mathcal{A} around each projected Weyl node must add to a total of $0 \in \mathbb{Z}_2$. Just as in the bulk, there is an important caveat regarding the physical interpretation of this: the sign of the winding number at a Weyl node w depends on a choice of orientation for the circle S^1_w that surrounds it. Just as in the bulk, this choice of orientation can be

¹⁵One needs to be a bit careful here in the sense that there is no longer a zero group to the left of the proper Mayer–Vietoris sequence, owing to the appearance of $H^0(S^1_{w'}) \cong \mathbb{Z}$ terms instead of the $H^1(S^2_w) = 0$ in the bulk sequence. However, this does not change the interpretation of the sequence at all: the leftmost map into $H^1(K^2)$ is still trivial, since the circles $S^1_{w'}$ are contractible inside K^2 .

induced from a chosen fundamental domain, and this may lead to different relative chiralities between projected Weyl points.

As an example, the experimentally observed dispersion in Figure 5.7 depends on the choice of fundamental domain. That is, one can extend the K^2 surface Brillouin zone to the full \mathbb{T}^2 in this figure by including momenta with $0 < k_2 \leq \pi$, and then choose a different fundamental domain to change the relative chirality. This is illustrated in Figure 5.16.

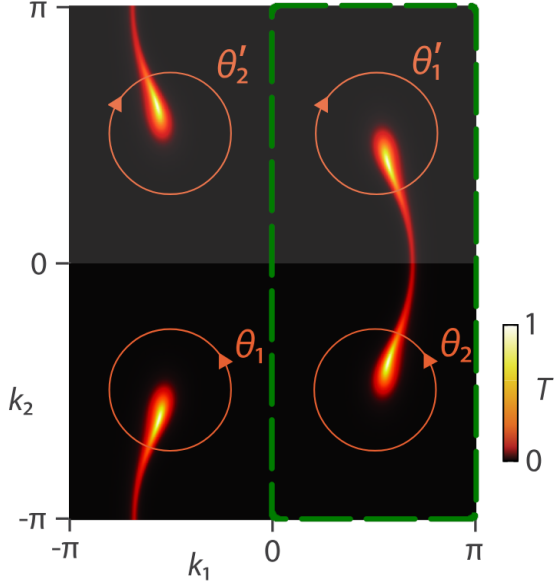


Figure 5.16: Figure adapted from Ref. [12], depicting the same system as Figure 5.7. The lower black region is the K^2 -like fundamental domain used by the authors. The upper grey region is obtained by mirroring this domain horizontally, completing the surface Brillouin torus. The two circular integration domains parametrised by θ_1 and θ_2 are mirrored to oppositely oriented circles parametrised by θ'_1 and θ'_2 respectively. Because the system respects this symmetry, the dispersion along θ'_1 and θ'_2 will look identical to that along θ_1 and θ_2 ; however, since the orientation is reversed, this implies that the underlying Weyl points have a negative rather than positive chirality. As a result, the fundamental domain chosen as in Figure 5.8(c) (here outlined in green) features two oppositely charged points.

The surface states obtained by truncating the system in the x and y directions cannot readily be expressed in terms of a similar surface Mayer–Vietoris sequence. For example, projecting in the k_x direction loses information about the $k_x \leftrightarrow -k_x$ action of the glide symmetry. One result of this is that the surface Brillouin zone is not non-orientable in this direction—it has the topology of the 2-torus \mathbb{T}^2 . This lack of non-orientability means that there is no non-trivial notion of twisted homology, which makes it impossible to encode the oppositely oriented Fermi arcs on this surface in terms of simple homology. As such, the precise classification of surface states in these two directions remains an open question.

5.3 Other non-orientable Brillouin zones

As we have reviewed in Sections 5.1 and 5.2.1, the fact that a single glide symmetry has a free action on the Brillouin torus does not guarantee that a combination of multiple glide symmetries also acts freely. This raises the question of whether there are any other momentum space symmetries besides the single glide reflection which give rise to a proper non-orientable Brillouin zone without high-symmetry points. Indeed, there are several in three dimensions; the aim of this section is to provide a complete overview of these symmetries.

We also provide a classification of the insulator and Weyl semimetal invariants existing on these three-dimensional non-orientable Brillouin zones, under the assumption that the action of the symmetry is unitary. That is, we provide the invariants obtained from ordinary cohomology and twisted homology, similar to the $K^2 \times S^1$ case discussed in the previous section. All explicitly calculated cohomology groups in this section are obtained using cellular homology.

In order to ensure completeness, this classification of Brillouin zones must rely on the theory of *space groups*, which fully categorise the possible symmetry operations on periodic systems [68]. We begin by briefly reviewing the two-dimensional case.

In two dimensions, the situation is quite manageable: there are only 17 space groups in total, which are referred to as the *wallpaper groups*. Of these, 13 are *symmorphic*, meaning their generators are symmetries with fixed points (i.e. mirror reflections and rotations in 2D). As a result, these groups cannot have a non-trivial free action. The four remaining non-symmorphic groups include at least one glide symmetry. Of these, it turns out that only the group pg featuring a single glide symmetry has a free action [69]. This is precisely the symmetry that gives rise to the Klein bottle shaped fundamental domain first discussed in Ref. [59]. We conclude that the Klein bottle K^2 is the only non-orientable two-dimensional manifold that can act as the Brillouin zone of a crystalline system.¹⁶ We have already studied its topology as a surface Brillouin zone in Equation (5.17).

In three dimensions, there are a total of 230 space groups. Among these, 73 are *symmorphic* (i.e. generated by point-fixing symmetries such as inversion, reflection and rotation) and the remaining 157 are non-symmorphic, featuring at least one glide reflection or screw rotation—the latter being a combination of a rotation and fractional lattice translation. Of the non-symmorphic space groups, a total of 12 have a group action that is free [69, Eq. (110)]. Of these, eight are generated only by screw rotations, which are orientation-preserving—just like ordinary rotations. This means they give rise to orientable fundamental domains, which can be classified using ordinary homology and cohomology. Nevertheless, these Brillouin zones may feature \mathbb{Z}_2 invariants owing to non-orientable subspaces, and we will discuss screw rotations combined with glide reflections. For these reasons, we briefly expand on one of these symmetries here before moving on to the four orientation-reversing cases.

The simplest space group featuring a screw rotation is $P2_1$, which is a \mathbb{Z}_2 group generated by a combined half turn and half lattice translation. For example, taking the screw axis to be the y axis, a Hamiltonian with a unitary $P2_1$ momentum space

¹⁶Again, this related to the fact that it is the only non-orientable manifold with a vanishing Euler characteristic.

symmetry obeys the relation

$$\mathcal{H}(k_x, k_y, k_z) = U\mathcal{H}(-k_x, k_y + \pi, -k_z)U^\dagger.$$

The fundamental domain of this symmetry can be taken to be the half torus with $-\pi \leq k_y \leq 0$ just as for the glide symmetry, but the boundary identifications are different: instead of mirroring the $k_y = -\pi$ face before identifying it with the $k_y = 0$ face, it must be rotated by a half turn. The resulting Brillouin zone topology is dubbed a “half-turn space” in Ref. [61], which probes a system with such a momentum space symmetry experimentally.¹⁷ The explicit semimetal Mayer–Vietoris sequence of this space is as follows:

$$0 \rightarrow \mathbb{Z} \oplus \mathbb{Z}_2^2 \rightarrow \mathbb{Z} \oplus \mathbb{Z}_2^2 \oplus \mathbb{Z}^{k-1} \rightarrow \mathbb{Z}^k \rightarrow \mathbb{Z} \rightarrow 0. \quad (5.18)$$

That is, the insulating invariants on the half-turn space are classified by $\mathbb{Z} \oplus \mathbb{Z}_2^2$, and Weyl points in the fundamental domain obey the regular Nielsen–Ninomiya theorem. The two \mathbb{Z}_2 invariants stem from K^2 -like subspaces of the half-turn space, one of which is illustrated in Figure 5.17.

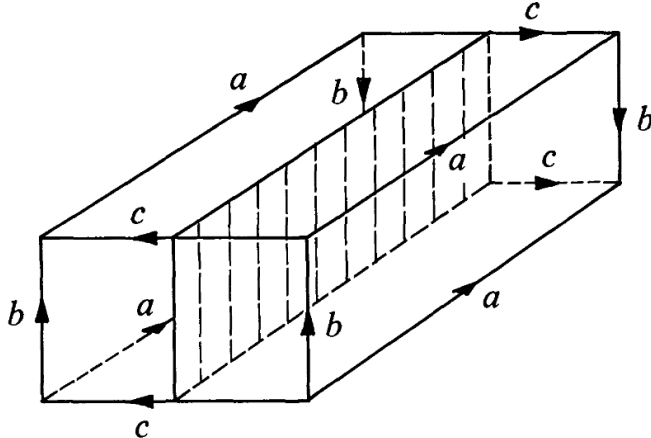


Figure 5.17: Figure from Ref. [70]. The half-turn space (called a “twisted cube” in that work) is shown with a two-dimensional subspace, which has the topology of a Klein bottle.

Free orientation-reversing space groups in 3D

We now turn our attention to the four remaining space groups with free actions, all of which give rise to a non-orientable Brillouin zone. The first and simplest of these is Pc , and it is precisely the \mathbb{Z}_2 group generated by a single glide symmetry that we have discussed at length in this chapter. Its semimetal Mayer–Vietoris sequence is given in Equation (5.9), and we refer to Section 5.2.3 for its interpretation.

The remaining three groups— Cc , $Pca2_1$ and $Pna2_1$ —all combine a glide symmetry with another operation to form a $\mathbb{Z}_2 \oplus \mathbb{Z}_2$ group. As such, the effective Brillouin

¹⁷To be precise, the full space group obeyed by the system in Ref. [61] is $P2_1/c$, which also features a glide symmetry; the action of this space group is not free.

zones that they induce cover exactly one fourth of the full Brillouin torus \mathbb{T}^3 . Just as in the $K^2 \times S^1$ case, their fundamental domains can be chosen in any number of ways, without changing the topology of the underlying manifolds. As such, we will remain agnostic about the choice of fundamental domain here, and simply provide the relevant Mayer–Vietoris sequences. The reader wishing to develop an intuition for the ways in which these spaces can be partitioned is referred to a space group atlas such as Ref. [71].

The group Cc combines a glide symmetry and a diagonal half-lattice translation, in such a way that the Hamiltonian obeys the following relations under unitary momentum space Cc symmetry (up to coordinate permutations):

$$\begin{aligned}\mathcal{H}(k_x, k_y, k_z) &= U\mathcal{H}(k_x, -k_y, k_z + \pi)U^\dagger, \\ \mathcal{H}(k_x, k_y, k_z) &= U\mathcal{H}(k_x + \pi, k_y + \pi, k_z)U^\dagger.\end{aligned}$$

The Mayer–Vietoris sequence associated with the non-orientable Brillouin zone under this unitary symmetry is as follows:

$$0 \rightarrow \mathbb{Z} \oplus \mathbb{Z}_2^2 \rightarrow \mathbb{Z} \oplus \mathbb{Z}_2^2 \oplus \mathbb{Z}^k \rightarrow \mathbb{Z}^k \rightarrow \mathbb{Z}_2 \rightarrow 0. \quad (5.19)$$

That is, this is the sequence in terms of ordinary cohomology or twisted homology.

The space group $Pca2_1$ features a glide reflection and a screw rotation. The unitary momentum space $Pca2_1$ symmetry acts on the Hamiltonian in the following way:

$$\begin{aligned}\mathcal{H}(k_x, k_y, k_z) &= U\mathcal{H}(k_x + \pi, -k_y, k_z)U^\dagger, \\ \mathcal{H}(k_x, k_y, k_z) &= U\mathcal{H}(-k_x, -k_y, k_z + \pi)U^\dagger.\end{aligned}$$

The associated Mayer–Vietoris sequence of ordinary cohomology groups is then

$$0 \rightarrow \mathbb{Z}_2^2 \rightarrow \mathbb{Z}_2^2 \oplus \mathbb{Z}^k \rightarrow \mathbb{Z}^k \rightarrow \mathbb{Z}_2 \rightarrow 0. \quad (5.20)$$

Finally, the group $Pna2_1$ is generated by similar operations as $Pca2_1$, but with the glide reflection plane offset from $k_y = 0$ by $\pi/2$; the resulting action on the Hamiltonian is

$$\begin{aligned}\mathcal{H}(k_x, k_y, k_z) &= U\mathcal{H}(k_x + \pi, \pi - k_y, k_z)U^\dagger, \\ \mathcal{H}(k_x, k_y, k_z) &= U\mathcal{H}(-k_x, -k_y, k_z + \pi)U^\dagger.\end{aligned}$$

The semimetal Mayer–Vietoris sequence in ordinary cohomology is

$$0 \rightarrow \mathbb{Z}_4 \rightarrow \mathbb{Z}_4 \oplus \mathbb{Z}^k \rightarrow \mathbb{Z}^k \rightarrow \mathbb{Z}_2 \rightarrow 0.$$

On the whole, all of these space groups share the same mod 2 charge cancellation seen on $K^2 \times S^1$, as is to be expected from the non-orientability of the underlying Brillouin zone. Incidentally, all three Mayer–Vietoris sequences feature different insulating invariants, which immediately confirms that the underlying manifold is different for each of these space groups (and also different from $K^2 \times S^1$). The insulating topology for a unitary $Pna2_1$ symmetry is especially interesting, being classified by a single \mathbb{Z}_4 invariant. Such invariants are fairly uncommon; for example, they do not appear in the tenfold way classification in Table [ref]. The derivation of an explicit expression and physical interpretation for this invariant is beyond the scope of this work, but the system certainly deserves further study.

5.4 Inversion symmetry ansatz

[Write out inversion symmetry logic + calculation results]

Chapter 6

Conclusions and outlook

In this chapter, we take stock of the current state of the research performed in this work. We begin in Section 6.1 by briefly summarising the key results presented in Chapter 5. We then expand on some avenues of possible further research in Section 6.2, speculating on specific lines of inquiry where appropriate.

6.1 Summary of main results

The central results of this thesis are focused around gaining a deeper understanding of how non-orientability in momentum space alters the topological description of Weyl semimetals—a state of matter that is fundamentally chiral in nature. This was achieved in large part by applying the appropriate tools from algebraic topology to a glide symmetric system featuring a Brillouin zone with $K^2 \times S^1$ topology, of which several salient properties had already been established in Ref. [12].

Contextualisation of the Poincaré–Hopf theorem

An important aspect of obtaining a cogent topological description lies in deciding which tools from topology are suitable to use in the first place. To this end, we have placed the role that the Poincaré–Hopf theorem plays in deriving the Nielsen–Ninomiya charge cancellation on firmer theoretical footing. In three dimensions, Poincaré–Hopf states that the singularities of a tangent vector field on a compact manifold should have topological indices which sum to zero. Nielsen–Ninomiya is then usually derived by noting that the $\mathbf{h}(\mathbf{k})$ appearing in the model Hamiltonian can be considered such a tangent vector field. We note that this is categorically not the case on non-orientable manifolds; in this context, $\mathbf{h}(\mathbf{k})$ is a section of the trivial \mathbb{R}^3 -bundle over the manifold, rather than the tangent bundle. The mismatch in orientability between the base manifold and the \mathbb{R}^3 -bundle is precisely what causes the Poincaré–Hopf/Nielsen–Ninomiya theorems to become modified to a mod 2 charge cancellation.

Formalism for obtaining twisted coefficients

In order to obtain a full classification in terms of homology and cohomology on a non-orientable system, one needs to decide how to restore Poincaré duality. This is

done by twisting the coefficients of either the homology or the cohomology; only one of these choices yields the correct topological invariants. The correct twisting is usually motivated using arguments relating to vector bundle classification. These arguments are relatively tractable for a free unitary action such as the one featured in the $K^2 \times S^1$ system, but they quickly become conceptually involved when studying more complex symmetries (i.e. those that have fixed points, are anti-unitary, etc.), requiring much mathematical legwork to be done in order to obtain the final topological invariants.

To remedy this situation, we demonstrate that a highly straightforward heuristic arises in the specific context of Weyl semimetals: one can study how a given orientation-reversing symmetry acts on Weyl points. If the symmetric partner of a Weyl point has the same chirality, this indicates a twist in the cohomology, and if it has the opposite chirality, the twist is in the homology. This twist then carries over to the underlying insulating topology, so that this heuristic is also useful for classifying those insulating phases which are mediated by transitional Weyl semimetals. This formalism is not rigorous enough to fully replace vector bundle classification, since in general one still needs to study how any fixed points of the symmetry are treated in the equivariant homology and cohomology. However, these features might also be assessable using similar heuristics, depending on the system. In any case, the formalism is useful for developing physical intuition, and it serves as a good sanity check in classification schemes making use of these twisted groups.

Classification of $K^2 \times S^1$ bulk and K^2 surface invariants

We provide a full classification and interpretation of the topological invariants on the $K^2 \times S^1$ system arising from a single momentum space glide symmetry, based on the explicitly calculated Mayer–Vietoris sequence in Equation (5.9). This includes both the insulating invariants, which are classified by $\mathbb{Z} \oplus \mathbb{Z}_2$, and the semimetal invariants, classified by $\mathbb{Z} \oplus \mathbb{Z}_2 \oplus \mathbb{Z}^k$ with k the number of Weyl points on $K^2 \times S^1$. Aside from the \mathbb{Z}_2 invariant ν_z which has been well studied previously, we also find a seemingly novel \mathbb{Z} invariant ν_x . We demonstrate how ν_x and ν_z can be obtained from the action of the glide symmetry on two of the basic homology invariants in $H_1(\mathbb{T}^3) \cong \mathbb{Z}^3$, and how the third invariant is trivialised by the same action. Based on these observations, we provide two integral equations for explicit calculation of ν_x : Equation (5.11) in terms of a simple Chern number in the insulating context, and Equation (5.14) in terms of curved planes in the semimetallic context. This illustrates the usefulness of the twisted homology point of view.

We also provide a classification of the surface states arising from truncation in the periodic S^1 direction, in the form of the Mayer–Vietoris sequence in Equation (5.17). This sequence has very similar features to the bulk $K^2 \times S^1$ sequence, save for the fact that the \mathbb{Z}_2 invariant ν_z is projected out.

Clarification of mod 2 charge cancellation

The Mayer–Vietoris sequence in Equation (5.9) also provides a more solid conceptual basis for the mod 2 charge cancellation on $K^2 \times S^1$ described in Ref. [12]. It relates to the fact that the charges of all Weyl points must sum to zero in the group $H^2(K^2 \times S^1) \cong \mathbb{Z}_2$, which appears where a \mathbb{Z} group would usually be in the orientable

case. This is closely related to the lack of a canonical orientation at each Weyl point. In particular, it follows that the total chirality is ill defined as an integer, being sensitive to arbitrary local choices of orientation (or equivalently, choice of a fundamental domain). We assert that this amounts to an unphysical degree of freedom, so that any apparent net non-zero chirality cannot have phenomenological consequences.

Classification of non-orientable Brillouin zones

Through use of the theory of space groups, we ascertain that there are exactly three other symmetry groups in three dimensions besides the single glide symmetry which have a free action giving rise to a non-orientable fundamental Brillouin zone: Cc , $Pca2_1$ and $Pna2_1$. Just as for $K^2 \times S^1$, we provide explicitly calculated Mayer–Vietoris sequences for each of these three systems. Each of them features the same \mathbb{Z}_2 charge cancellation as $K^2 \times S^1$; the differences lie in the insulating invariants. Explicitly, the insulating phases under Cc symmetry are classified by $\mathbb{Z} \oplus \mathbb{Z}_2^2$, those under $Pca2_1$ are given by \mathbb{Z}_2^2 and those under $Pna2_1$ are given by \mathbb{Z}_4 . This latter group is especially interesting, featuring a topological invariant of order four.

Ansatz for inversion symmetry invariants

6.2 Research recommendations

Outlook points:

- $K^2 \times S^1$ surface states in k_x and k_y directions
- The same MV sequence in Equation (5.17) may also apply to 2D type AIII Klein bottle WSM with chiral symmetry; there is a difference in Fermi arcs vs. Dirac strings etc. but the topology should be similar.
- 2D non-Hermitian systems: König, Yang et al. → Stålhammar & Rødland → present work
- Heuristic approach to dealing with fixed points in equivariant homology may be feasible
- Applicability of this description is probably limited under addition of non-trivial additional bands, e.g. 4-band models incorporating spin and orbital degrees of freedom. The full scope of applicability is somewhat of an open question at this point. (E.g., how well are 2D chiral WSMs described by this homology picture?)
- Experimental verification in acoustic crystals may be relatively straightforward.
- Anti-unitary glide symmetry \implies twisted cohomology on $K^2 \times S^1$?

Notes

Concepts explored in early personal notes:

- Calculations of (co)homology and semimetal MV sequence for manifolds in ≥ 2 dimensions:
 - All compact surfaces without boundary, i.e. the surfaces M_g and N_g
 - All spaces of the form $M = K^2 \times \mathbb{T}^{d-2}$
- Σ and the other maps in the MV sequence are difficult to interpret in the $\chi \neq 0$ case (maybe even generally for odd dimensions). Taking the oriented case as an example, the MV sequence ends as

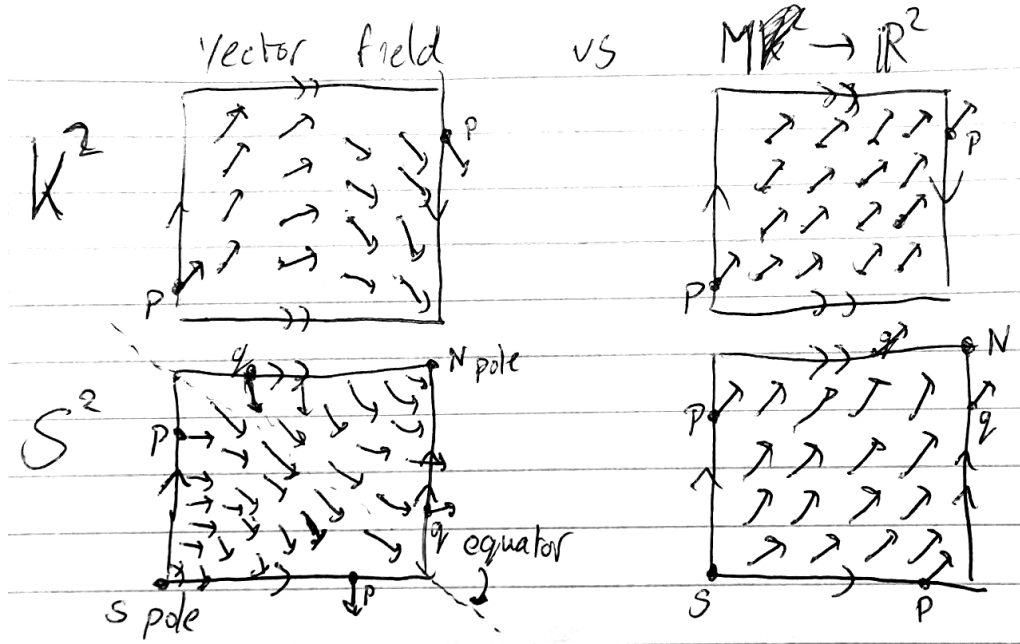
$$H^{d-1}(M \setminus \Delta) \rightarrow H^{d-1}\left(\bigsqcup_k S^{d-1}\right) \cong \mathbb{Z}^k \xrightarrow{\Sigma} H^d(M) \cong \mathbb{Z}$$

so that the “charge configuration” in \mathbb{Z}^k must map to 0 by Σ in order to descend from the semimetal, regardless of whether $\chi = 0$.

- This may imply that the Bloch vector field carries more topological information about the total charge than the MV sequence (which makes sense since it generates *all* homology groups of the valence bundle, and all Betti numbers factor into χ). As a concrete example, consider $M = S^2$ with a single puncture of charge +2. The punctured sphere is topologically a disc, so that the valence bundle must be trivial, while the Bloch vector field is topologically non-trivial in the sense that it has an index +2 singularity. In addition, all relevant $H_n(A) \oplus H_n(B)$ are zero, so that the semimetal MV reduces to the statement that $H_2(S^2) \cong H_1(S^1)$.
- It may even be the case that the valence bundle cannot be generated from the Bloch vector field in the $d = 2$ case; it’s probably worth studying the $d \in \{3, 4, 5\}$ cases (pullback of some universal bundle) to learn more about this. The $d = 3$ case should be especially helpful in understanding how the valence bundle arises from the vector field.
- The map $H : \mathbb{R}^3 \rightarrow \mathfrak{su}(2)$, $\vec{h} \mapsto \vec{h} \cdot \vec{\sigma}$ is an isomorphism of Lie algebras, with the cross product as a Lie bracket on \mathbb{R}^3 . Still the vector field is discontinuous on a non-orientable manifold, while H is not. This suggests an alternative approach for constructing the valence bundle: consider h as a map $M \rightarrow \mathbb{R}^d$ instead of an element of $\mathfrak{X}(M)$, and then pull back the universal bundle along the unit map $\hat{h} : M \setminus \Delta \rightarrow S^{d-1}$. That is, we detach \vec{h} from the tangent bundle and consider it a more abstract map. An added “benefit” of this is that we lose all coordinate dependence. However, this may also be a downside in the sense that the map will not be subject to the same constraints (Poincaré–Hopf etc.) that the vector field is; for example, $S^2 \rightarrow \mathbb{R}^2$, $x \mapsto (1, 0)$ is a perfectly valid map that would violate the hairy ball theorem as a vector field (and this is a result of being unable to cover S^2 by a single chart). At this point the question

may become more about which description is more physical in nature, and the non-orientable Weyl point paper[12] seems to imply there may be more to the $h : M \rightarrow \mathbb{R}^3$ story. It also seems to agree better with the intuition of an applied external potential removing all Weyl nodes – something that's impossible for $\chi \neq 0$ if charge corresponds to vector field index. It also explains how the valence bundle can be trivial on the once punctured S^2 .

- Any smooth d -manifold can be given a CW complex structure with one d -cell (link). On this d -cell there is an exact correspondence between vector fields and maps to \mathbb{R}^d , since it can be embedded in \mathbb{R}^d . What distinguishes the two is how points on the boundary of the d -cell are identified with each other; this determines whether the “vectors” need to change orientation. To illustrate:



- On any orientable manifold, the Stokes' theorem argument shows that the total charge must be zero regardless of Euler characteristic:

$$\sum_{\alpha} w(S_{\alpha}) = \sum_{\alpha} \int_{S_{\alpha}} c_1(E) = \sum_{\alpha} \int_{S_{\alpha}} \frac{\text{Tr } \mathcal{F}}{2\pi} = \int_{B'} d \frac{\text{Tr } \mathcal{F}}{2\pi} = 0$$

where the last equality holds by the Bianchi identity for the trace. This means the valence bundle cannot be a pullback along a tangent vector field for $\chi \neq 0$.

On a non-orientable manifold, this argument doesn't hold since the integral over B' isn't well defined.

Appendix A

Cellular (co)homology

[Write out short example of a cellular homology calculation if I have time]

Bibliography

- [1] Allen Hatcher. *Algebraic Topology*. Cambridge: Cambridge Univ. Press, 2002. URL: <https://pi.math.cornell.edu/~hatcher/AT/ATpage.html> (visited on 10/07/2024).
- [2] Glen E. Bredon. *Topology and geometry*. 139. Springer International Publishing, 1993. ISBN: 978-1-4419-3103-0. DOI: [10.1007/978-1-4757-6848-0](https://doi.org/10.1007/978-1-4757-6848-0).
- [3] Raoul Bott and Loring W. Tu. *Differential Forms in Algebraic Topology*. 82. New York, NY: Springer Science+Business Media New York, 1982. ISBN: 978-1-4419-2815-3. DOI: [10.1007/978-1-4757-3951-0](https://doi.org/10.1007/978-1-4757-3951-0).
- [4] Daniel S Freed and Gregory W Moore. “Twisted Equivariant Matter”. In: *Annales Henri Poincaré* 14.8 (Dec. 2013), pp. 1927–2023.
- [5] Guo Chuan Thiang. “On the K-Theoretic Classification of Topological Phases of Matter”. In: *Annales Henri Poincaré* 17.4 (Apr. 2016), pp. 757–794.
- [6] Anton Akhmerov et al. *Online course on topology in condensed matter*. URL: <https://topocondmat.org/> (visited on 10/07/2024).
- [7] János K. Asbóth, László Oroszlány, and András Pályi. *A Short Course on Topological Insulators*. Springer International Publishing, 2016. ISBN: 9783319256078. DOI: [10.1007/978-3-319-25607-8](https://doi.org/10.1007/978-3-319-25607-8). URL: <http://dx.doi.org/10.1007/978-3-319-25607-8>.
- [8] B. Andrei Bernevig and Taylor L. Hughes. *Topological insulators and topological superconductors*. Princeton University Press, 2013. ISBN: 978-0-691-15175-5.
- [9] Masatoshi Sato and Yoichi Ando. “Topological superconductors: a review”. In: *Reports on Progress in Physics* 80.7 (May 2017), p. 076501. ISSN: 1361-6633. DOI: [10.1088/1361-6633/aa6ac7](https://doi.org/10.1088/1361-6633/aa6ac7). URL: <http://dx.doi.org/10.1088/1361-6633/aa6ac7>.
- [10] P. Gehring et al. “A Natural Topological Insulator”. In: *Nano Letters* 13.3 (Mar. 2013), pp. 1179–1184. ISSN: 1530-6992. DOI: [10.1021/nl304583m](https://doi.org/10.1021/nl304583m). URL: <http://dx.doi.org/10.1021/nl304583m>.
- [11] Felix Bloch. “Über die Quantenmechanik der Elektronen in kristallgittern”. In: *Zeitschrift für Physik* 52.7–8 (July 1929), pp. 555–600. DOI: [10.1007/bf01339455](https://doi.org/10.1007/bf01339455).
- [12] André Grossi Fonseca et al. “Weyl Points on Nonorientable Manifolds”. In: *Phys. Rev. Lett.* 132 (26 June 2024), p. 266601. DOI: [10.1103/PhysRevLett.132.266601](https://doi.org/10.1103/PhysRevLett.132.266601). URL: <https://link.aps.org/doi/10.1103/PhysRevLett.132.266601>.

- [13] W. P. Su, J. R. Schrieffer, and A. J. Heeger. “Solitons in Polyacetylene”. In: *Phys. Rev. Lett.* 42 (25 June 1979), pp. 1698–1701. DOI: 10.1103/PhysRevLett.42.1698. URL: <https://link.aps.org/doi/10.1103/PhysRevLett.42.1698>.
- [14] W. P. Su, J. R. Schrieffer, and A. J. Heeger. “Soliton excitations in polyacetylene”. In: *Phys. Rev. B* 22 (4 Aug. 1980), pp. 2099–2111. DOI: 10.1103/PhysRevB.22.2099. URL: <https://link.aps.org/doi/10.1103/PhysRevB.22.2099>.
- [15] Michael Freedman et al. “A class of P,T-invariant topological phases of interacting electrons”. In: *Annals of Physics* 310.2 (2004), pp. 428–492. ISSN: 0003-4916. DOI: <https://doi.org/10.1016/j.aop.2004.01.006>. URL: <https://www.sciencedirect.com/science/article/pii/S0003491604000260>.
- [16] Eric J Meier, Fangzhao Alex An, and Bryce Gadway. “Observation of the topological soliton state in the Su–Schrieffer–Heeger model”. en. In: *Nat. Commun.* 7.1 (Dec. 2016), p. 13986.
- [17] Marcos Atala et al. “Direct measurement of the Zak phase in topological Bloch bands”. In: *Nature Physics* 9.12 (Nov. 2013), pp. 795–800. ISSN: 1745-2481. DOI: 10.1038/nphys2790. URL: <http://dx.doi.org/10.1038/nphys2790>.
- [18] H Weyl. “Gravitation and the Electron”. en. In: *Proc Natl Acad Sci U S A* 15.4 (Apr. 1929), pp. 323–334.
- [19] N. P. Armitage, E. J. Mele, and Ashvin Vishwanath. “Weyl and Dirac semimetals in three-dimensional solids”. In: *Rev. Mod. Phys.* 90 (1 Jan. 2018), p. 015001. DOI: 10.1103/RevModPhys.90.015001. URL: <https://link.aps.org/doi/10.1103/RevModPhys.90.015001>.
- [20] Pavan Hosur and Xiaoliang Qi. “Recent developments in transport phenomena in Weyl semimetals”. In: *Comptes Rendus Physique* 14.9 (2013). Topological insulators / Isolants topologiques, pp. 857–870. ISSN: 1631-0705. DOI: <https://doi.org/10.1016/j.crhy.2013.10.010>. URL: <https://www.sciencedirect.com/science/article/pii/S1631070513001710>.
- [21] Conyers Herring. “Accidental Degeneracy in the Energy Bands of Crystals”. In: *Phys. Rev.* 52 (4 Aug. 1937), pp. 365–373. DOI: 10.1103/PhysRev.52.365. URL: <https://link.aps.org/doi/10.1103/PhysRev.52.365>.
- [22] A.A. Burkov. “Weyl Metals”. In: *Annual Review of Condensed Matter Physics* 9.1 (Mar. 2018), pp. 359–378. ISSN: 1947-5462. DOI: 10.1146/annurev-conmatphys-033117-054129. URL: <http://dx.doi.org/10.1146/annurev-conmatphys-033117-054129>.
- [23] Alexey A Soluyanov et al. “Type-II Weyl semimetals”. In: *Nature* 527.7579 (Nov. 2015), pp. 495–498.
- [24] H.B. Nielsen and M. Ninomiya. “Absence of neutrinos on a lattice: (I). Proof by homotopy theory”. In: *Nuclear Physics B* 185.1 (1981), pp. 20–40. ISSN: 0550-3213. DOI: [https://doi.org/10.1016/0550-3213\(81\)90361-8](https://doi.org/10.1016/0550-3213(81)90361-8). URL: <https://www.sciencedirect.com/science/article/pii/0550321381903618>.

- [25] H.B. Nielsen and M. Ninomiya. “Absence of neutrinos on a lattice: (II). Intuitive topological proof”. In: *Nuclear Physics B* 193.1 (1981), pp. 173–194. ISSN: 0550-3213. DOI: [https://doi.org/10.1016/0550-3213\(81\)90524-1](https://doi.org/10.1016/0550-3213(81)90524-1). URL: <https://www.sciencedirect.com/science/article/pii/0550321381905241>.
- [26] Hongming Weng et al. “Weyl Semimetal Phase in Noncentrosymmetric Transition-Metal Monophosphides”. In: *Phys. Rev. X* 5 (1 Mar. 2015), p. 011029. DOI: <10.1103/PhysRevX.5.011029>. URL: <https://link.aps.org/doi/10.1103/PhysRevX.5.011029>.
- [27] Shin-Ming Huang et al. “A Weyl Fermion semimetal with surface Fermi arcs in the transition metal monopnictide TaAs class”. In: *Nature Communications* 6.1 (June 2015), p. 7373.
- [28] B Q Lv et al. “Observation of Weyl nodes in TaAs”. In: *Nature Physics* 11.9 (Sept. 2015), pp. 724–727.
- [29] Su-Yang Xu et al. “Discovery of a Weyl fermion state with Fermi arcs in niobium arsenide”. In: *Nature Physics* 11.9 (Sept. 2015), pp. 748–754.
- [30] Ilya Belopolski et al. “Signatures of a time-reversal symmetric Weyl semimetal with only four Weyl points”. In: *Nature Communications* 8.1 (Oct. 2017), p. 942.
- [31] Gui-Geng Liu et al. “Topological Chern vectors in three-dimensional photonic crystals”. In: *Nature* 609 (2022), pp. 925–930. DOI: <10.1038/s41586-022-05077-2>.
- [32] Varghese Mathai and Guo Chuan Thiang. “Differential Topology of Semimetals”. In: *Communications in Mathematical Physics* 355.2 (July 2017), pp. 561–602. ISSN: 1432-0916. DOI: <10.1007/s00220-017-2965-z>. URL: <http://dx.doi.org/10.1007/s00220-017-2965-z>.
- [33] Varghese Mathai and Guo Chuan Thiang. “Global topology of Weyl semimetals and Fermi arcs”. In: *Journal of Physics A: Mathematical and Theoretical* 50.11 (Feb. 2017), 11LT01. ISSN: 1751-8121. DOI: <10.1088/1751-8121/aa59b2>. URL: <http://dx.doi.org/10.1088/1751-8121/aa59b2>.
- [34] David Vanderbilt. *Berry Phases in Electronic Structure Theory: Electric Polarization, Orbital Magnetization and Topological Insulators*. Cambridge University Press, 2018, pp. 215–218. DOI: <https://doi.org/10.1017/9781316662205>.
- [35] Chiara Devescovi et al. “Cubic 3D Chern photonic insulators with orientable large Chern vectors”. In: *Nature Communications* 12.1 (Dec. 2021), p. 7330.
- [36] Guo Chuan Thiang, Koji Sato, and Kiyonori Gomi. “Fu–Kane–Mele monopoles in semimetals”. In: *Nuclear Physics B* 923 (Oct. 2017), pp. 107–125. ISSN: 0550-3213. DOI: <10.1016/j.nuclphysb.2017.07.018>. URL: <http://dx.doi.org/10.1016/j.nuclphysb.2017.07.018>.
- [37] Giuseppe De Nittis and Kiyonori Gomi. “Classification of “Quaternionic“ Bloch-Bundles”. In: *Communications in Mathematical Physics* 339.1 (Oct. 2015), pp. 1–55.

- [38] Giuseppe De Nittis and Kiyonori Gomi. “The cohomological nature of the Fu–Kane–Mele invariant”. In: *Journal of Geometry and Physics* 124 (2018), pp. 124–164. ISSN: 0393-0440. DOI: <https://doi.org/10.1016/j.geomphys.2017.10.007>. URL: <https://www.sciencedirect.com/science/article/pii/S0393044017302607>.
- [39] Zhijun Wang et al. “Hourglass fermions”. In: *Nature* 532.7598 (Apr. 2016), pp. 189–194.
- [40] Yige Chen, Heung-Sik Kim, and Hae-Young Kee. “Topological crystalline semimetals in nonsymmorphic lattices”. In: *Phys. Rev. B* 93 (15 Apr. 2016), p. 155140. DOI: [10.1103/PhysRevB.93.155140](https://doi.org/10.1103/PhysRevB.93.155140). URL: <https://link.aps.org/doi/10.1103/PhysRevB.93.155140>.
- [41] Heejae Kim and Shuichi Murakami. “Emergent spinless Weyl semimetals between the topological crystalline insulator and normal insulator phases with glide symmetry”. In: *Phys. Rev. B* 93 (19 May 2016), p. 195138. DOI: [10.1103/PhysRevB.93.195138](https://doi.org/10.1103/PhysRevB.93.195138). URL: <https://link.aps.org/doi/10.1103/PhysRevB.93.195138>.
- [42] Ken Shiozaki, Masatoshi Sato, and Kiyonori Gomi. “Topology of nonsymmorphic crystalline insulators and superconductors”. In: *Phys. Rev. B* 93 (19 May 2016), p. 195413. DOI: [10.1103/PhysRevB.93.195413](https://doi.org/10.1103/PhysRevB.93.195413). URL: <https://link.aps.org/doi/10.1103/PhysRevB.93.195413>.
- [43] Tomáš Bzdušek et al. “Nodal-chain metals”. In: *Nature* 538.7623 (Oct. 2016), pp. 75–78.
- [44] Benjamin J. Wieder and C. L. Kane. “Spin-orbit semimetals in the layer groups”. In: *Phys. Rev. B* 94 (15 Oct. 2016), p. 155108. DOI: [10.1103/PhysRevB.94.155108](https://doi.org/10.1103/PhysRevB.94.155108). URL: <https://link.aps.org/doi/10.1103/PhysRevB.94.155108>.
- [45] Y. X. Zhao and Andreas P. Schnyder. “Nonsymmorphic symmetry-required band crossings in topological semimetals”. In: *Phys. Rev. B* 94 (19 Nov. 2016), p. 195109. DOI: [10.1103/PhysRevB.94.195109](https://doi.org/10.1103/PhysRevB.94.195109). URL: <https://link.aps.org/doi/10.1103/PhysRevB.94.195109>.
- [46] Bohm-Jung Yang et al. “Topological semimetals protected by off-centered symmetries in nonsymmorphic crystals”. In: *Phys. Rev. B* 95 (7 Feb. 2017), p. 075135. DOI: [10.1103/PhysRevB.95.075135](https://doi.org/10.1103/PhysRevB.95.075135). URL: <https://link.aps.org/doi/10.1103/PhysRevB.95.075135>.
- [47] Luyang Wang, Shao-Kai Jian, and Hong Yao. “Hourglass semimetals with nonsymmorphic symmetries in three dimensions”. In: *Phys. Rev. B* 96 (7 Aug. 2017), p. 075110. DOI: [10.1103/PhysRevB.96.075110](https://doi.org/10.1103/PhysRevB.96.075110). URL: <https://link.aps.org/doi/10.1103/PhysRevB.96.075110>.
- [48] Shan-Shan Wang et al. “Hourglass Dirac chain metal in rhenium dioxide”. In: *Nature Communications* 8.1 (Nov. 2017), p. 1844.
- [49] Benjamin J. Wieder et al. “Wallpaper fermions and the nonsymmorphic Dirac insulator”. In: *Science* 361.6399 (July 2018), pp. 246–251. ISSN: 1095-9203. DOI: [10.1126/science.aan2802](https://doi.org/10.1126/science.aan2802). URL: <http://dx.doi.org/10.1126/science.aan2802>.

- [50] Xiaoliang Xiao et al. “Ideal hourglass-type charge-three Weyl fermions in spinless systems”. In: *Phys. Rev. B* 109 (7 Feb. 2024), p. 075160. DOI: 10.1103/PhysRevB.109.075160. URL: <https://link.aps.org/doi/10.1103/PhysRevB.109.075160>.
- [51] Rui-Xing Zhang and Chao-Xing Liu. *Nonsymmorphic Symmetry Protected Dirac, Möbius, and Hourglass Fermions in Topological Materials*. 2022. arXiv: 2207.00020 [cond-mat.mes-hall]. URL: <https://arxiv.org/abs/2207.00020>.
- [52] Chen Zhang et al. “General Theory of Momentum-Space Nonsymmorphic Symmetry”. In: *Phys. Rev. Lett.* 130 (25 June 2023), p. 256601. DOI: 10.1103/PhysRevLett.130.256601. URL: <https://link.aps.org/doi/10.1103/PhysRevLett.130.256601>.
- [53] Z Y Chen et al. “Classification of time-reversal-invariant crystals with gauge structures”. In: *Nature Communications* 14.1 (Feb. 2023), p. 743. DOI: 10.1038/s41467-023-36447-7.
- [54] Y. X. Zhao, Yue-Xin Huang, and Shengyuan A. Yang. “ \mathbb{Z}_2 -projective translational symmetry protected topological phases”. In: *Phys. Rev. B* 102 (16 Oct. 2020), p. 161117. DOI: 10.1103/PhysRevB.102.161117. URL: <https://link.aps.org/doi/10.1103/PhysRevB.102.161117>.
- [55] Y. X. Zhao et al. “Switching Spinless and Spinful Topological Phases with Projective PT Symmetry”. In: *Phys. Rev. Lett.* 126 (19 May 2021), p. 196402. DOI: 10.1103/PhysRevLett.126.196402. URL: <https://link.aps.org/doi/10.1103/PhysRevLett.126.196402>.
- [56] L. B. Shao et al. “Gauge-Field Extended $k \cdot p$ Method and Novel Topological Phases”. In: *Phys. Rev. Lett.* 127 (7 Aug. 2021), p. 076401. DOI: 10.1103/PhysRevLett.127.076401. URL: <https://link.aps.org/doi/10.1103/PhysRevLett.127.076401>.
- [57] Haoran Xue et al. “Projectively Enriched Symmetry and Topology in Acoustic Crystals”. In: *Phys. Rev. Lett.* 128 (11 Mar. 2022), p. 116802. DOI: 10.1103/PhysRevLett.128.116802. URL: <https://link.aps.org/doi/10.1103/PhysRevLett.128.116802>.
- [58] Tianzi Li et al. “Acoustic Möbius Insulators from Projective Symmetry”. In: *Phys. Rev. Lett.* 128 (11 Mar. 2022), p. 116803. DOI: 10.1103/PhysRevLett.128.116803. URL: <https://link.aps.org/doi/10.1103/PhysRevLett.128.116803>.
- [59] Z. Y. Chen, Shengyuan A. Yang, and Y. X. Zhao. “Brillouin Klein bottle from artificial gauge fields”. In: *Nature Communications* 13.2215 (Apr. 2022). DOI: 10.1038/s41467-022-29953-7.
- [60] Yu-Liang Tao et al. “Higher-order Klein bottle topological insulator in three-dimensional acoustic crystals”. In: *Phys. Rev. B* 109 (13 Apr. 2024), p. 134107. DOI: 10.1103/PhysRevB.109.134107. URL: <https://link.aps.org/doi/10.1103/PhysRevB.109.134107>.

- [61] Zhenxiao Zhu et al. “Brillouin Klein space and half-turn space in three-dimensional acoustic crystals”. In: *Science Bulletin* 69.13 (2024), pp. 2050–2058. ISSN: 2095-9273. DOI: <https://doi.org/10.1016/j.scib.2024.05.003>. URL: <https://www.sciencedirect.com/science/article/pii/S2095927324003372>.
- [62] Jinbing Hu, Songlin Zhuang, and Yi Yang. “Higher-Order Topological Insulators via Momentum-Space Nonsymmorphic Symmetries”. In: *Phys. Rev. Lett.* 132 (21 May 2024), p. 213801. DOI: 10.1103/PhysRevLett.132.213801. URL: <https://link.aps.org/doi/10.1103/PhysRevLett.132.213801>.
- [63] Yanqiu Wang et al. *Chess-board Acoustic Crystals with Momentum-space Non-symmorphic Symmetries*. 2023. arXiv: 2305.07174 [cond-mat.mes-hall]. URL: <https://arxiv.org/abs/2305.07174>.
- [64] Yu-Liang Tao, Jiong-Hao Wang, and Yong Xu. *Quadrupole Insulator without Corner States in the Energy Spectrum*. 2023. arXiv: 2307.00486 [cond-mat.mes-hall]. URL: <https://arxiv.org/abs/2307.00486>.
- [65] George William Whitehead. *Elements of Homotopy Theory*. Graduate Texts in Mathematics. Springer, 2012. ISBN: 978-1-4612-6320-3. DOI: 10.1007/9781-4612-6318-0.
- [66] Loring W. Tu. *Introductory Lectures on Equivariant Cohomology: (AMS-204)*. Princeton University Press, Mar. 2020. ISBN: 9780691191751. DOI: 10.23943/princeton/9780691191751.001.0001. URL: <https://doi.org/10.23943/princeton/9780691191751.001.0001>.
- [67] Graeme Segal. “Equivariant K-theory”. In: *Publications Mathématiques de l'IHÉS* 34 (Jan. 1968), pp. 129–151. DOI: 10.1007/BF02684593.
- [68] Theo Hahn, ed. *International Tables for Crystallography, Volume A: Space-Group Symmetry*. Dordrecht; London: Springer, 2002.
- [69] L. Michel. “Fundamental concepts for the study of crystal symmetry”. In: *Physics Reports* 341.1 (2001). Symmetry, invariants, topology, pp. 265–336. ISSN: 0370-1573. DOI: [https://doi.org/10.1016/S0370-1573\(00\)00091-0](https://doi.org/10.1016/S0370-1573(00)00091-0). URL: <https://www.sciencedirect.com/science/article/pii/S0370157300000910>.
- [70] John W. Woll Jr. “One-Sided Surfaces and Orientability”. In: *The Two-Year College Mathematics Journal* 2.1 (1971), pp. 5–18. DOI: 10.1080/00494925.1971.11973990. URL: <https://www.tandfonline.com/doi/abs/10.1080/00494925.1971.11973990>.
- [71] Jeremy Karl Cockcroft. *A Hypertext Book of Crystallographic Space Group Diagrams and Tables*. 1999. URL: <http://img.chem.ucl.ac.uk/sgp/mainmenu.htm> (visited on 06/16/2025).